The Hong Kong Polytechnic University

Department of Health Technology and Informatics

DEVELOPMENT OF A NONCONTACT ULTRASOUND INDENTATION SYSTEM FOR MEASURING TISSUE MATERIAL PROPERTIES USING WATER JET

By

Min-Hua Lu

B. Eng.

A thesis submitted in partial fulfilment of the requirements for the Degree of Doctor of Philosophy in Biomedical Engineering

Nov 2006

CERTIFICATE OF ORIGINALITY

I hereby declare that this thesis is my own work and that, to the best of my knowledge and belief, it reproduces no material previously published or written, nor material that has been accepted for the award of any other degree or diploma, except where due acknowledge has been made in the text.

_____

(Min-Hua Lu)

ABSTRACT of thesis titled "Development of a Noncontact Ultrasound Indentation System for Measuring Tissue Material Properties Using Water Jet"

Submitted by **Min-Hua Lu**

for the degree of Doctor of Philosophy in Biomedical Engineering at the Hong Kong Polytechnic University in Sep 2006

To measure or image the mechanical properties of tissues has been attracting increasing research efforts during the recent decades. The purpose of this research was to develop a noncontact ultrasound indentation system using water jet compression. The key idea was to use a water jet as the indenter and simultaneously as the medium for ultrasound to propagate through so as to measure or map the mechanical properties of tissues. A high frequency focused ultrasound (20 MHz) transducer was used in the system for measuring tissue thickness and deformation at a high resolution. A pressure sensor installed within the water pipe could monitor the water pressure during the indentation process. The device was fixed on a high-resolution 3-D translating device, thus the system could easily conduct 1-D or 2-D scan across the tissue sample and obtain the modulus distribution of soft tissue.

Tissue-mimicking phantoms were used for the validation of the ultrasound water jet indentation system. It was found that the stiffness ratio defined as the pressure applied on

phantom surface to the local strain of the phantom correlated very well with the Young's modulus of the phantom measured using the uniaxial compression test. Therefore, the stiffness ratio was employed as an indicator of the tissue stiffness. The repeatability of the measurement was very good with Intra-class coefficient (ICC) > 0.99. The phantom study was also used to demonstrate the ability of the new system to map the distribution of the stiffness. Results showed that both the spatial resolution (0.4 mm) and the contrast resolution (6.7 kPa) were good enough for the modulus imaging of most soft tissues.

The ultrasound water jet indentation system provided a noncontact way for the measurement of both mechanical and acoustical properties of soft tissues. It was used to assess the degeneration of articular cartilage in this study. It was found that, after the bovine patellar cartilages were treated by 0.25% trypsin solution for 4 hours, their stiffness ratios were significantly reduced by 44.3% ± 17.0%, and the peak-to-peak amplitude of ultrasound echoes reflected from the cartilage surface significantly decreased by 35.64% ± 19.51% in comparison with the intact samples. The system was also employed to monitor the healing of the bone-tendon junction tissues of rabbits after partial patellectomy. Low intensity pulsed ultrasound (LIPUS) and functional electrical stimulation (FES) were used to accelerate the healing of the bone-tendon junction structures. After studying the stiffness and Young's modulus of the remained patellar cartilage, the junction tissue and the tendon, it was found that the patellar cartilages and junctions of the postoperative samples were significantly softer than those of the control

samples, and the junction tissues of the samples treated by LIPUS and FES were significantly stiffer than those of the postoperative samples without any treatment.

With further improvement of the system and the development of an appropriate model to simulate the interaction between the water jet and soft tissues, the ultrasound water jet indentation system could be potentially used to assess the mechanical and acoustical properties of living tissues, tissues with small dimensions, bioengineered tissues, and other materials.

ACKNOWLEDGEMENTS

Given this opportunity, I would like to acknowledge all the help from the people around me. During the four years of study, it was just with their honest help, I could start, keep on and finally finish the work as described in the sections to follow.

First I would like to thank my supervisor, Dr. Yong-Ping Zheng, for helping me so much during the four years. When I began my postgraduate study, I was just a junior engineer and knew little about research. Dr. Zheng not only taught me a lot of things, such as how to search the literature, to present the research work, and to write academic articles, but also has greatly affected me with his very active, devoted and energetic attitude to research. Through lots of times of discussions with him, Dr. Zheng has given me tremendous ideas, suggestions and feedbacks on my research project. This thesis has greatly benefited from his invaluable research experiences. Therefore, my deepest appreciation is especially given to him. I must also thank my co-supervisor, Professor Arthur FT Mak, for his valuable suggestions and encouragements to my study. He was also the main lecturer of one of my selected subjects “Mechanics of Living Tissues & Systems”. Thanks for his wonderful lectures and sincerely speaking, I learned a lot from this class.

My grateful thanks also go to Ms. Sally Ding. She is not only a good teacher for me and gave her valuable reviews on my research reports, but also a very nice friend to me. She gave me the warmest care and encouragements to both my study and life, shared those

happy hours with me, and most importantly, taught me to be a sincere, frank and zealous person. Without anything provided by her, I could not fulfil my four-year Ph.D study in Hong Kong smoothly. Therefore, my special appreciation is given to her.

I would like to thank all the colleagues in REC, especially those in our group. In particular, sincere thanks to Qing-Hua Huang for his great support in development of software, Qing Wang for her important help in sharing her knowledge about cartilage, Carrie Ling for her great help in design of my experiments, Alex Choi, Yan-Ping Huang, and Xin Chen for their constructive discussions on my experiments, and Jun-Feng He, James Cheung, Cong-Zhi Wang, Hai-Jun Niu, Jun Shi, Grace Lo and Sushil Patil for their kind helps to my study.

I wish to thank Dr. Ming Zhang, Dr. Randolph CK Leung, Prof. VC Mow, and Prof. Ling Qin for their important comments and suggestions on my research proposal and study. I also thank Dr. Jason Cheung for his great help in my learning of finite element simulation, Mr. CF Tin, Mr. Samy Leung and Mr. KC Chen for their kind helps in the development of the system presented in this thesis.

I would also like to thank all the staffs in the Department of Health Technology and Informatics (HTI) of The Hong Kong Polytechnic University for providing me the help in my work and giving me warm, friendly and collaborating circumstances.

Finally, I would like to extend my deepest thanks to my parents and my sister for their self-giving loves and supports. I must also give my sincere appreciation to my husband Qing-Hua Huang and my daughter Amy, for their support and love, and, for everything.

PUBLICATIONS

Patent

Zheng YP and Lu MH, Noncontact measurement of material properties. US Patent. Application No.10/954, 022. Filed in Sept 2004. Issued in Sept 2006 (Patent No. to be issued).

Peer-reviewed Journal Papers

1. Lu MH, Zheng YP and Huang QH. A novel method to obtain modulus image of soft tissues using water jet indentation. *IEEE transactions on Biomedical Engineering*. Accepted (Apr 2006).

2. Lu MH, Zheng YP, and Huang QH. A Novel non-contact ultrasound indentation system for measurement of tissue material properties using water jet compression. *Ultrasound in Medicine and Biology*. 31: 817-826, 2005.

3. Lu MH, Zheng YP, and Huang QH. Ultrasound elastomicroscopy using water beam indentation: preliminary study. In: *State of the Art: Ultrasonics in Medicine*. Elsevier, 87-96, 2004.

4. Lu MH, Zheng YP. Indentation test of soft tissues with curved substrates: a finite element study. *Medical and Biological Engineering and Computing*. 42: 535-540, 2004.

5. Zheng YP, Lu MH, and Wang Q. Noncontact ultrasound elastomocroscopy: potentials for assessment for articular cartilage. *Ultrasonics*. In press (Dec 2005).

6. Zheng YP, Li ZM, Choi APC, Lu MH, Chen X, and Huang QH. Ultrasound palpation sensor for tissue thickness and elasticity measurement - assessment of transverse carpal ligament. *Ultrasonics*. In press (Dec 2005).

7. Yu W, Li YB, Zheng YP, Lim NY, Lu MH and Fan JT. Softness measurement for open-cell foam materials and human soft tissue. *Measurement Science and Technology*. 17: 1785-1791, 2006.

8. Huang QH, Zheng YP, Lee R and Lu MH. 3D measurement of body tissues based on ultrasound images with 3D spatial information. *Ultrasound in Medicine and Biology*. 31(12):1607-15, 2005.

9. Huang QH, Zheng YP, Lu MH, and Chi ZR. Development of a portable 3D ultrasound imaging system for musculoskeletal tissues. *Ultrasonics*. 43: 153-163, 2005.

10. Zheng YP, Bridal SL, Shi J, Saied A, Lu MH, Jaffre B, Mak AFT, Laugier P. High resolution ultrasound elastomicroscopy imaging of soft tissues: System development and feasibility. *Physics in Medicine and Biology* 2004; 49: 3925-3938.

11. Lu MH**,** Zheng YP, Yu W, Huang QH, LO G, Huang YP. A hand-held indentation system for the assessment of the mechanical properties of soft tissues *in vivo*. *Instrumentation Science and Technology*. Submitted (Aug 2006).

12. Huang QH, Zheng YP, Lu MH and Chi ZR. Speckle suppression and contrast enhancement in reconstruction of freehand 3-D ultrasound images using an adaptive distance-weighted method. *IEEE Transactions on Biomedical Engineering.* Submitted (Sep 2006).

13. Lu MH, Zheng YP, Huang QH, Ling HY, Mak AFT and Wang Q. Assessment of articular cartilage degeneration using a novel ultrasound water jet indentation system. (To be submitted to *Physics in Medicine and Biology*).

14. Lu MH, Zheng YP, Lu HB, Huang QH and Qin L. A noncontact ultrasound indentation system for assessing bone-tendon junction tissues: a preliminary result. (To be submitted to *Medical Engineering and Physics*).

15. Lu MH, Zheng YP, Qin L, Lu HB, and Huang QH. Noncontact ultrasound evaluation of bone-tendon junction tissues treated by low intensity pulsed ultrasound. (To be submitted to *IEEE Transactions on Neural Systems and Rehabilitation Engineering*).

Selected Conference Paper and Presentations

1. Lu MH, Zheng YP, Lu HB, Huang QH, and Qin L. A novel ultrasound water-jet indentation system for assessing bone-tendon joint tissues. *5th World Congress of Biomechanics*, Munich, Germany, July 29 – Aug 4, 2006.

2. Zheng YP, Li ZM, Choi APC, Lu MH, and Huang QH. Ultrasound palpation sensor for the measurement of tissue thickness and elasticity of transverse carpal ligament. *5th World Congress of Biomechanics*, Munich, Germany, July 29 – Aug 4, 2006.

3. Li ZM, Zheng YP, Lu MH, Choi APC, and Huang QH. Ultrasound palpation of carpal tunnel mechanics. *52nd Annual Meeting of the Orthopaedic Research Society*, Chicago, Illinois, US, Mar 19-22, 2006.

4. Lu MH, Zheng YP, Lu HB, Huang QH, and Qin L. Noncontact ultrasound indentation system for assessing bone-tendon junction tissues: preliminary results. *The 4th international conference on the ultrasonic measurement and imaging of tissue elasticity*. Oct. 16-19, 2005, Lake Travis, Austin, Texas, USA.

5. Lu MH, Zheng YP, and Huang QH. A novel method to obtain modulus image of soft tissues using water jet compression. *The 27th annual international conference IEEE engineering in medicine and biology society*, Sep. 1-4, 2005, Shanghai, China

6. Lu MH**,** Zheng YP and Huang QH. Noncontact ultrasound indentation system for

measuring tissue material properties using water beam. *Third International Conference on the Ultrasonic Measurement and Imaging of Tissue Elasticity*, Oct 17~20, 2004, Lake Windermere, Cumbria, United Kingdom.

7. Huang QH, Lu MH, and Zheng YP. Optical and ultrasound elastomicroscopy for imaging tissues elasticity in high resolution. *Biomedical Engineering Conference, BME 2004*, pp.130-134, Hong Kong.

8. Lu MH, Zheng YP, and Huang QH. Ultrasound elastomicroscopy using water beam indentation: preliminary study. Proceedings of *7th Congress of the Asian Federation of Societies for Ultrasound in Medicine and Biology* (*AFSUMB*), Utsunomiya, Japan. International Congress Series 1274: 87-96, 2004.

9. Lu MH and Zheng YP. Noncontact ultrasound indentation using water beam. *Second International Conference on the Ultrasonic Measurement and Imaging of Tissue Elasticity*, Oct 12~15, 2003, Corpus Christi, USA.

10. Zheng YP, Lu MH and Huang QH. An optical method for ultrasound elastomicroscopy. *Second International Conference on the Ultrasonic Measurement and Imaging of Tissue Elasticity*, Oct 12~15, 2003, Corpus Christi, USA.

11. Lu MH and Zheng YP. Indentation test of soft tissues embedded with hard tissues with different curvatures: a finite element study. *World Congress on Medical Physics and Biomedical Engineering*, August 24-29, 2003, Sydney, Australia.

12. Zheng YP, Bridal L, Shi J, Saied A, Lu MH, Jaffre B, Mak AFT, Laugier P, and Qin L. Ultrasound elastomicroscopy for articular cartilage: from static to transient and 1D to 2D. *SPIE Medical Imaging: Ultrasonic Imaging and Signal Processing Conference*, February 15-20 2003, San Diego, CA USA. 398-410.

13. Zheng YP, Bridal L, Lu MH, Jaffre B, Saied A, Mak AFT, and Laugier P. Ultrasound elastomicroscopy (UEM): system development. *World Congress for Chinese Biomedical Engineers*, December 11-13, 2002, Taipei, Taiwan. I07.

14. Zheng YP, Saied A, Jaffre B, Lu MH, Bridal L, Laugier P, and Mak AFT. Development of an ultrasound elastomicroscopy (UEM) system: preliminary results. *First International Conference on the Ultrasonic Measurement and Imaging of Tissue Elasticity*, Oct 20~23, 2002, Niagara Falls, Canada. P5.

TABLE OF CONTENTS

LIST OF FIGURES

LIST OF TABLES

ABBREVIATIONS

1-D:	one dimensional
2-D:	two dimensional
F/D:	force/deformation
COMP:	cartilage oligomeric matrix protein
LVDT:	linear variable differential transducer
SNR:	signal-to-noise ratio
CW:	continuous wave
TUPS:	tissue ultrasound palpation system
UBM:	ultrasound biomicroscopy
PG:	Proteoglycan
MRI:	magnetic resonance imaging
OCT:	optical coherent tomography
ICC:	intra-class coefficient
RF:	radio frequency
sCV:	standardized coefficient of variation
BTJ:	bone-tendon junction
LIPUS:	low intensity pulsed ultrasound
FES:	functional electronic stimulation
QLV:	quasi-linear viscoelastic
FBG:	fibre Bragg grating

CHAPTER I INTRODUCTION

1.1 Background

To measure or image the mechanical properties of tissues has been attracting increasing research efforts during the recent decades. The stiffness of soft tissues may change under different pathological situations, and even normal tissues may have different stiffness, which is important information for tissue characterization. The mechanical properties of tissues can have different values depending on whether they are measured *in vivo* or *in-vitro* and *in situ* or as an excised specimen (Fung 1981, Mow and Hayes 1997). For the lack of quantitative tools for *in vivo* assessment of living tissue, manual palpation has been the primary technique for tissue stiffness assessment for many years in clinics. However, it strongly relies on personal experiences and cannot provide a quantitative measurement of changes in tissue stiffness.

Indentation is one of the most frequently used approaches to assess the soft tissues *in situ* or *in vivo*. Cylindrical flat-ended or spherical indenters have been used to perform contact loading on soft tissues. By obtaining tissue thickness using a needle probe or optical based methods, researchers have reported mathematical solutions to extract the elastic modulus of thin layer soft tissues from indentation data (Waters 1965; Hayes et al. 1972; Mak et al. 1987; Mow et al. 1989; Chicot et al. 1996; Yu and Blanchard 1996; Sakamoto et al. 1996; Haider and Holmes 1997). Several generations of indentation instruments have been developed for the assessment of tissue mechanical properties, especially for

articular cartilage (Kempson et al. 1971; Hori and Mockros 1976; Mow et al. 1989; Newton et al. 1997; Arokoski et al. 1994, 1999; Athanasiou et al. 1995, 1999; Shepherd and Seedhom 1997). These mechanical indentation apparatuses employed a load cell to measure the loading force, and a displacement transducer (LVDT) to record the tissue deformation according to the displacement of the indenter. However, the structures of these mechanical indentation instruments are complicated and not convenient for *in vivo* measurement. For clinical application, similar but portable indentation instruments have been developed for the quantification of cartilage stiffness under arthroscopic control (Lyyra et al. 1995), *in vivo* analysis of residual limb tissues (Pathak et al. 1998), plantar tissue stiffness measurement in patients with diabetes mellitus and peripheral neuropathy (Klaesner et al. 2002), stiffness estimation of spinal tissues (Kawchuk and Fauvel 2001) and heel pad stiffness assessment (Rome and Webb 2000). These indentation apparatuses used the obtained force/deformation (F/D) curves to indicate the tissue stiffness. However, the obtained stiffness may depend on the tissue thickness, which cannot be measured using these instruments.

Ultrasound indentation was proposed in the last decade which integrated a load cell and a flat-ended unfocused ultrasound transducer to monitor the indentation response of soft tissues (Zheng and Mak 1996, Hsu et al. 1998, Adam et al. 1998, Suh et al. 2001, Kawchuk et al. 2000, Laasanen et al. 2002). The ultrasound transducer served as an indenter to compress the tissue and meanwhile collected the echoes reflected from the tissues during indentation to obtain the deformation and tissue thickness simultaneously

and noninvasively. However, ultrasound indentation typically operated in the frequency range between 2 MHz and 10 MHz and was normally used to measure the mechanical properties of entire tissue layers. Its resolution is not sufficient to map the mechanical properties of soft tissue with fine structures, such as articular cartilage, corneal tissues or skins. Using high-frequency for ultrasound indentation may improve the resolution, but the high-frequency focused ultrasound transducer cannot be used for traditional contact indentation due to its concave-face. In addition, it is not common to use contact indentation to image the distribution of elastic modulus for a region of tissue due to the restrictions of the low spatial resolution (typically greater than 2 mm) and the long measurement time. With the use of nanoindentation (Oliver and Pharr 1992), high resolution modulus imaging could be achieved for a small region of a thin layer of material which is likely to be homogeneous in the entire thickness. However, the technique has not been widely used for the assessment of soft tissue as the testing results were highly dependent on the surface condition of the specimen (Guo et al. 2001).

Ultrasound elastography, on the other hand, could provide a local strain image inside soft tissues along the transducer axis by comparing the ultrasound cross-section images before and after compression (Ophir et al. 1991, 1999, Cespedes and Ophir 1993). The local strain image with good resolution and contrast is useful for medical diagnosis. However, tissue strain is not a fundamental tissue property as it depends on the tissue mechanical properties and other factors, such as the tissue geometry, tissue connectivity, modulus contrast and distribution, applied strain and boundary conditions. Shear modulus images

of soft tissues were obtained when the tissue was vibrated either by a low-frequency shear wave produced by an external vibrator (Krouskop et al. 1987, Lerner et al. 1990, Yamakoshi et al. 1990, Sandrin et al. 2002) or by the acoustic radiation force produced by focused ultrasound (Fatemi and Greenleaf 1998, Nightingale et al. 2002, Chen et al. 2002). The spatial resolution of the elasticity images using the current medical ultrasound frequency is usually on the order of several millimeters and may not be sufficient for the assessment of tissues with fine structures.

1.2 Objectives of This Study

The objectives of this study are:

1. To develop a noncontact ultrasound indentation system using water jet compression. The use of a water jet as the indenter and simultaneously as the medium for ultrasound to propagate through would be beneficial to measure or map the mechanical properties of tissues at a microscopic level in a nondestructive way.

2. To evaluate the ability of the ultrasound water jet indentation system for the determination and imaging of the mechanical properties using tissue-mimicking phantoms.

3. To apply the ultrasound water jet indentation to assess the degeneration of bovine articular cartilage and to monitor the healing of rabbit bone-tendon junction tissues.

1.3 Outline of the Dissertation

The remaining chapters of this thesis are outlined as follows:

In Chapter 2, a literature review is presented. The mechanical properties of articular cartilage, the theoretical models and instrumentations of mechanical indentation, arthroscopic indentation, ultrasound indentation and nanoindentation are introduced. The approaches of imaging the distribution of tissue mechanical properties using ultrasound, elastography and elastomicroscopy are also reviewed in this chapter.

Chapter 3 describes the methodologies of this study. The development of the ultrasound water jet indentation system is first introduced. The composition and calibration of the system, validation methods for the system, and the efforts in modeling the interaction between the water jet and soft tissues are described. The methods for obtaining modulus image of phantoms with varied modulus distribution using the water jet ultrasound indentation system are then presented. Following with the experiments on phantoms, two applications of the water jet ultrasound indentation system used to assess the degeneration of articular cartilage and to monitor the healing of bone-tendon junction tissues, are demonstrated.

Chapter 4 reports the results obtained using the methods introduced in Chapter 3. The results of the calibration and validation of the system are presented, followed by the results of modulus imaging approach applyed to the tissue-mimicking phantom. The

experimental results for the *in situ* assessments of bovine articular cartilage and rabbit bone-tendon junction tissues are finally reported.

In Chapter 5, systematic discussions on the ultrasound water jet indentation system and the obtained experimental results are provided. The advantage and the limitations of the system are discussed in detail, and the findings of the *in situ* experimental results are also presented.

Chapter 6 summarizes the development and applications of the ultrasound water jet indentation system presented in this PhD study. Suggestions on future investigations are also highlighted to address possible improvements of this system in the future for the measurement and imaging of the mechanical properties of various living tissues and biomaterials.

This work provides an original contribution to the research in biomechanics. A novel and unique experimental technique had been developed which offers several advantages for the measurement and imaging both the mechanical and acoustical properties of soft tissues, especially for thin layer of tissues with fine structures simultaneously and conveniently. The system also offers the advantage of no direct contact between the device and the sample thus minimizes the risk of tissue damage during water jet examination compared with those contact indentation measurements.

CHAPTER II LITERATURE REVIEW

Articular cartilage has unique material properties that enable the cartilage to perform its physiological functions over a lifetime and under a wide range of loading conditions. Numerious studies have investigated the mechanical properties of soft tissues, especially for the articular cartilage. In this chapter, a review was conducted on the theoretical and experimental studies on the measurement or imaging the behavior of articular caritlage and other human tissues under load. The composition and structure of articular cartilage were first presented, followed by the theoretical models and measurement instrumentations developed for the determination of the mechanical properties of cartilage. Finally the imaging techniques for mapping the material properties of soft tissues were introduced.

2.1 Mechanical Properties of Articular Cartilage

2.1.1 Composition, Structure and Function of Articular Cartilage

Articular cartilage is glistening, smooth, intact, and substantial tissue in its young, healthy and normal state. In older individuals and in preclinical disease states, the tissue loses this appearance and looks dull and roughened. Articular cartilage fibrillates, forms deep fissures, and in advanced osteoarthritis, is entirely lost at weight bearing sites over the joint surface (Mow and Hayes, 1997). To provide a basis for understanding this disease process, it is necessary to understand the relationships among the composition, structure and the function existing for articular cartilage.

Articular cartilage can be regarded as multiphasic materials with two major phases: a fluid phase composed of water and electrolytes and a solid phase composed of collagen, proteoglycans, and other proteins, glycoproteins, and the chondrocytes (Mow et al. 1980). Most of the articular cartilage is water (68%-85%), 10% to 20% of its wet weight is type II collagen, and 5%-10% of its wet weight is proteoglycan. Table 2-1 shows a summary of the components of articular cartilage. Each phase of the tissue contributes significantly to its known mechanical properties. Of the organic components, the collagens provide the quantitatively major organic components, followed by aggrecans and proteoglycan aggregates. Quantitatively minor components include link protein, hyaluronan, biglycan, decorin, and perlican, fibromodulin and thrombospondin, and COMP (cartilage oligomeric matrix protein). Although some of the noncollagenous components of articular cartilage are not described yet, an understanding of the structure-function relation for articular cartilage will be developed based on the current knowledge.

Water is the most abundant component of articular cartilage. It is believed that in normal cartilage, a portion of this water (approximately 30%) resides within the intrafibrillar space of collagen, and for normal tissue this proportion appears not to vary with age (Maroudas et al. 1991). The diameter of collagen fibers, and the amount of water within the intrafibrillar compartment, are modulated by the swelling pressure generated by the fixed charge density of the surrounding proteoglycans. In the native tissue, it appears that

most of this intrafibrillar water is not available for transport under mechanical loading and is excluded from the proteoglycans. In contrast, there is a significant increase of

Table 2-1. A summary of the components of articular cartilage (Mow and Hayes, 1997).

Component	Wet weight
Quantitatively major	
Water	60-85%
Collagen, type II	15-22%
Aggrecan	4-7%
Quantitatively minor (<5%)	
Link protein	
Hyaluronan	
Biglycan	
Collagen type I	
Collagen type V	
Collagen type VI	
Collagen type IX	
Collagen type XI	
COMP	
Decorin	
Fibromodulin	
Perlican	
Thrombospondin	

water content in degenerating articular cartilages. It is not known yet, however, whether the same proportion of water exists in the intrafibrillar space within these degenerating cartilages. The changes in total water content have strong influences in the mechanical, swelling, and fluid-transparent properties exhibited by the tissue. The amount of water present depends largely on several factors: the concentration of the proteoglycans, the

organization of the collagen network, and the strength and stiffness of this network. In cartilage from osteoarthritic joints, disruption of the collagen network can cause the water content of the tissue to increase by more than 10% (McDevitt and Muir, 1976), and this increase greatly affects the mechanical properties of the tissue (Mow et al. 1984). Most of the fluid and ions within the tissue are freely exchangeable by diffusion with the bathing solution surrounding the tissue. The interstitial fluid may also be extruded from the tissue by applying a pressure gradient across the tissue or by simply compressing the tissue. As the interstitial fluid flows through the pores of the collagen-proteoglycan solid matrix, significant frictional drag forces are exerted on the walls of the pores of the solid matrix, thus causing compaction. Such nonlinear flow-induced compression effect, sometimes called strain-dependent permeability, is very important in the physiology of articular cartilage because it means that it becomes more difficult to squeeze fluid from such tissues after a relatively long compression (Mow and Hayes, 1997).

In articular cartilage, the primary function of the collagen appears to be to provide the tensile properties to the tissues. Collagen has a high degree of structural organization (Figure 2-1). The basic triple helical structure unit of collagen is formed from three polypeptide chains, each of which has a natural left-handed helix, that together form a right-hand helix (Mow and Hayes, 1997). This highly organized structure appears to have been specially designed to resist tension. Proteoglycans are large complex biomolecules and are composed of a protein core to which one or more GAG chains are covalently attached. The major proteoglycan in articular cartilage is aggrecan. It plays an important

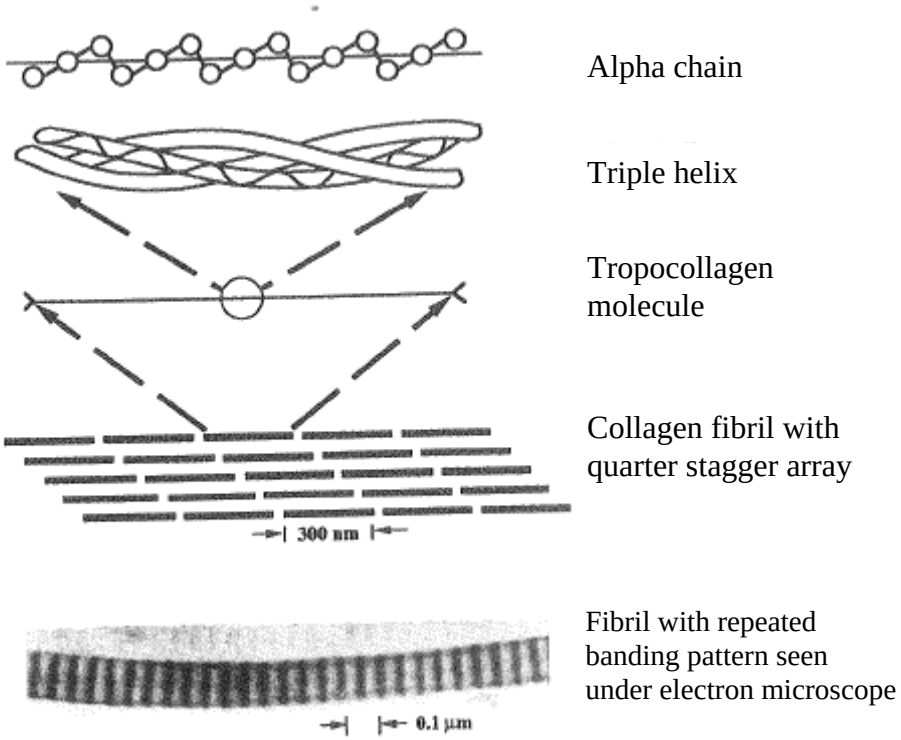

Figure 2-1. Schematic representation and photomicrograph of the collagen fibril structure (Mow and Hayes, 1997).

role in skeletal growth, joint function, and the development of osteoarthritis. Important molecular interactions exist not only between the proteoglycans and between the collagens, but also between the proteoglycans and aggregates. These interactions, along with force acting within the tissue and those applied on the tissue, can affect chondrocyte metabolism, collagen fibrillogenesis, and collagen network organization. The interaction between the collagen network and the proteoglycan aggregates is mainly frictional in nature; it is also required in the biology of tissue maintenance.

From the material standpoint, the content and structure of collagen and proteoglycan within articular cartilage vary with depth from the articulating surface. The collagen content is highest in the surface zone (approximately 85% by dry weight), and it decreases to 68% in the middle zone. Electron microscopy studies have shown that articular cartilage can be regarded as having three separate structural zones (Figure 2-2): superficial tangential zone, middle zone and deep zone. In the superficial tangential zone (10% to 20% of the total tissue thickness), fine collagen fibrils are organized parallel to the articular surface. In the middle zone (40% to 60% of the total thickness), the collagen fibrils have a larger diameter and appear to be oriented either randomly or in vertical columns. In the deep zone (about 30% of the total thickness), the fibers appear to be woven together to form large fiber bundles organized perpendicular to the surface. These bundles cross the tidemark to insert into the calcified cartilage and subchondral bone, thus securely anchoring the uncalcified tissue onto the bone ends. The concentration of proteoglycan in articular cartilage is lowest in the surface zone and highest in the middle zone, which produces variations in the tensile stiffness and swelling behaviors of samples obtained from the various zones of the tissue and causes swelling when the tissue is removed from the bone. The layered morphology of the collagen network and the preferred orientation of collagen fibers of articular cartilage demonstrate the inhomogeneity and anisotropy.

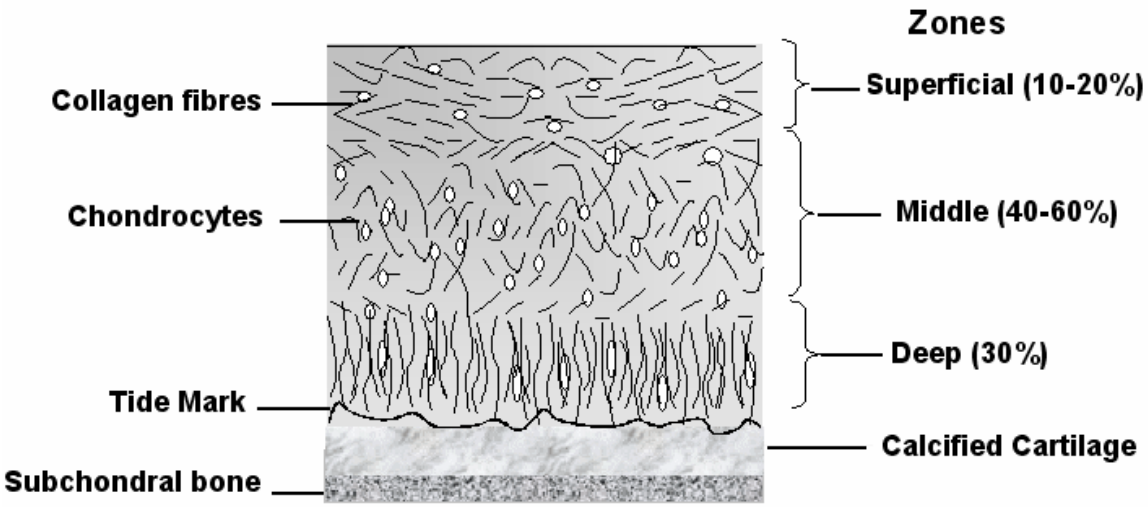

Figure 2-2. Layered structure of cartilage collagen network in three separate zones.

2.1.2 Theoretical Models of Articular Cartilage

When object is subjected to an external load, it will move and deform. Two types of physical quantities are necessary to determine the deformational response of a material body: stress and strain. Generally speaking, when an object is under load, theoretical models and mathematical analyses are required to determine the states of stress and strain within the object. To describe the mechanical properties, some independent material coefficients are necessary to be determined, such as Young's modulus, and Poisson's ratio.

Indentation is a widely used technique to measure the mechanical properties of articular cartilage. However, the mechanics of modeling the indentation experiments of cartilage-on-bone configuration is very complex because of the multidimensional deformations in the layer of tissue as well as the biphasic nature of the tissue. Due to the mathematical

difficulties involved in modeling the indentation test, the derivation of meaningful material properties from indentation tests of articular structure is also very complicated. Theoretical modeling of articular cartilage has evolved from single phasic models to biphasic and multiphasic models. In these models, the properties and the mechanics of the structural elements of articular cartilage (such as the collagen fibrils) were introduced into the constitutive equations through experimentally derived material parameters. Pathological degeneration of articular cartilage is likely to be governed by structural changes at the molecular level; therefore, molecular-based theories have been developed in an attempt to understand the mechanical behavior of degenerated cartilage.

2.1.2.1 Single-phasic model

Early investigators have tried to obtain elastic constants from indentation test by assuming a uniaxial stress field beneath the indenter. This assumption ignores important edge effects occurring with indenters that have contact areas with diameters comparable to the cartilage thickness. Hayes et al. (1972) first considered the indentation mechanics of an infinite elastic layer bonded to a rigid half-space as a model for the layered geometry of cartilage and subchondral bone. Articular cartilage is modeled as a linearly elastic, homogeneous, and isotropic material, indented by the plane end of a rigid circular cylinder or by a rigid sphere. The elastic infinite layer deforms under the action of a rigid axisymmetric punch pressed normal to the surface by a uniaxial force *P* (Figure 2-3). No friction is assumed between the punch and the layer. For a plane-ended cylindrical

indenter, at a given value of the parameters *a/h* and *v*, the relation between the applied force *P*, and the displacement, ω_0, is given by

$$G = \frac{P(1-\nu)}{4a\omega_0\kappa(a/h,\nu)} \qquad (2\text{-}1)$$

in which *a* is the radius of indenter, *G* is shear modulus, *h* is thickness of cartilage, and *v* Poisson's ratio. Values of the scale factor κ were numerically determined by Poisson's ratio *v* ranging from 0.3 to 0.5 (Hayes et al. 1972) and from 0.0 to 0.3 (Jurvelin et al. 1990). These values of κ were later validated by finite element simulation and widely adopted in the calculation of the relationship between the load *P* and the indenter displacement ω_0 of articular cartilage as well as on forearm (Zheng and Mak 1996), and plantar foot (Zheng et al. 2000).

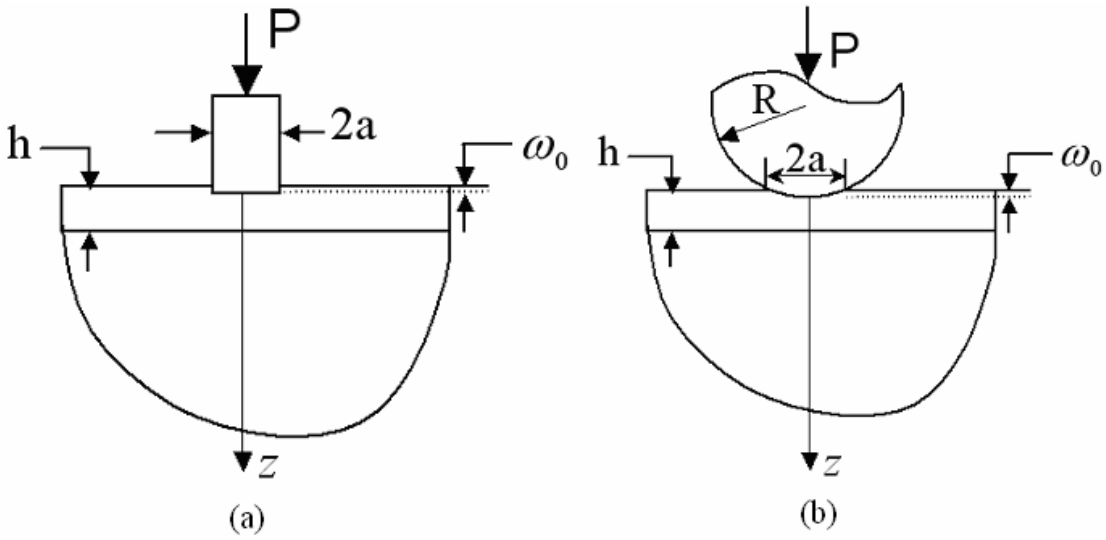

Figure 2-3. Geometries for the plane-ended cylindrical indenter (a) and the spherical indenter (b).

In this mathematical model, cartilage properties can be described by a single value of the elastic modulus, if a specific Poisson's ratio is assumed. Using this linear elastic model, cartilage response is time independent – that is, it does not exhibit creep or stress relaxation. Thus, it is only useful in two limited cases, one is to predict the instantaneous response to a step load, and the other is to predict the asymptotic deformation in creep tests. Both applications should be confined to small loads to stay within the limits of small-strain assumption. This theory is quantitatively comparable to some of the experimental results on bovine patellar cartilage. Hayes' mathematical model of indentation was extended from linear elastic model to viscoelactic model by Parsons and Black (1977, 1979). They combined the thin elastic-layer indentation solution with a Kelvin-type viscoelastic solid with a continuous retardation spectrum using the Boltzmann superposition principle to study the viscoelasticity of articular cartilage.

Finite element analysis has been employed to study this mathematical model (Galbraith and Bryant 1989, Zhang et al. 1997). The effect of model geometry and deformable substrate of articular surface was examined using a linear elastic finite element model (Galbraith and Bryant 1989). They reported that the results of the indentation analysis were unaffected if the radius of the tissue was at least three times the radius of the indenter, and if the thickness of the substrate was at least sixteen times the tissue thickness. A 2-D nonlinear finite element model was developed to investigate the influence of friction between the indenter and cartilage surface, and large deformation, on the calculation of the effective Young's modulus (Zhang et al. 1997). A new κ table was

given for the flat-ended indentation test with consideration of the larger deformation effect. The simulation results indicated that the effect of friction in the calculation of effective Young's modulus became significant with a large aspect ratio and with a large Poisson's ratio. It was found that the values of κ increased almost proportional to the increase of indentation depth, especially obvious with larger Poisson's ratio and larger area aspect ratio a/h. By using the new table of κ values, the effect of finite deformation (up to 20%) could be corrected.

2.1.2.2 Biphasic model

With Hayes's solution, one can calculate the Young's modulus for cartilage with an arbitrarily chosen Poisson's ratio. However, for articular cartilage, the choice of Poisson's ratio causes a major uncertainty in the determination of Young's modulus or shear modulus. This elastic analysis, which regards articular cartilage as a sing-phased medium, cannot predict time-dependent behavior. Articular cartilage, from the mechanical point of view, is a biphasic material, which exhibits viscoelastic behavior under compressive loading because the interstitial fluid flows within the tissue and across the tissue surface. To appropriately interpret the viscoelastic behavior of articular cartilage during creep indentation test or stress-relaxation indentation test, a biphasic indentation mathematical model was solved by Mak and coworkers (1987).

In this biphasic model solution, articular cartilage is modeled as being composed of an impressible, isotropic, linearly elastic solid and an impressible inviscid fluid, i.e. the

linear KLM model for articular cartilage. A mathematical solution for the biphasic stress-relaxation and biphasic creep indentation problems was proposed. The thin layer of articular cartilage is assumed to be bonded to an impervious-rigid substrate. The indenter is assumed to be cylindrical, flat-ended, rigid, frictionless, porous, and free-draining, which is different from the Hayes's model. There are three coefficients for biphasic material to be determined: aggregate modulus H_A, Poisson's ratio v, and permeability k. The aggregate modulus represents the compressive stiffness of the solid phase, Poisson's ratio is a measure of the lateral relative to the axial strain of the solid phase, and the permeability is a measure of the ease with which fluid flows through the matrix.

Mow et al. (1989) developed a numerical algorithm to compute all three material coefficients from the creep indentation experiments using biphasic indentation model for articular cartilage. This solution, for the first time, can determine simultaneously all three *in situ* coefficients of intrinsic material properties (H_A, v, k) of articular cartilage. However, it was found that the early time response of creep usually differs from the best curve-fit solution. And the more, the linear KLM biphasic theory is not able to account for the observed different rate for creep and recovery. It may be due to the nonlinear strain-dependent permeability of the biphasic material, and those assumptions, such as frictionless porous indenter, and regarding articular cartilage as an isotropic and homogeneous material.

Based on the assumption of linear infinitesimal deformation in Mak's solution, Suh and Spilker (1994) examined the finite deformation response for stress relaxation problem using either a porous or solid indenter. Differences between the finite deformation response and the linear response are shown to be significant when the compression rate is fast or when the indenter is permeable. Besides the cylindrical, flat-ended indenter used in the biphasic indentation modeling, Hale et al. (1993) investigated the biphasic mechanical property deficits using a rigid, impermeable, spherical ended indenter. Use of a spherical indenter avoids stress singularity under the edge of the indenter, but introduces geometric nonlinearity since the engaged portion of the indenter surface area changes as the solution develops. The spread of cartilage engagement by the spherical ended indenter is modeled by successively imposing an impenetrable kinematic boundary condition at cartilage surface area for which incipient indenter surface penetration is detected. For each indentation test, a least-squares-error curve fitting procedure is used to identify a set of those biphasic coefficients.

Generally speaking, this biphasic indentation solution is a successful method to determine all the three coefficients for the biphasic articular cartilage material. However, it is a quite formidable computational task. Closed-form mathematical approximations of the deformation were presented for the cases of plane indentation by a rectangular block and three-dimensional indentation by a plane-ended cylinder (Haider and Holmes, 1997). The approximations are analyzed in the context of a static indentation test by comparison of applied load values to those obtained using a classical integral transform solution. The

advantage of this approach is that it yields closed-form approximations of the static indentation solution which can also capture the essential singular behaviour.

Finite element analysis has also proven to be a useful tool to simulate and analyze the biphasic indentation problem. Spilker et al. (1992) studied the stress-relaxation problem using finite element analysis. The following issues were considered: 1) the indenter is porous, free-draining or impermeable, solid; 2) the interface between the indenter and the articular cartilage surface is frictionless or totally adhesive; 3) tissue is thin or thick. The effects of the stiffness of the subchondral bone and a curved tissue-subchondral bone interface were also studied. It was found that, for a long time scale, the reaction force reaches a larger peak value for the solid indenter in comparison with the free-draining indenter, and is larger for the adhesive indenter compared with the lubricated indenter. The permeability of the indenter does not affect the equilibrium value of the reaction force, while for the adhesive indenter, the equilibrium reaction force is larger. Since this equilibrium value would be used to determine the solid phase properties, the assumption made in analytic models of a lubricated indenter would have about a 10% effect on the predicted properties. While these effects are present for both thin and thick tissues, they are shown to be more significant for the thin tissue. For the effect of a curved tissue - subchondral bone interface, the physiologically representative levels of bone-tissue interface curvature was studied, and the predicted tissue response in regions away from the curved geometry was found being virtually unchanged. Donzelli et al. (1992) proposed an automated, adaptive, finite element solution of the governing biphasic

equation. This finite element formulation is based on a mixed-penalty approach in which the penalty form of the continuity equation for the mixture is included in the weak form. The accuracy and effectiveness of this adaptive finite element analysis is demonstrated using two-dimensional axi-symmetric problem corresponding to the unconfined compression of a cylindrical disk of soft tissue and the indentation of a thin sheet of soft tissue. It was shown that this method could effectively capture the steep gradients in both problems and produce solutions in good agreement with independent, converged, numerical solutions. Wu et al. (1998) evaluated the finite element software ABAQUS for biomechanical modeling of biphasic soft tissues. For the unconfined indentation problem, a cylindrical cartilage layer is ideally bonded to an impermeable, rigid subchondral bone. The cylindrical indenter is assumed to be rigid, porous, and frictionless. The specimen is modeled using axi-symmetric, poroelastic elements because of the symmetry of the problem. The indenter is prescribed a displacement history. The reaction force on the indenter is predicted as a function of time. The pore pressure at the top and the side surface of the cartilage disc is set to zero to simulate a free draining of the interstitial fluid from the cartilage. Their simulated results suggest that the biphasic cartilage model can be implemented into the commercial finite element software ABAQUS to analyze practical joint contact problem with biphasic articular cartilage layers.

A significant finding by using biphasic indentation solution is that, the *in situ* Poisson's ratio of cartilage may be much smaller than those determined from the measurements performed on excised osteochondral plugs reported in the literature (Mow et al. 1989).

The available data on Poisson's ratio reflect some important characteristics of cartilage: a) it varies with species and location; b) it almost always falls outside the 0.4 to 0.5 range, the commonly assumed range; c) prior estimates of Poisson's ratio in the range 0.4 to 0.5 may lead to significant errors in calculating the aggregate modulus. For isotropic biphasic material, a measure of the column efflux of fluid through the tissue when it is compressed is Poisson's ratio. For a biphasic material with $\nu = 0.5$, no fluid flow can occur, and thus no creep and stress-relaxation behaviors are possible. The species and anatomic site variation of Poisson's ratio over the joint surface may in fact reflect the fluid efflux requirement at a specific location on the joint surface for purpose of joint lubrication (Mow and Hayes 1997).

Triphasic theory (Lai et al. 1991) is an extension of the biphasic theory which incorporates an ion phase into to the solid and fluid phases of the biphasic theory. Adding ion species to the biphasic model has helped in reproducing selected experimental results; however, the model remains macroscopic and is disconnected from the microscopic, molecular structure of cartilage. Recent progress in the understanding of microscopic and molecular structures of cartilage, as well as the realization that pathologic degeneration of cartilage is ultimately at the molecular level, have led to the development of molecular-based models incorporating interactions between the microscopic structural details (Buschmann and Grodzinsky 1995; Kovach 1996).

2.2 Indentation Test – Instruments and Applications

2.2.1 Mechanical Indentation

To perform indentation experiments on various articular cartilage specimens, different kinds of indentation apparatuses have been developed. For the *in situ* experiments, mechanical indentation apparatuses are generally used (Mow et al.1989; Kempson et al. 1971; Hori and Mockros, 1976; Newton et al. 1997; Arokoski et al. 1994, 1999). Figure 2-4 shows a typical mechanical indentation instrument developed by Shepherd and Seedhom (1997). These instruments usually use a linear variable differential transducer (LVDT) to monitor the indentation depth, a load cell to record the indentation force, and a needle probe to measure the cartilage thickness.

Mechanical indentation apparatuses have been used to perform various indentation tests, such as on the human femoral head *in vitro* to distinguish between visually normal and fibrillated cartilage (Kempson et al. 1971), on the human tibial condyle *in situ* to study the difference between the normal and osteoarthritis or degenerative joint diseased articular cartilage(Hori and Mockros, 1976), on the canine tibial plateau to observe the effect of long-term exercise on canine knee (Newton et al. 1997), and on canine femoral and tibial cartilage *in situ* to analyze the interrelationships between the structure, composition and mechanical properties of articular cartilage (Arokoski et al. 1994, 1999). An automated creep indentation apparatus was used to investigate articular cartilage of the human elbow to study the potential relationship to osteochondritis dissecans (Schenck et al. 1994), hip cartilage in experimental animal model (Athanasiou et al. 1995b),

biomechanical properties of human ankle cartilage (Athanasiou et al. 1995a, 1999), and effects of aging and dietary restriction of rat articular cartilage (Athanasiou et al. 2000).

Mechanical indentation apparatuses are quite fine instruments for mechanical assessment of articular cartilage *in vitro* or *in situ*. However, they are limited in performing indentation tests *in vivo* due to the complexity of compositions of those apparatuses. The needle probe technique allows in situ thickness measurements, but at the site of measurement the tissue is destructed, restricting further use of the specimen.

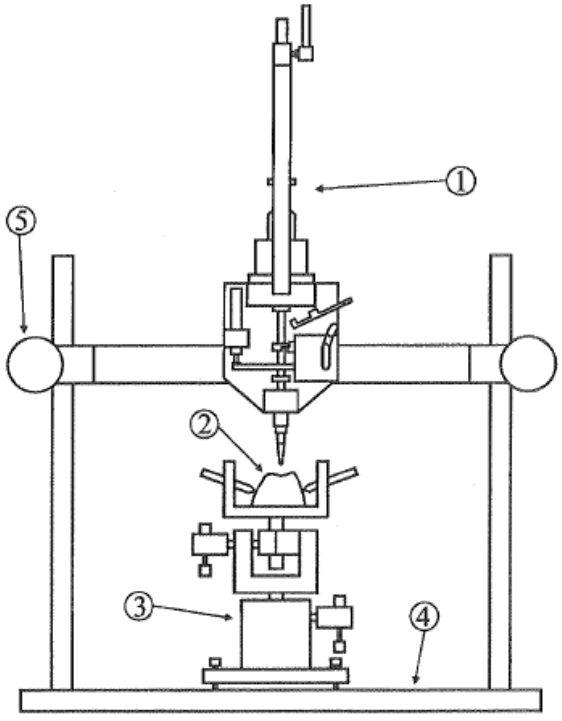

Figure 2-4. A typical mechanical indentation machine and associated equipment (1 indentation mechanism; 2 specimen; 3 specimen holder; 4 base; 5 height adjustment for machine) (Shepherd and Seedhom 1997).

2.2.2 Arthroscopic Indentation

Lyyra et al. (1995) developed a new indentation instrument for the quantification of cartilage stiffness under arthroscopic control, with which objective measurements of cartilage stiffness can be made to diagnose the softening of articular cartilage at an early stage in clinic. The instrument is composed of a measurement rod joined to a handle (Figure 2-5). The rod has an inclined flat ended reference plate with a cylindrical plane-ended indenter in the centre of the inclined surface. The force applied to the indenter is measured through bending of the beam by a pair of strain gauge transducers. The pressing force by which the surgeon presses the flat inclined surface of the instrument against the cartilage surface is measured by another pair of strain gauges. During arthroscopy the measurement rod is pushed with a trocar through the soft tissue into the knee joint, pressing perpendicular to the cartilage surface to a depth of 300 μm, using a 10 N force. Then the mean indenter force for 1 s after load application is used as an indicator for cartilage stiffness. If a significant stress-relaxation occurs within the first second of the measurement, the maximum indenter force at the beginning of the 1 s period is used. It was found that the indenter force was virtually independent of the cartilage thickness, when cartilage was thicker than 2 mm.

Arthroscopic stiffness measurements were carried out using three human cadaver knees (Lyyra et al. 1995). Measurements were validated using a stress-relaxation indenter instrument. The arthroscopic stiffness showed a good correlation with the reference measured shear modulus. This instrument was used to characterize for the first time the topographical variation of the stiffness of the human knee articular cartilage *in vivo*

(Lyyra et al. 1999b), and the stiffness variation was consistent with earlier laboratory biphasic indentation measurements with the knee joint cartilage of cadavers. The stiffness change for enzymatically-degraded cartilage of bovine knee was also measured using this novel indentation instrument *in vitro* (Lyyra et al. 1999a).

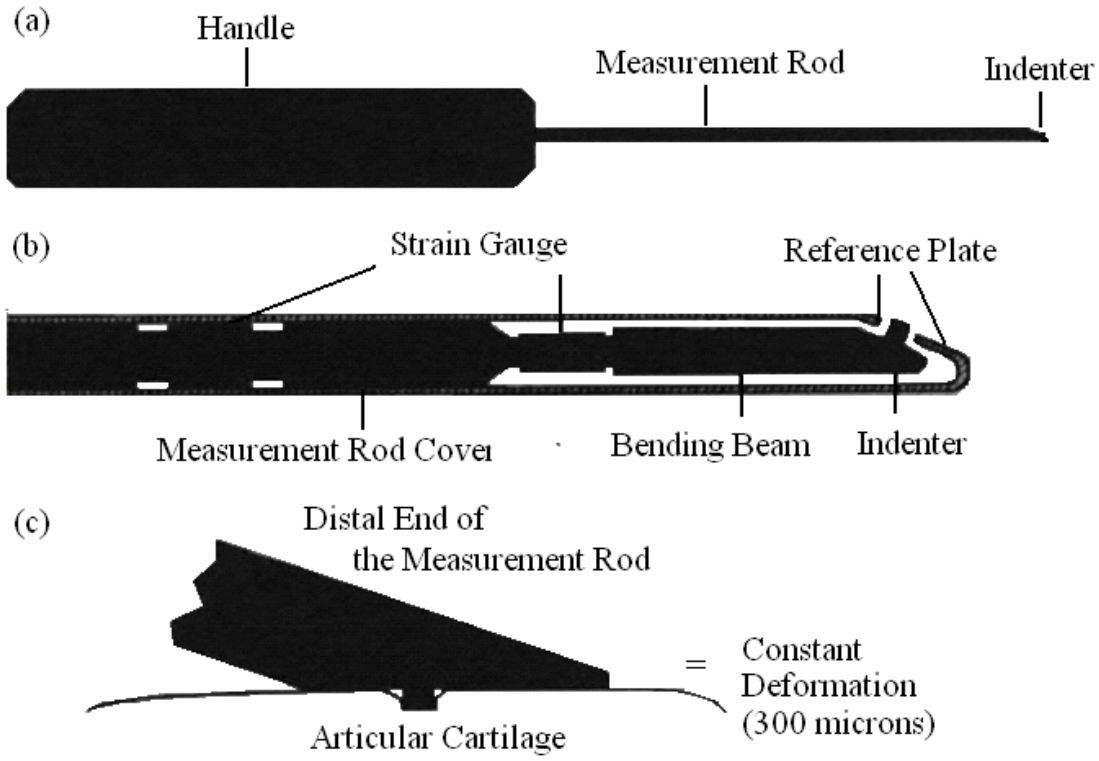

Figure 2-5. (a) Schematic presentation of the arthroscopic indentation instrument; (b) longitudinal section of the measurement rod showing localization of strain gauge transducers; (c) indentation geometry for the arthroscopic measurement of cartilage stiffness (Lyyra et al. 1995).

This arthroscopic indentation instrument is suitable for clinical use. However, the cartilage thickness is normally not known, so the measured stiffness is just only an

indicator, not the real shear modulus. Toyras et al. (2001) introduced ultrasound to measure the thickness of articular cartilage, and with the stiffness obtained from the arthroscopic indentation, the Young's modulus of articular cartilage was estimated.

2.2.3 Ultrasound Indentation

Considering the ability of ultrasound in measuring the thickness of articular cartilage (Adam et al. 1998, Toyras et al. 2001) and assessing the mechanical properties of soft tissue (Zheng and Mak 1996, Han et al. 2003), Suh et al. (2001) studied the potential applications of ultrasound for an ultrasonic indentation test of articular cartilage. The accuracy of ultrasound in measuring the cartilage thickness is limited by the lack of an accurate measurement of the ultrasound speed of cartilage, for the ultrasound speed varies according to the pathological conditions of the tissue. An *in situ* calibration method was developed to predict the true ultrasound speed of cartilage, thus allowing the ultrasound transducer to measure the thickness with great accuracy. The accuracy of the *in situ* calibration method was indirectly validated by comparing the cartilage thickness obtained using ultrasound with that obtained using a direct microscopic optical method (Jurvelin et al. 1995).

Generally, an ultrasound indentation testing system consisted of a miniature ultrasound contact transducer, a low capacity load cell, and a precision micrometer head (Zheng et al. 1996, Laasanen et al. 2002). By simultaneously implementing an indentation testing protocol and using the ultrasound transducer as an indenter, this method can provide an indentation stiffness measurement of cartilage. During indentation, thickness and

deformation of the cartilage are detected in real-time from the ultrasound signal using the pre-defined value for speed of sound and the information on the ultrasound flight time from the bone-cartilage interface. Subsequently, the instantaneous Young's modulus of articular cartilage is calculated (Laasanen et al. 2002). Figure 2-6 presents the measurement geometry of the ultrasound indentation instrument for the measurement of mechanical properties of articular cartilage.

Ultrasound indentation enables a simultaneous measurement of tissue thickness, indentation deformation and force and, thereby, quantification of tissue intrinsic mechanical properties (Korhonen et al. 2003). This technique has been used to study the degeneration of bovine knee cartilage (Laasanen et al. 2003a, 2003b), and spontaneously degenerated bovine articular cartilage (Saarakkala et al. 2003). However, it is still not possible to accurately measure the speed of ultrasound for cartilage with the present technique. Although the *in situ* calibration method proposed by Suh et al. (2001) provides the measurement of tissue thickness, stiffness and speed of sound, the apparent complexity of the instrumentation limits the clinical applicability of this calibration method. The pre-defined ultrasound speed remains a problem for such an ultrasound indentation instrument (Toyras et al. 2003).

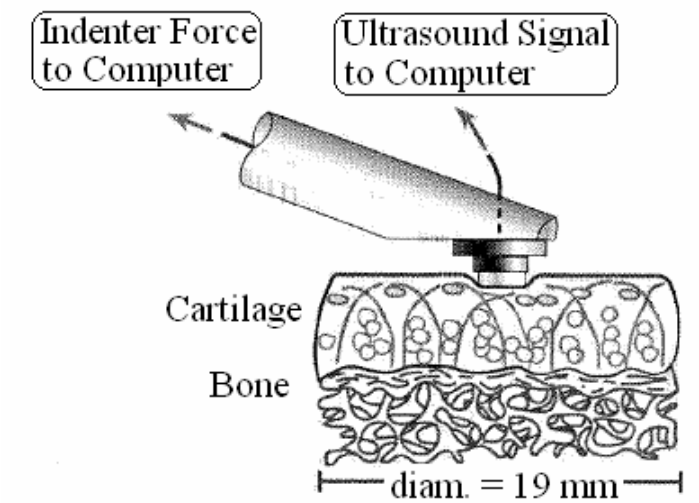

Figure 2-6. Measurement geometry of the ultrasound indentation instrument for the measurement of mechanical properties of articular cartilage (Laasanen et al. 2002).

Accurate knowledge of test tissue thickness is an essential issue for the analysis of mechanical properties of articular cartilage. Three methods are currently available for the measurement of thickness in those indentation instruments including optical, needle probe and ultrasonic techniques. The optical method uses a stereomicroscope (Jurvelin et al. 1990) while the needle probe method employs a sharp needle penetrating perpendicularly to cartilage surface, and the ultrasonic technique is based on the determination of time delay of echoes arising from the articular surface and tidemark. Jurvelin et al. (1995) compared these methods. By performing experiments on canine and bovine knee articular cartilage, the measured thicknesses using these three methods were found showing a high correlation. However, each of the methods has its own restriction. For the optical method, rupturing of the fibrous structure of articular cartilage during specimen preparation may produce extra swelling of the tissue when immersed in

aqueous solution and cause an artificial increase in the measured thickness. Due to the puncturing of the tissue the needle probe method is normally suitable only if cartilage thickness is not necessary before mechanical tests. Also, destruction of the tissue structure at the site of measurement restricts the further use of the specimen. As to the ultrasonic technique, a constant ultrasound speed in articular cartilage must be assumed. However the speed strongly depends on the density and elastic modulus of the cartilage. Therefore, efforts for developing indentation instruments to provide accurate and repeatable indentation measurements *in vivo* are quite necessary. In addition, the mechanical properties of articular cartilage are site-dependent, so the specimens or testing sites for experiments should be properly chosen.

2.2.4 Nanoindentation

Both mechanical indentation and ultrasound indentation are useful to measure the mechanical properties of soft tissues, however, it is not common to use these contact indentation techniques to image the distribution of elastic modulus for a region of tissue due to the restrictions of their low spatial resolution (typically greater than 2 mm) and long measurement time, as the measurement needs to be taken point by point (Vannah et al. 1999; Appleyard et al. 2001). Nanoindentation techniques have been developed for the measurement of the mechanical properties of materials on their surface (Pethica et al. 1983). They have also been used for the microscopic mechanical assessment of hard biological tissues including bone (Rho et al. 1997; Ferguson et al. 2002) and tooth (Habelitz et al. 2001), and for the study of spinal fusion quality by evaluating the

hardness of the host tissues and implanted materials within the fusion complex (Guo et al. 2001). But nanoindentation cannot provide information inside tissue. The sample surface should be well prepared for nanoindentation test, and the results rely much on the selection criteria of sampling, and hence it is difficult to use for most biological tissues, especially soft tissues (Guo et al. 2001).

2.3 Ultrasound Elastography

The material properties of Articular cartilage are anisotropic, nonhomogeneous, and viscoelastic. The properties vary with location within the cartilage and with the joint and species of origin of the tissue. Ultrasound elastography, provides a technique to map the material properties such as Young's modulus, Poisson's ratio and viscoelsticity inside soft tissues along the transducer axis in an anatomically meaningful presentation to provide useful clinical information. The medical applications of ultrasound elastography technique range from tumor detection (Garra et al. 1997) to the study of skeletal muscle contraction (Krouskop et al. 1987), from the assessment of vascular health (Lerner et al. 1990) to the renal transplant rejection (Yamakoshi et al. 1990), from the diagnosis of spine tissues (Kawchuk et al. 2001) to the assessment of corneal tissues (Hollman et al. 2002). Research in ultrasound elastography typically relies on 1-10 MHz ultrasound, and elasticity imaging at these frequencies can provide strain maps with a resolution on the order of millimeters. This is not sufficient for applications to skin, articular cartilage or other fine structures. High-resolution elasticity measurements may be achieved by the utilization of high-frequency (larger than 50 MHz) ultrasound (Cohn et al. 1997a, 1997b, 2000; Fortin et al. 2000; Zheng et al. 2004).

Ultrasound elastography techniques can be grouped according to their stimulation methods to the tissue. The stimulus to the motion could be externally applied (in most current applications, by applying pressure with the transducer), generated by the actual tissue itself, such as the contraction of myocardium, or be the result of nearby intrinsic motion, such as the response of the liver to nearby aortic and cardiac pulsation. Currently, ultrasound elastography techniques fall into two main groups: those using a quasi-static, externally applied force, and those using a periodic excitation, which may be externally applied or naturally generated in the tissue itself.

2.3.1 Quasi-static Elastography

Ophir et al. investigated the tissue mechanical properties imaging and proposed a new diagnostic method termed elastography to image tissue strain when under a certain loading (Ophir et al. 1991, 1997, 1999, Ce'spedes et al. 1993). The basic principle of elastography is to compress soft tissue using an ultrasound transducer or the transducer/ compressor combination (Figure 2-7), and collect the ultrasound echoes before and after the compression. Pairs of echoes scattered from tissue are analyzed using cross-correlation algorithm to estimate the local strain of the compressed tissue.

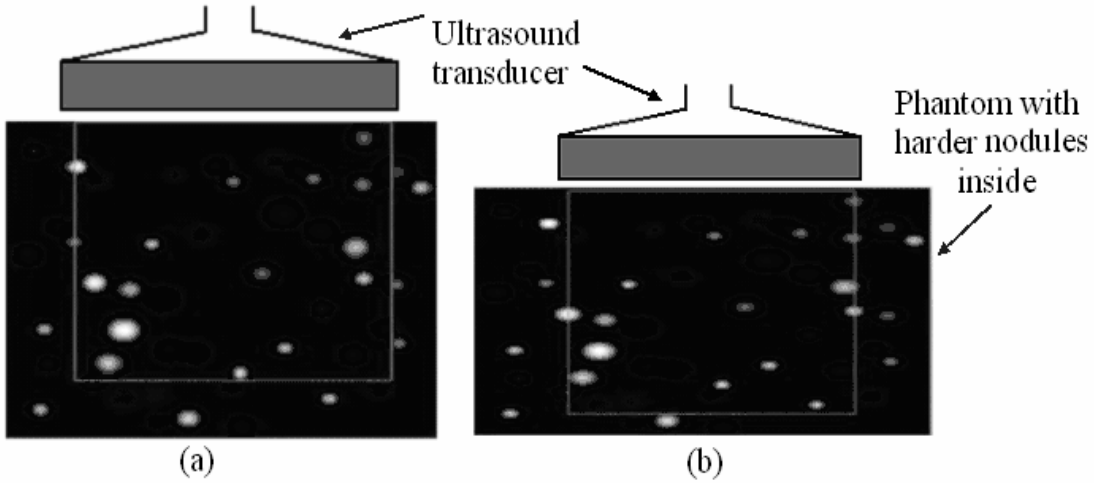

Figure 2-7. Quasi-static elastography: tissue strain estimation. Ultrasound transducer array compressed to the phantom: (a) before compression; (b) after compression (Ophir et al. 1991).

The first radio frequency A-line is obtained by the transducer slightly pre-compressing the tissue to ensure good contact. The second radio frequency A-line is obtained after axially compressing the tissue a small amount (about 1 per cent or less of the tissue depth). The echoes are then subdivided into small temporal windows that are compared pairwisely by using cross-correlation techniques, from which the change in arrival time of the echoes before and after compression can be estimated. Due to the small magnitude of the applied compression, there are only small distortions of the echo lines, and the changes in arrival times are also small. The local axial strain is estimated as:

$$e_{local} = \frac{(t_{1b} - t_{1a}) - (t_{2b} - t_{2a})}{t_{1b} - t_{1a}} \qquad (2\text{-}2)$$

Where t_{1a} is the arrival time of the pre-compression echo from the proximal window, t_{1b} is the arrival time of the pre-compression echo from the distal window, t_{2a} is the

arrival time of the post-compression echo from the proximal window and t_{2b} the arrival time of the post-compression echo from the distal window. The windows are usually translated in small overlapping steps along the temporal axis of the echo line, and the calculation is repeated for all depths. The method is based upon the assumption that speckle motion adequately represents the underlying tissue motion for small uniaxial compressions (Wilson and Robinson 1982).

This kind of elastography technique uses an external, quasi-static stimulus, measures compression as a spatial gradient of tissue displacement, and performs all computations in the spatial domain. The group led by Ophir developed many methods, such as signal stretching technique to improve the accuracy and resolution of elastograms (Ce´spedes et al. 1993, Ce´spedes and Ophir 1993, Varghese and Ophir 1997). In elastography, the mapping of the elastic modulus distribution in tissue is replaced by mapping the distribution of strains. This process is governed by the basic physics as expressed in the elasticity equations, which are dependent on the modulus distribution itself, the details of the applied compression, and the boundary conditions. If a simple (but generally inaccurate) assumption of stress constancy and a semi-infinite target are made, there is an inverse proportionality between the modulus distribution and the strain distribution. However, this assumption generally results in significant mechanical artifacts in the elastogram. A 2-D analytical model developed by O'Donnell (1994) combined with additional information could be used to reduce the level of the mechanical artifacts. That is, given Young's modulus as a function of position, to predict the strain inside tissue

given specific forces and boundary conditions by assuming the tissue to behave as an inhomogeneous isotropic linear elastic and incompressible medium. The group suggested using large deformation to maximize the signal-to-noise ratio (SNR) of the displacement and strain estimations. However, large displacement (over 10 wavelength of the carrier signal) results in significant internal strain, which changes the spatial distribution of the scatterers within an area of the image, thus decorrelating the speckle patterns used for cross-correlation. Instead, they used multiple small step deformations (each step was less than one wavelength) to produce a large total deformation. The total displacement was then calculated by accumulating the displacement between each small deformation (Skovoroda et al. 1994). The method has later extended (Hamilton et al. 1998) and results of experiments with enhanced contrast resolution were reported.

Based on the research on standard elastography, i.e. mapping the local axial strain of soft tissues assumed as linear elastic, single-phase, isotropic and incompressible, lateral strain elastography (Kallel and Ophir 1997a, Konofagou and Ophir 1998), modulus elastography (Kallel and Ophir 1997b) and Poisson's ratio elastography (Konofagou and Ophir 1998, Stafford et al. 1998) were reported and results of simulation and experiments were presented by the research group led by Ophir. In recent years, they have extended their investigation to demonstrate the feasibility of elastography technique of estimating and imaging poroelastic material properties, such as poroelastic properties (Konofagou et al. 2001), Poisson's ratio (Righett et al. 2004) and permeability of porous media (Righett et al. 2005) using homogeneous and nonhomogeneous phantoms. This provides a unique

type of methods in mapping the mechanical properties of biphasic materials although the resolution of the elastograms should be improved before the method is used to assess articular cartilage.

Doley et al. (2001) developed a prototype freehand elstographic imaging approach. The system was used for clinical breast imaging. It consists of a fast data acquisition system, which is able to capture sequences of intermediate frequency echo frames from a commercial ultrasound scanner while the breast is deformed using hand-induced transducer motion. 2-D echo tracking is used and elastograms are produced. Varghese et al. (2002) developed a handheld, portable stepper motor controlled system for elastography. The system may reduce motion and jitter errors that are prevalent in completely “freehand elastography” that employs hand-induced compression using the transducer. The stepper motor controlled system provides controlled compression and synchronized data acquisition. Elastograms of phantom and liver tissue were presented by the authors.

2.3.2 Dynamic Elastography

The vibration amplitude sonoelastography (sonoelasticity imaging) was first presented by Lee et al. in 1991. In this method, a low frequency vibration (20 – 1000 Hz) is applied externally to excite internal vibration within the under inspection (Figure 2-8). When a discrete hard inhomogeneity, such as a tumor, is present within a region of soft tissue, decreased vibration amplitude will occur at its location. Doppler detection algorithms are

employed to make a real-time vibration image. Studies on liver, breast, and kidney tissue were published by Lee et al. (1991). Huang et al. (1992) and Walker et al. (1993) extended this work to "real-time" estimators of vibration amplitude, phase and frequency that could be used for a variety of vibration sonoelastography techniques. A real time, *in-vitro* study of the prostate conducted by Rubens et al. (1995) demonstrated that vibration amplitude sonoelastography had a better sensitivity and predictive value than doing B-scan imaging alone. Taylor et al. (2000) reported that three dimensional sonoelastography reconstructions were finished. The principles and practices *ex-vivo* and on prostate phantom were presented.

Vibration amplitude sonoelastography detects a hard lesion by looking at the disturbance of the vibration amplitude pattern. In practice, the lowest frequency is preferred, as it is the easiest to excite and to interpret. Various time and frequency estimators make this technique a real-time diagnostic tool. Vibration amplitude sonoelastography is currently in an early stage of *in vivo* trials using real-time imaging techniques.

Sato et al. (1985) studied the nonlinear interaction between ultrasound and low-frequency waves in tissue, and developed a vibration-phase gradient approach to build sonoelastography (Yamakoshi et al. 1990). This technique maps both the amplitude and the phase of low-frequency wave propagation inside tissue. From these maps, the wave propagation velocity and dispersion properties are derived. These parameters are directly linked to the elastic and viscous characteristics of tissue. The tissue vibration amplitude

and phase of tissue motion may be estimated from the ratio of adjacent harmonics. Phase and amplitude maps constructed as a function of time permit the display of wave propagation as a moving image. Images of amplitude and phase are computed offline using a minimum-square-error algorithm to estimate the direction of wave propagation and to calculate phase and amplitude gradient in this direction. A large number of *in-vivo* and animal studies of the propagation of 100 Hz shear wave have been done and results were reported (Yamakoshi et al. 1990) with the assumption that the effect of shear viscosity is negligible at low frequency.

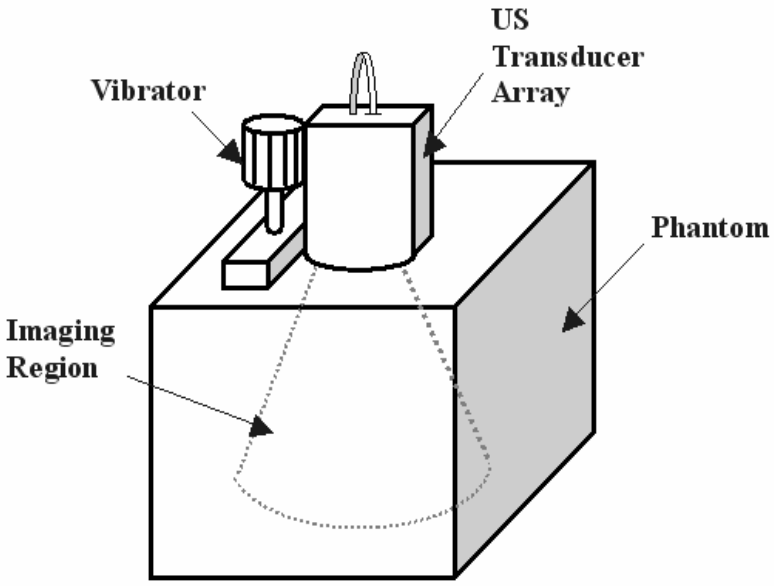

Figure 2-8. Dynamic elastography: low frequency vibration method. System setup: Vibrator is placed at left side of ultrasonic array (Lee et al. 1991).

Levinson (Levinson et al. 1995) adapted and refined Sato's technique (Yamakoshi et al. 1990) by using a more general model of tissue visco-elastisity, and a linear-filtering. Based on the assumption that the effect of shear viscosity is negligible at low frequency, Levinson conducted a series of experiments on the quadriceps muscle group in human thighs. Values of Young's modulus of elasticity were calculated from phase gradient images under conditions of active muscle contraction. A pulley apparatus was used to control the tension applied to the muscle.

Catheline et al. (1999) studied the directivity patterns of shear waves produced by the usual vibrators during their propagation in the soft tissue. Sandrin et al. (2002a) developed a new method for measuring the shear velocity in soft tissue different from the techniques discussed above in which the ultrasonic transducer and the low frequency vibrator are two separate parts. This method relies on a probe that associated the vibrator and the transducer, which is built on the axis of the vibrator. The low frequency shear wave is driven by the transducer itself while it is used in pulse-echo mode to acquire ultrasonic lines. The problem is that the absolute displacements within the tissue are not direct because the transducer vibrates. The measured displacement of a tissue equals the absolute displacement induced by the shear wave minus the relative displacement of the transducer itself. By measuring a motionless interface relative displacement, or deducing the vibrator displacement from the relative displacement of a deep echo when no motionless object echo is present upon the assumption that the elastic wave attenuation is sufficient for the displacements to be negligible at a certain depth in the tissue, the

vibrator displacement can be derived and compensated, and the shear velocity can be correctly estimated which is linked to Young's modulus of tissue. They presented 2-D shear modulus maps obtained from tissue-equivalent material (Sandrin et al. 2002b). Tanter et al. (2002) studied both axial and lateral displacements in human tissues during the shear wave propagation induced by low frequency vibrators and thus improved Young's modulus image reconstruction. This technique is based on multisynthetic aperture beam-forming. The beam-forming is achieved in the receive mode on two independent subapertures. Comparison of successive frames by a classical 1-D speckle tracking algorithm allows estimation of displacements along two different directions linked to the subaperture beams.

Different from those techniques that are based on low frequency vibration sonoelastogram which usually employ mechanical or handheld vibrators to induce the low frequency vibration of tissue, acoustic radiation force is also used to induce tissue motion. Nightingale et al. (1995) reported the feasibility of a technique based on radiation force and acoustic streaming to distinguish cysts from solid lesions. Acoustic radiation force is a unidirectional force that is applied to absorb or reflect targets in the propagation path of an acoustic wave. This phenomenon is caused by a transfer of momentum from the acoustic wave to the propagation medium. When the target is both absorbing and has a scatter that acts as a reflector, the radiation force is entirely in the direction of wave propagation. In tissue, assuming the plane wave propagation, the radiation force is:

$$F = \frac{2\alpha I}{c} \qquad (2\text{-}3)$$

Where F is radiation force, c is the speed of sound in the medium, α is the absorption coefficient of the tissue, and I is the temporal average intensity of the acoustic beam at a given point in the tissue. For a focused acoustic beam propagating through soft tissue, the "target" is the tissue, and the force is applied throughout the focal region of the acoustic beam (Wells 1977, Muir and Carstensen 1980, Nyborg 1965, Wu and Du 1993, Starritt et al. 1989).

In the acoustic radiation force induced vibration elastography system, a single focused ultrasound beam is used to apply localized radiation force within tissue, and the resulting tissue displacements are mapped using ultrasonic correlation based methods. The tissue displacements are inversely proportional to the stiffness of the tissue, and thus a stiffer region of tissue exhibits smaller displacements than a more compliant region. The displacement images are directly correlated to local variations in tissue stiffness with high contrast. Results of the experiments on human breast, human abdomen, human biceps, human thyroid and tissue mimicking phantom had been reported by Nightingale et al (1999, 2002).

Sarvazyan et al. (Sarvazyan et al. 1998, Barannik et al. 2002) reported an approach named shear wave elasticity imaging to image and characterize tissue structures based on the use of acoustic wave remotely induced by the radiation force of a focused ultrasonic beam. The mechanical response of tissue to radiation force is detected using a modified ultrasound Doppler technique. The induced shear strain is detected to estimate

viscoelastic properties of tissue. Figure 2-9 is schematic presentation of shear wave elasticity imaging approach developed by Sarvazyan et al. (1998). Fatemi and Greenleaf (1998) described an imaging technique that used acoustic emission to map the mechanical response of an object to local cyclic radiation force produced by interfering ultrasound beams. They used two coaxial, confocal transducer elements of a spherically focused annular array (consisting of a central disc and an outer annulus) driven by two continuous wave (CW) signals at slightly different frequencies ω_1 and ω_2. The object is vibrated by oscillating radiation force of varying frequency. Experiments were conducted in a water tank, which provided good ultrasonic and acoustic coupling to the object and freedom of movement for the prototype scanner mechanism. Images of excised human iliac arteries (Fatemi and Greenleaf 1999) and human breast tissue (Fatemi et al. 2002) were reported.

Walker et al. (2000) presented a method of imaging viscoelastic parameters with acoustic radiation force. A series of focused ultrasonic pulses are applied to generate an acoustic force, and then the echoes returned from these pulses are processed to estimate the radiation-force-induced displacement as a function of time. This process can be repeated at a number of locations to acquire data for image formation. The images of tissue stiffness are formed by depicting the maximum displacement induced at each tissue location after a finite period of insonification. For simple elastic materials, the displacements measured by these techniques are inversely proportional to their elastic moduli, with some distortion due to local boundary conditions.

Acoustic radiation force generates localized displacements in the medium when an acoustic wave propagates through visco-elastic or elastic media. The tissue displacements are inversely proportional to the stiffness of the tissue, and thus a stiffer region of tissue exhibits smaller displacement than a more compliant region. Since the radiation force is applied for a short time period (less than a millisecond), the acoustic radiation force impulse imaging provides information about the mechanical impulse response of the tissue, which is related to the viscoelastic characteristics of the tissue. The resolution of an acoustic radiation force impulse imaging system depends on several factors, including transducer parameters, number of pushing locations, spatial relationship of pushing locations and tracking beams, and the pulse length and kernel size used for the tracking algorithm. As with quasi-static elastography, the resolution will also be affected by the tissue itself. The resolution of the available acoustic radiation force impulse imaging systems is comparable to that achieved in conventional B-mode imaging. However, the acoustic energy required to generate detectable displacements *in vivo* is large, thus has the potential to generate an increase in tissue temperature, which may result in an increased risk to the patient.

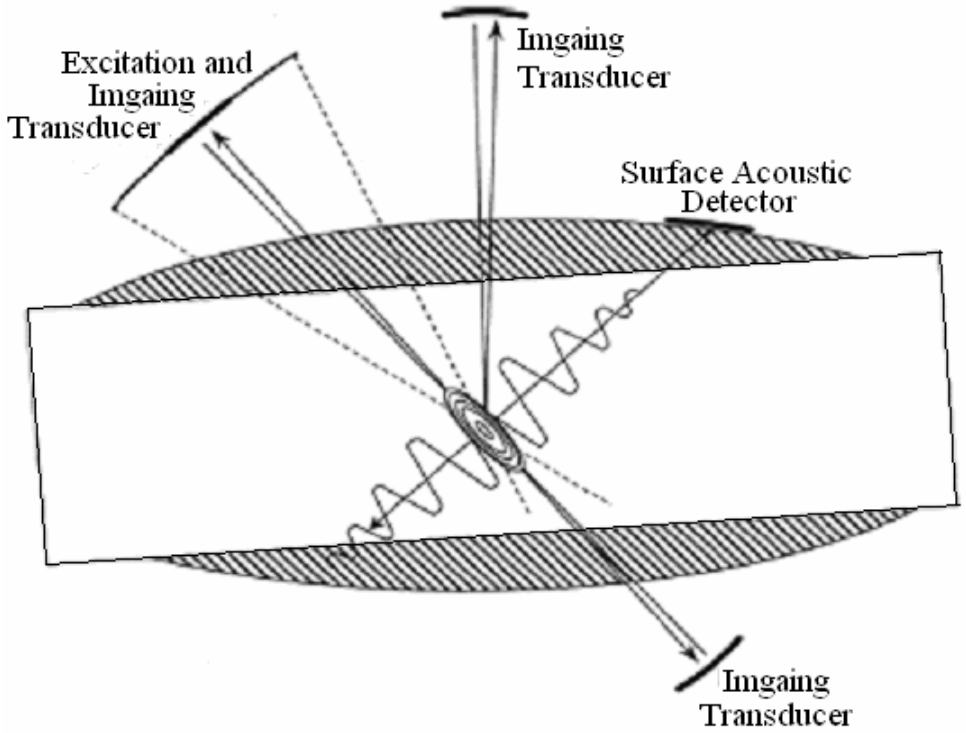

Figure 2-9. Schematic presentation of shear wave elasticity imaging. A shear wave excitation transducer as well as various imaging transducers and detection sensors are shown (Sarvazyan et al. 1998).

2.4 Ultrasound Elastomicroscopy

Previous elastography techniques have used the transducer itself or the combination of the transducer and a compressor or a vibrator (mechanical vibrator or acoustic radiation force) to stimulate the soft tissue. Ultrasound frequency typically operates in the range from 2MHz to 10MHz, which can obtain tissue axial strain image or shear modulus image at the resolution on the order of several millimeters. It's obvious that such a resolution is not sufficient for the mechanical properties imaging of the articular cartilage or thin skins with the higher demand of resolution.

High frequency ultrasound (>20 MHz) imaging, or ultrasound biomicroscopy (UBM), has been widely used to image healthy and abnormal tissue with the aim of providing information previously only available from biopsy samples. Clinical applications of UBM are mainly on ocular imaging, skin imaging, intravascular imaging, nonvascular endoluminal imaging and cartilage imaging (Foster et al. 2000). Ocular imaging using UBM has been successfully applied to detect anterior segment tumors, glaucoma, scleral disease, corneal disease, corneal pachymetric mapping, intraocular lens assessment and trauma (Palvin and Foster 1995). High-frequency ultrasound Doppler offers unique capabilities to study the flow of blood in the microcirculatory system of the eye (Palvin et al. 1998). In the skin, ultrasound biomicroscopy provides a noninvasive mean of examing cutaneous lesions with high resolution (Hoffmann et al. 1992, Passmann and Ermert 1995, Knapik et al. 1997). UBM imaging can not only provide basic measures of the thickness of the dermis but also contribute to the assessment of skin tumors by providing information about their depths and margins (Lasau et al. 1997). Intravascular imaging involves the introduction of a catheter with a rotating single element or phased-array of ultrasound transducer at its tip into the vascular for the purpose of visualising and measuring the vessel wall and any associated plaque build-up (Roelandt et al. 1993). The success of high-frequency intravascular ultrasound leads to the use of similar probes in nonvascular applications, such as urinary tract, biliary tract, endometrial canal etc (Liu and Goldberg 1995).

Ultrasound biomicroscopy provides a minimally invasive way for the assessment of cartilage since it can observe the surface structure of cartilage as well as its internal abnormalities, such as loss of matrix glycosoaminoglycans and proteoglycans, presence of abnormal cellular clustering, or changes in the subchondral bone (Sanghiv et al. 1990, Kim et al. 1995, Saied et al. 1997, Joiner et al. 2001). Cherin et al. (1998) have monitored cartilage damage in a rat model, reporting significant alterations in acoustical properties including integrated reflection coefficients and integrated backscatter, and thickness as a function of aging and damage progression. Laasanen et al. (2005) employed ultrasound biomicroscopy to quantitatively detect site-specific differences in ultrasound reflection and backscattering properties of cartilage and studied factors controlling ultrasound reflection properties of cartilage surface and cartilage-bone interface. Their results suggested that ultrasound reflection from the intact surface was mainly dependent on the cartilage surface roughness and the collagen content had less significant role. Hattori et al. (2002, 2003, 2004) analyzed the ultrasound signals reflected from cartilage using wavelet transformation to obtain the echo duration and maximum magnitude and thus to quantitative evaluate the situation of cartilage. Spriet et al. (2005) employed 40 MHz ultrasound biomicroscopy for the detection of osteoarthritis lesions of varying severity in an animal model of OA. It was validated that UBM was possible to identify slight surface irregularities of cartilage, and UBM had the potential to be a valuable tool for the in vivo identification of early lesions of OA.

High frequency ultrasound has demonstrated to be a promising tool to study articular cartilage. However, traditional ultrasound biomicroscopy only gives morphological information or acoustical properties of cartilage. It can not provide mechanical properties of cartilage which is important information for the diagnosis of osteoarthritis.

To measure or map the mechanical properties of cartilage using ultrasound, a number of systems have been reported by combining high frequency ultrasound measurement or imaging with traditional mechanical testing. The high frequency ultrasound transducer normally requires a certain water path, i.e. focal length for converging the ultrasound beam to achieve focusing. It limits the direct use of high frequency ultrasound transducer to compress the soft tissue. An additional rigid compressor or indenter between the concave-faced focused transducer and the specimen is necessary for present techniques. However, the rigid indenter was reported to attenuate the ultrasound signal significantly and generate multiple reflection signals which could overlap with the signals from the specimen (Zheng et al. 2002, 2004).

Cohn et al. (1997a, 1997b) developed a method, which used a 50MHz ultrasound transducer to study the mechanical properties of soft tissue (Figure 2-10). In their method, two plates are used to compress downwards to squeeze the soft tissue. The movement of tissue in the slit between two plates is monitored by analyzing the ultrasound echoes collected by the 50MHz ultrasound transducer, which is located above the slit. It's obvious that the slit introduces uncertainties in the mechanical boundary conditions of

test tissue. This system has been used to measure the bioengineering tissues (Cohn et al. 2000) and corneal tissues (Hollman et al. 2002). Fortin et al. (2003) reported that a 50MHz ultrasound system was developed to measure transient lateral displacements of cartilage tissues at different depth. As shown in Figure 2-11, two plates are used to compress the cartilage tissue at the axial direction thus squeezing the tissue at the lateral direction. The lateral movement of tissue is estimated using the high frequency focused ultrasound transducer. It couldn't load on a specimen uniformly and meanwhile collect high frequency ultrasound signals along the same direction.

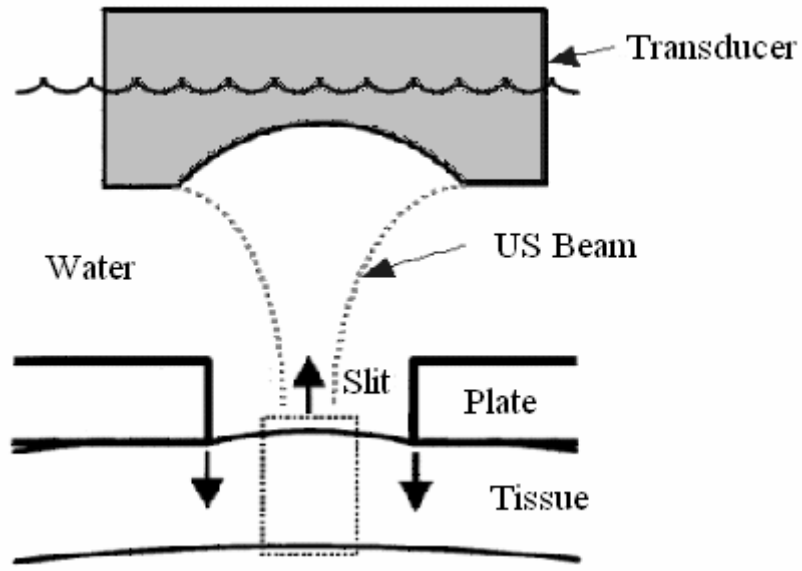

Figure 2-10. Elastomicroscopy: a high frequency ultrasound squeezing system using a 50MHz ultrasound transducer (Cohn et al. 1997a).

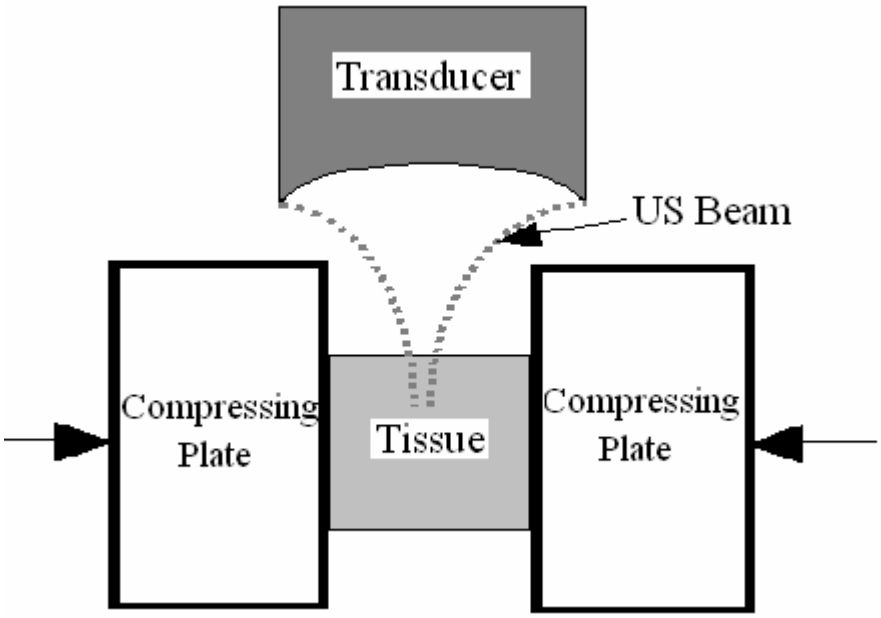

Figure 2-11. Elastomicroscopy: a 50MHz ultrasound system used to measure transient lateral displacements of cartilage at different depth (Fortin et al. 2003).

Based on the development and application of a tissue ultrasound palpation system (TUPS) (Zheng and Mak 1996), Zheng et al. (2002) worked on developing the elastomicroscopic systems for the assessment of articular cartilage. By applying signal analysis techniques to the radio frequency signals obtained by ultrasound biomicroscopy (10 to 65 MHz), they developed a 2-D ultrasound elastomicroscopy system (Figure 2-12), which consists of a compression system and a backscatter ultrasound microscope system. A 50 MHz focused transducer is used with its beam perpendicular to the specimen and compressor surface, centered between the edges of the 1 mm slit. The transducer is moved in 50 μm steps along the slit length (Zheng et al. 2004). Strain images of mouse skin and bovine patella cartilage with high resolution were reported (Zheng et al. 2002, 2004). What should be considered in this system is that, although a thin film or a thin

layer of bone of AC is used to avoid introducing uncertain boundary conditions, there are additional attenuations because of the thin film and the layer of bone.

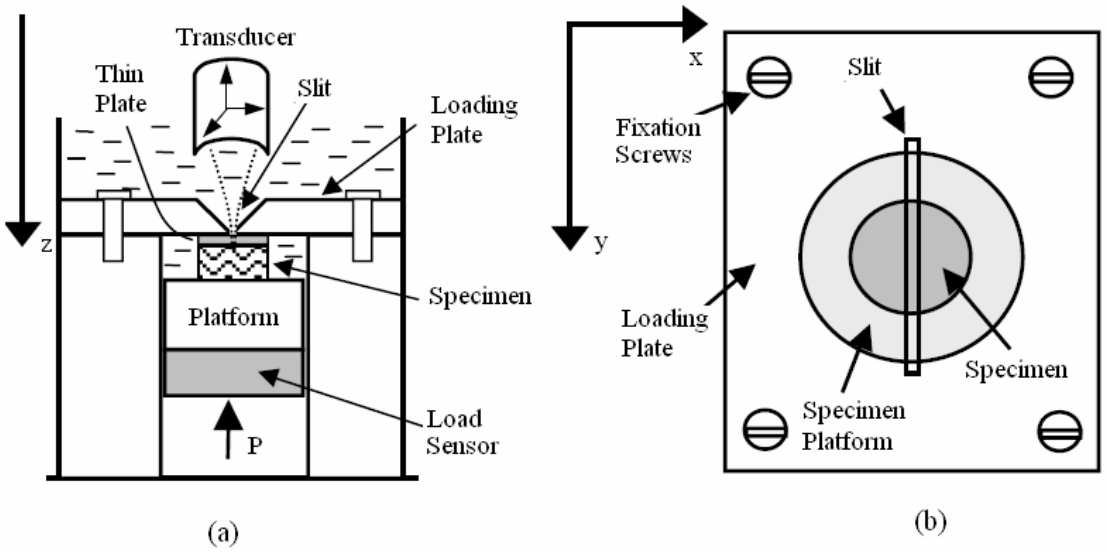

Figure 2-12. Elastomicroscopy: (a) A cross-sectional view of the compression system used for the ultrasound elastomicroscopy. (b) Top view of the compressor with the slit specimen, loading plate and specimen platform being highlighted (not to scale) (Zheng et al. 2004).

2.5 Summary

Articular cartilage has unique material properties that enable the cartilage to perform its physiological functions over lifetime and under a wide range of loading conditions. Numerous studies have investigated the relationship between the mechanical properties of cartilage and its composition/structure. Theoretical models of the mechanical behavior of cartilage have been developed. In early analytical models of cartilage deformation, articular cartilage was modeled as a linearly elastic, homogeneous, and isotropic material

in a single phase model. In this model, cartilage properties can be described by a single value for the elastic modulus, if a specific Poisson's ratio is assumed. The main disadvantage of the single-phased model is that it cannot distinguish the stress carried by the solid phase from that carried by the fluid. Biphasic model which describes articular cartilage as a solid phase (collagen – PG matrix) and a fluid phase (interstitial fluid) was then developed. Both phases are assumed to be incompressible and immiscible. The solid matrix is assumed to be porous, homogeneous, isotropic, permeable, and linear elastic. The fluid phase is assumed to be nonviscous. Numerical algorithms were developed to solve the three *in situ* coefficients intrinsic material properties of articular cartilage. However, it is impractical when the whole joint surface is to be surveyed due to the large time scales involved. Further study for modeling the indentation on articular cartilage is needed with consideration of the anisotropic, inhomogeneous, and strain-dependent permeability of articular cartilage.

Indentation is a widely used technique to measure the mechanical properties of articular cartilage. To perform the indentation on articular cartilage, a number of mechanical, arthroscopic and ultrasound indentation instruments have been developed. Mechanical indentation instruments provide an accurate and repeatable indentation measurement, though they are not convenient for clinical use; arthroscopic indentation apparatus can perform experiments *in vivo*, however, it can't measure the tissue thickness, thus failing to provide the indentation modulus of cartilage; ultrasound indentation instruments are a combination of an arthroscopy and an ultrasound transducer. By using ultrasound echoes

to estimate the tissue thickness, it can measure the instantaneous Young's modulus of articular cartilage *in vivo*, though its accuracy and repeatability are still to be further validated. In addition, it is not common to use current contact indentation techniques to image the distribution of elastic modulus for a region of tissue due to the restrictions of their low spatial resolution (typically greater than 2 mm) and long measurement time, as the measurement needs to be taken point by point. With the use of new technology, such as nanoindentation, it could be feasible to image the modulus of a small region of a thin layer of the soft tissue which is likely to be homogeneous in the entire thickness at high spatial resolution. However, the technique has not been widely used for the assessment of soft tissues as the testing results are highly dependent on the surface condition of the specimen.

Ultrasound elastography, on the other hand, can provide a local strain image inside soft tissues along the transducer axis by comparing the ultrasound cross-section images before and after compression. The local strain image with good resolution and contrast is useful for medical diagnosis. However, tissue strain is not a fundamental tissue property as it depends on the tissue mechanical properties and other factors, such as the tissue geometry, tissue connectivity, modulus contrast and distribution, applied strain and boundary conditions. Shear modulus images of soft tissues are obtained when the tissue is vibrated either by a low-frequency shear wave produced by an external vibrator or by the acoustic radiation force produced by focused ultrasound. The spatial resolution of the elasticity images using medical ultrasound frequency is usually on the order of several

millimeters and may not be sufficient for the assessment of tissues with fine structures, such as articular cartilage. Ultrasound biomicroscopy has demonstrated its ability to map cartilage with resolution in the order of 50 μm and to provide the acoustical properties of cartilage. Elastomicroscopy integrates high frequency ultrasound transducer into elastography system thus it can map the tissue strain in a high resolution. However, there still remain challenges because of the following difficulties in developing elastomicroscopy systems: 1) Increased signal attenuation for high frequency ultrasound; 2) Lack of high-frequency multiple element array transducers; 3) Lack of proper loading methods on small tissue specimens.

Besides nanoindentation and ultrasound elastomicroscopy, magnetic resonance imaging (MRI) is one of the most promising methods to detect changes in cartilage structure and composition (Burstein et al. 2000, Nieminen et al. 2000, 2001a). Although the high-filed MRI has been shown to predict cartilage stiffness *in vitro*, it does not provide direct high resolution quantitative information on the functional properties of cartilage (Nieminen et al. 2001b). Resolution of low-field (<2T) clinical MRI devices is, at its best, hundreds of micrometers invalidating, e.g. the detection of surface fibrillation or decrease of superficial proteoglycan content. Optical coherent tomography (OCT) elastomicroscopy (Huang et al. 1991, Schmitt et al. 1999), which provides a greater resolution for imaging than any available clinical technology, is a potential and relatively low-cost technique for the evaluation of articular cartilage. However, OCT does not provide direct information of the cartilage functional properties, such as its compressive Young's modulus.

After studying all these approaches, ultrasound elastomicroscopy is considered as the most feasible approach for the mechanical assessment of soft tissues with fine structures because of its selectable penetration and resolution by selecting ultrasound frequency from a wide range, easy accessibility and relative low-cost of ultrasound biomicroscopy, and the maturity of ultrasound elastography and biomicroscopy. However, the success of ultrasound elastomicroscopy will depend on the development of proper loading methods for tissue specimen. Therefore, we find it is very necessary to develop a new method to achieve noncontact ultrasound indentation and hence we can perform proper loading on small specimen, conduct fast scanning on different tissue surface as well as use high frequency ultrasound transducer to measure the mechanical properties and acoustical properties of tissues with high resolutions.

CHAPTER III METHODOLOGY

The descriptions of methodology of this study are divided into four main sections. In the first section, the development of the ultrasound water jet indentation system is introduced. The composition and calibration of the system, validation methods for the system, and the efforts in modeling the interaction between the water jet and soft tissues are then described. In the second section, the methods for obtaining modulus images of phantoms with varied modulus distribution using the water jet ultrasound indentation system are described. In the third section, one of the most important applications of the water jet ultrasound indentation system used to assess the degeneration of articular cartilage, is addressed. The methods of sample preparation for the simulation of cartilage degeneration, the fixation of the sample for experiments, and the measurement of stiffness and thickness using both water jet ultrasound indentation and mechanical indentation are detailed in this section. In the last section, the methods of the water jet ultrasound indentation system used to evaluate the bone-tendon junction tissue regeneration are described. The animal model and the methods for obtaining the stiffness and thickness of different tissue parts including patella, junction and tendon are presented.

3.1 System Development and Validation

3.1.1 Development of Ultrasound Water Jet Indentation System

3.1.1.1 System Description

A noncontact ultrasound indentation system was constructed (Figure 3-1) using a water jet as an indenter. As shown in Figure 3-1, a bubbler (B120, GE Panametrics, Inc. West Chester, Ohio, USA) was used to eject a water jet by controlling the water flow. The diameter of the water-ejecting nozzle was 1.94 mm. A 20 MHz focused ultrasound transducer (Model V316B, GE Panametrics, Inc. West Chester, Ohio, USA) was fixed with the bubbler, i.e. the water ejector, and the focused ultrasound beam could propagate through the bubbler when it was full of water as coupling medium. The focal length of the transducer was 19.05 mm, and the diameter of the active element of this transducer was 3.175 mm. Therefore, the f-number (focal length/crystal diameter) was 6. If sufficient pressure was available, a water jet could provide noncontact coupling of the transducer to a test object over a distance of 120 mm or more. Water jet coupling had an advantage over immersion when testing large structures (no large volume of water or tank was required). Coupling was maintained by pressurizing a water column and draining the water after it struck the test object. The transducer and the bubbler were installed to a three dimensional translating device (Parker Hannifin Corporation, Irvine, CA, USA) which was used to adjust the distance from the nozzle to the specimen surface to fit the focal length of the transducer and later was used to perform one-dimensional (B-scan) or two-dimensional scanning (C-scan) over the tissue. Hence, not only the local

stiffness, but also the distribution of the stiffness of soft tissues could be obtained using this water jet ultrasound indentation system.

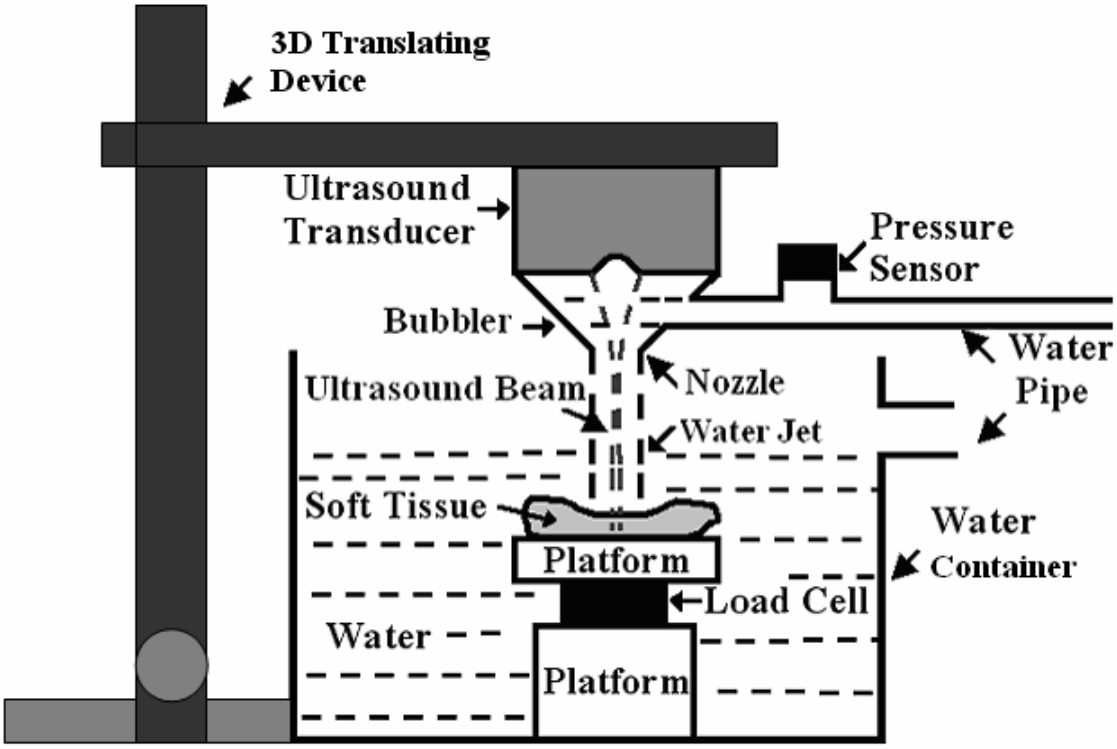

Figure 3-1. Diagram of the non-contact ultrasound indentation system using water jet compression. The water jet is used as an indenter and focused high-frequency ultrasound is employed to monitor the deformation of the soft tissue. The dimensions of the important components are: nozzle diameter 1.94 mm, water supply pipe diameter 3 mm, platform diameter 24 mm, load cell diameter 12.7 mm, ultrasound transducer active element diameter 3.175 mm, and the distance from the nozzle to tissue approximately 5 mm.

During the test, specimens were placed on a rigid platform within a water container. An outlet on the side of the container was used to control the water level within the container. For *in vivo* test on soft tissues, the water container was not a must. The ultrasound water jet indentation can be performed with the water jet only, which provides a load onto the sample and also the coupling medium for ultrasound beam to reach the sample. Therefore, a hand-held probe with an ultrasound transducer and water ejecting mechanism could be designed to perform ultrasound water jet indentation for the body tissues at different parts, without the need of a water tank. The reason for using a water container in the early phantom study was that it was found the water spattered through the air during the water jet indentation might potentially damage nearby ultrasound and translating devices. This problem was later solved by giving more distance between the devices and the water ejecting setup as well as covering the water spattering area with a plastic film.

A pressure sensor (EPB-C12, Entran Devices, Inc., Fairfield, NJ, USA) was installed near the outlet of the water pipe to measure the water pressure within the water pipe. A load cell (ELFS-T3M, Entran Devices, Inc., Fairfield, NJ, USA) located under the platform could sense the overall force applied on the specimen. The overall diameter of the load cell was 12.7 mm and the diameter of its force sensing area was 5 mm. Both the pressure sensor and the load cell were calibrated. This specific design was used to study the relationship between the pressure within the water pipe and the force applied on the

platform, which would later be used to obtain the pressure applied on the sample surface from the pressure measured within the water pipe.

An ultrasound pulser/receiver (Model 5052 UA, GE Panametrics, Inc. West Chester, Ohio, USA) was utilized to drive the ultrasound transducer and to amplify the received ultrasound signal. The ultrasound echoes reflected from the specimen were digitized by a high speed A/D converter with a sampling rate up to 2 GHz (Gage CS82G, Gage Applied Technologies, Inc**.,** QC, Canada). The pressure and the force were collected by a data acquisition card (DAQ 6024E, National Instruments Corp. Austin, Texas, USA). Figure 3-2 shows the system diagram. A program has been developed in Microsoft VC++ to control the 3D translating device and collect, process and display the ultrasound signal along with the force and the pressure in real time during the water jet indentation process. The user interface of the software is shown in Figure 3-3,where the left column is the control panel showing various parameters. In the main window, the lower right window displays the real-time radio frequency (RF) ultrasound signal reflected from the sample surface, the lower left window shows the force sensed by the load cell or pressure measured by the pressure sensor, the upper left window shows the M-mode ultrasound signals, and the upper right window is the deformation extracted from the ultrasound signal using a cross-correlation tracking algorithm (Zheng et al. 2004).

The acquisition of the A-mode ultrasound signal, force and pressure data was synchronized by the program. All the data could be recorded in a file for further off-line

analysis. The ultrasound echoes reflected from both the surface and bottom of the specimen under different loading conditions were tracked using a cross-correlation algorithm (Zheng et al. 2004). The deflection of the time of flight of the echoes was thus obtained. The original tissue thickness and the subsequent change of thickness, i.e., the deformation of the tissue under indentation, were derived from the time information. With the high-speed A/D converter, when the sampling frequency of 500 MHz was selected, the sensitivity of the time measurement was 2 ns. The theoretical sensitivity of the deformation determined by the water indentation system was better than 4 μm (Zheng et al. 2004). By using the 24-bit A/D converter to digitize the force and pressure signals, the sensitivity of force was better than 1 μN within the 10 N range and the sensitivity of pressure was better than 0.05 Pa within the 350 kPa range.

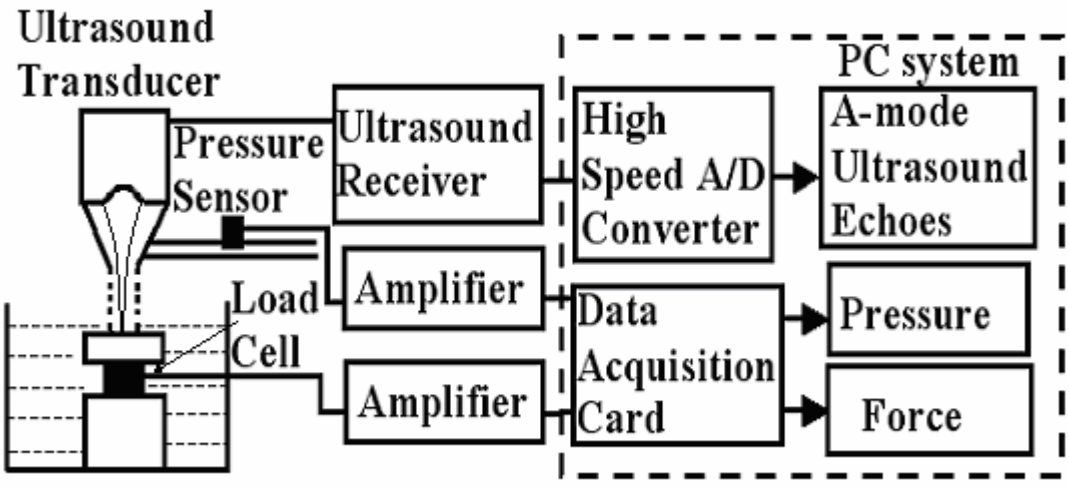

Figure 3-2. The water indentation and data collection modulus of the non-contact ultrasound water indentation system.

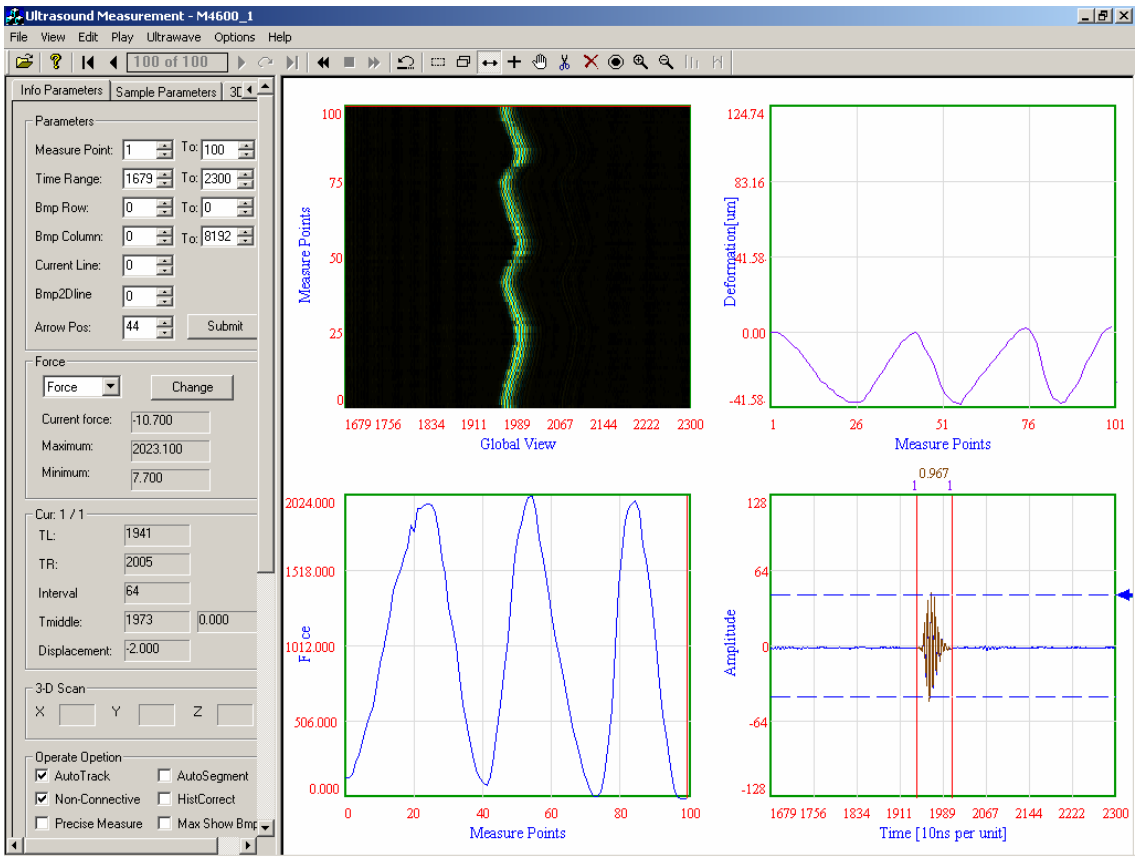

Figure 3-3. The user interface of the signal processing software. The left column is the control panel showing various parameters. In the main window, the lower right window displays the real-time ultrasound signal reflected from the sample surface, the lower left windows shows the force sensed by the load cell or pressure measured by the pressure sensor, the upper left window shows the M-mode ultrasound signals, and the upper right window is the deformation extracted from the ultrasound signal using the cross-correlation tracking algorithm.

3.1.1.2 System Calibration

Both the pressure sensor and the load cell were calibrated. The pressure sensor was used to measure and monitor the water pressure within the water pipe P_{wp}. It was calibrated using a blood pressure meter with a range of 45 kPa and at a sensitivity of 0.13 kPa

(Figure 3-4). The effect of the water temperature on the performance of the pressure sensor was also considered. Experimental results showed that the output of the pressure sensor was sensitive to the temperature. When the temperature was close to the air temperature, the output was relatively steady. During all the following experiments, daily tap water was used so the effect of water temperature was neglected.

The load cell could sense the overall force applied on the platform F_{ov} that is directly related to the force applied on the surface of the specimen F_{ss} by the water jet. Its special attributes ensured it worked properly in water. It was calibrated using an electronic balance with a range of 10 N and at a sensitivity of 0.1 mN. It had been tested that its output would change little when the temperature of water changed, however, this shift could be eliminated by keeping the water temperature as a constant or a calibration of the effect on the output of the load cell.

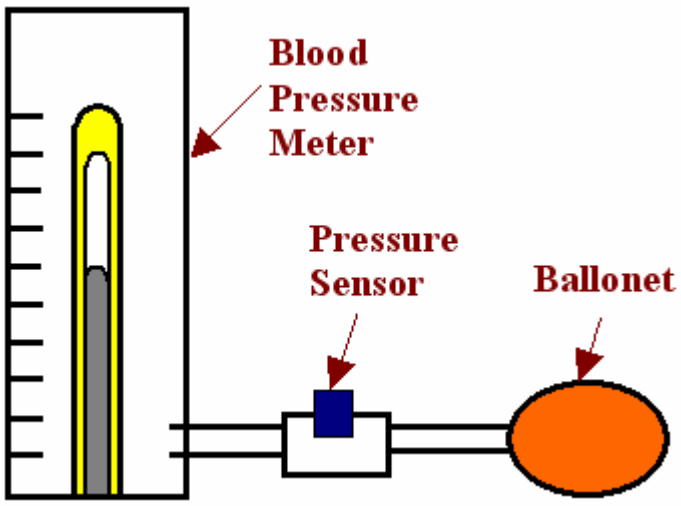

Figure 3-4. Schematic diagram of the calibration for the pressure sensor.

Both the pressure P_{wp} and the force F_{ov} were used to derive the pressure applied on the surface of the specimen P_{ss} by the water jet. The relationship between the overall force applied on the platform and the pressure within the water pipe was studied when the distance from the nozzle to the surface of the platform was fixed at approximately 5 mm according to the focal length of the focused ultrasound transducer. During this calibration experiment, there was no sample placed on the platform, i.e., the water beam was ejected to directly strike on the platform. A linear regression was used to study their relationship.

3.1.2 System Validation

The water jet ultrasound indentation system was developed for the measurement of both the thickness and the stiffness (or mechanical properties, such as Young's modulus) of the soft tissues. However, it has been known that biological tissues have very complicated mechanical properties. The stress-strain relationship for most tissue is nonlinear. Although many models of tissue have been proposed relating to stress and strain, based on linear theory of viscoelasticity, such as Voigt (Buchtal et al. 1951), Maxwell (Viidik 1966), and Kelvin (Fung 1993), it still remained a challenge for using such a novel indentation system to conduct experiments on biological tissues. Therefore, before the system was used to assess the soft tissues such as articular cartilage, tissue-mimicking phantoms were prepared for the validation test. The phantoms were first assessed by the ultrasound water indentation system, and then their compressive Young's moduli and Poisson's ratios were determined by a compression device developed by our group. The results obtained from these two systems were compared.

3.1.2.1 Preparation of Uniform Phantoms

It has been reported that tissue-mimicking phantoms made from silicones or gels have similar mechanical properties with soft tissues and their shapes, sizes and compositions are easier to control (Hall et al. 1997). For the validation tests, Rhodia RTV 573 (Rhodia Inc. CN7500, Cranbury, NJ, USA) and Wacker M4648 and M4600 silicones (Wacker Chemicals Hong Kong Ltd. HK, China) were used to make phantoms with different stiffness and height (Figure 3-5). Each of the uniform phantoms was made from one kind of silicone and was supposed to be homogeneous. The sizes of the uniform phantoms were 1 *cm* × 1 *cm* × 0.5 *cm* (width×length×height), 1 *cm* × 1 *cm* × 1 *cm*, and 1 *cm* × 1 *cm* × 1.5 *cm* respectively.

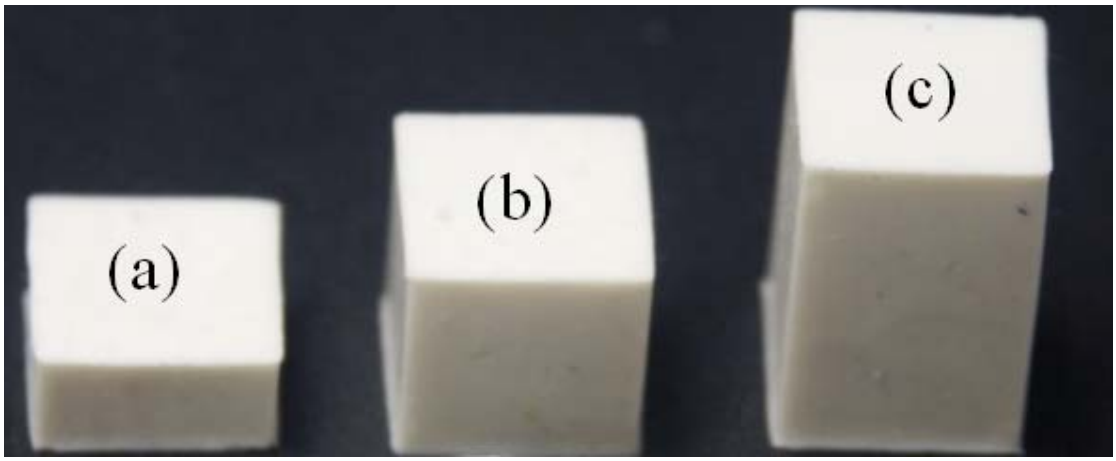

Figure 3-5. Phantoms made from three kinds of silicones (Rhodia RTV 573, Wacker M4648 and M4600) were prepared for the experiments: the uniform phantoms with dimensions (a) 1 *cm* × 1 *cm* × 0.5 *cm* (width×length×height), (b) 1 *cm* × 1 *cm* × 1 *cm*, and (c) 1 *cm* × 1 *cm* × 1.5 *cm.*

3.1.2.2 Ultrasound Water Jet Indentation on Uniform Phantoms

Water jet ultrasound indentation tests were performed on the uniform phantoms. The pressure/deformation curves were obtained to calculate the stiffness ratios of those phantoms. The stiffness ratio was defined as the ratio of the applied pressure on the phantom surface P_{ss} to the relative deformation (deformation/thickness) with a unit of kPa. P_{ss} was calculated using the overall force applied on the phantom divided by the cross-section area of the water jet at the contact interface with the assumption that the contact area between the water jet and the sample keeps as a constant. As Galbraith and Bryant (1989) reported, the results of the indentation analysis were unaffected if the lateral dimension of the tissue was three or more times larger than the diameter of the indenter. In this validation study, the lateral dimension of the prepared uniform phantoms ($1\ cm \times 1\ cm$) was more than five times of the diameter of the water jet indenter and the indentation was generally performed on the center of the phantom surface. During the test, the phantom was placed at the center of the platform and was gently fixed at edges by four screws. The phantom was not squeezed from the lateral sides; furthermore, it was found that it could “stick” to the platform since the surfaces of both phantom and the platform were quite flat and smooth. This boundary condition fulfilled the Hayes’ model. The position of the ultrasound transducer to the phantom surface was adjusted according to the height of the phantom so as to keep a constant initial distance between the transducer and the phantom surface. The focal point of the transducer was placed approximately at the surface level of the phantom. The distance between the nozzle and the surface of the specimen was 5 mm. The container was full of water before loading

and a constant water level was kept during the test. In each loading and unloading cycle, the water pressure within the water pipe was changed at a rate of approximately 45 kPa/s and from 0 to 180 kPa, which corresponds to the local deformation from 0 to approximately 0.4 mm for the softest phantom that we used. This process was repeated for 3 cycles in each test. Each phantom was indented three times. A total of 27 pieces of uniform phantoms was tested.

3.1.2.3 Uniaxial Compression Test on the Uniform Phantoms

To compare with the experimental results obtained from the ultrasound water jet indentation, the compressive properties of the phantoms were measured using a mechanical testing device which was developed by our group. As shown in Figure 3-6, the axial displacement was monitored by a displacement transducer - linearly variable differential transformer (LVDT), and the lateral deformation of the phantom was measured by an unfocused ultrasound transducer (5MHz, Model V316B, GE Panametrics, Inc. West Chester, Ohio, USA) during the axial compression. Ultrasound coupling gel was used between the ultrasound transducer and the phantom for ultrasound beam propagation. It was also used in the interface between the phantom and the compressor and that between the phantom and the platform, serving as lubrication to fulfil a frictionless boundary condition. The phantom was placed at the center of the platform and kept perpendicular to the ultrasound transducer by moving the phantom to obtain a maximal ultrasound echo reflected from the two opposite surfaces of the phantom. The ultrasound echoes were tracked using the cross-correlation algorithm to

estimate the lateral deformation of the phantom during compression (Figure 3-7). The uniaxial force applied on the phantom was measured by a load cell (ELFS-T3M, Entran Devices, Inc., Fairfield, NJ, USA, calibrated for a range of 10N). The axial displacement, force and ultrasound echoes were recorded synchronously by the program. The compressive Young's moduli and Poisson's ratios of the phantoms could be thus obtained.

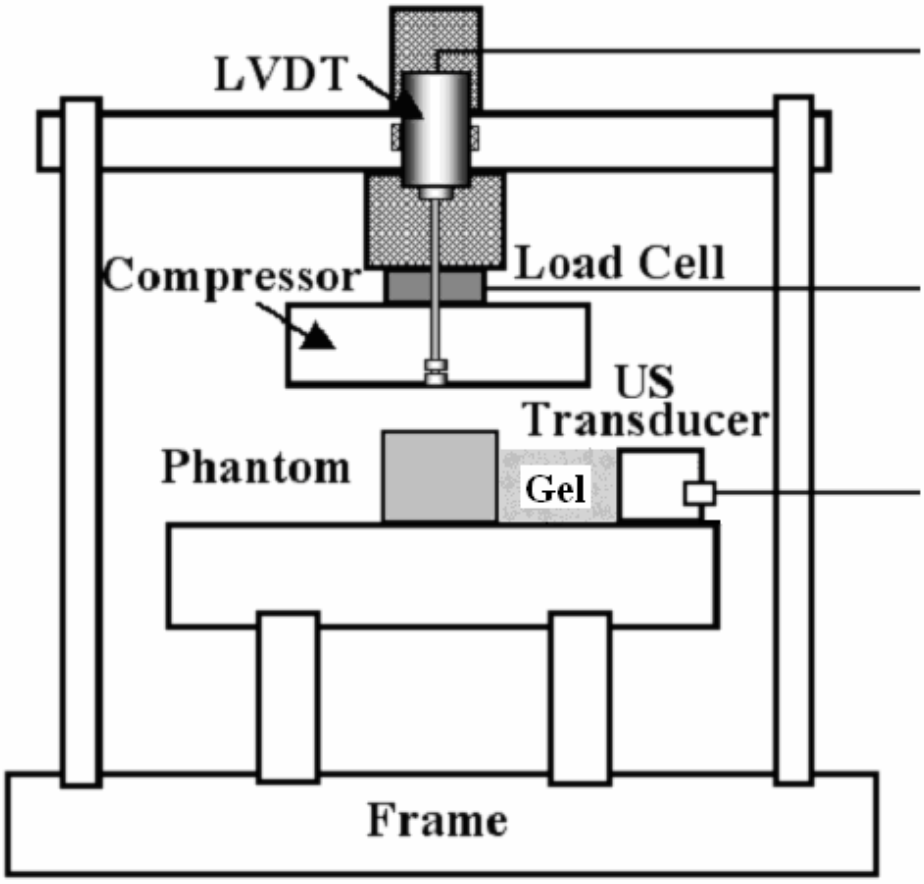

Figure 3-6. Diagram of the system which was used to measure the compressive Young's moduli and Poisson's ratios of the phantoms. A load cell was used to measure the uniaxial force applied on the phantom. An ultrasound transducer was used to estimate the lateral deformation of the phantom, while the LVDT was employed to measure the axial deformation.

The compressive Young's modulus of the phantom was calculated using Equation 3-1:

$$E_c = \frac{F/A}{\Delta L/L_0} \tag{3-1}$$

where E_c is the compressive Young's modulus of the phantom, F the axial force applied on the phantom, A the surface area of the phantom, ΔL the axial deformation, and L_0 is the initial height of the phantom. The Poisson's ratio calculation was based on the lateral deformation estimated from the ultrasound echoes and the axial deformation measured by LVDT (Equation 3-2):

$$\upsilon = \frac{\Delta W/W_0}{\Delta L/L_0} = \frac{|W_1 - W_0|/W_0}{|L_1 - L_0|/L_0} \tag{3-2}$$

where: $W_0 = \frac{1}{2} t_1 \cdot c_{phantom}$, $W_1 = \frac{1}{2} t_2 \cdot c_{phantom}$, $\Delta W = W_1 - W_0 = \frac{1}{2}(t_2 - t_1) \cdot c_{phantom}$, where υ is the Poisson's ratio of the phantom, ΔW the lateral deformation, ΔL the axial deformation, W_0 and L_0 the initial width and height of the phantom, t_1 and t_2 the time of flight of ultrasound between the two lateral faces of the phantom before and after compression, respectively, and $c_{phantom}$ the speed of sound in phantom. The meanings of these variables are shown in Figure 3-8.

The test for each phantom included loading and unloading phases. The test was repeated for three times on each phantom. The compression rate was kept at approximately 45 μm/s and the total deformation was up to 10%. Only the data with deformation less than

3% were used to calculate the Poisson's ratio and Young's modulus, corresponding to the 3% local strain of the phantoms under ultrasound water indentation. According to the stress/strain curves of the phantoms obtained from compression, they were in the linear elastic region for the 3% deformation.

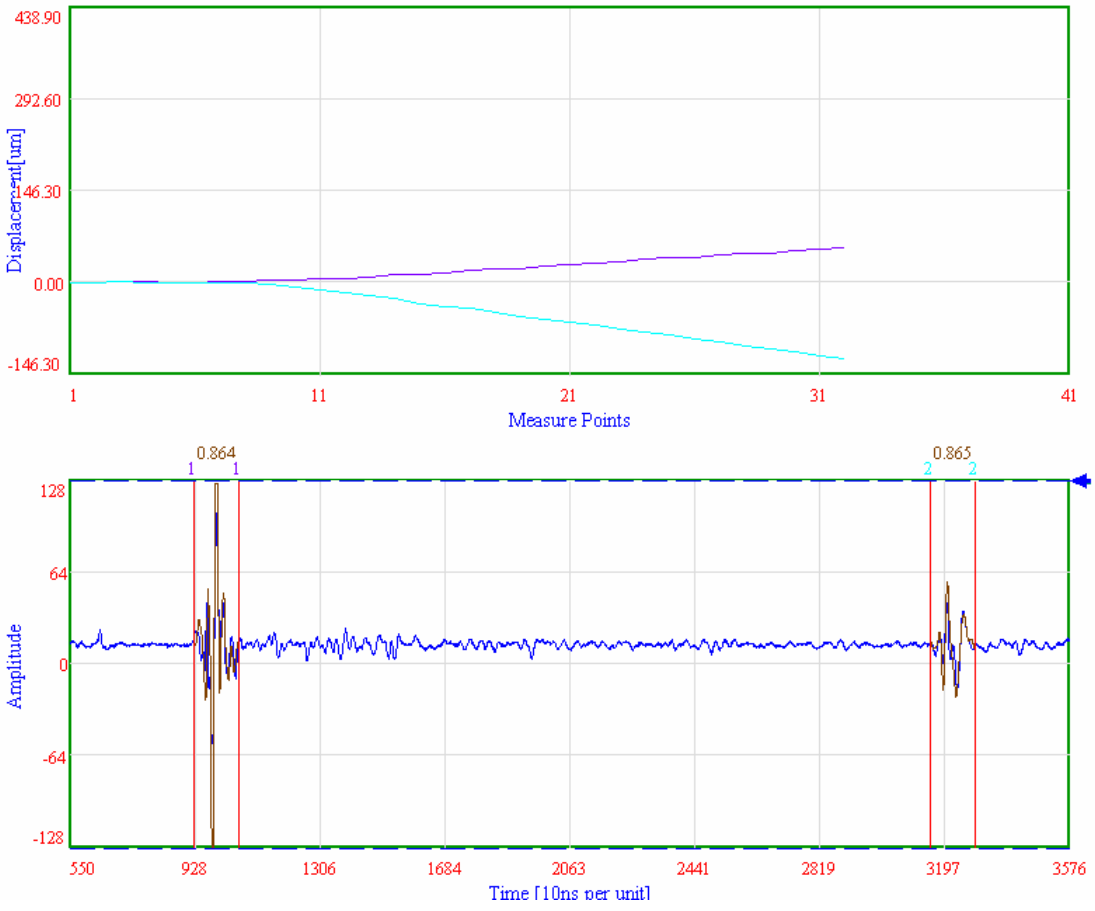

Figure 3-7. Estimation of the lateral deformation of the phantom under uniaxial compression. The lower window shows the ultrasound echo pulses reflected from the two opposite surfaces of the phantom, and the upper window shows the movements of these two echoes obtained from cross-correlation tracking.

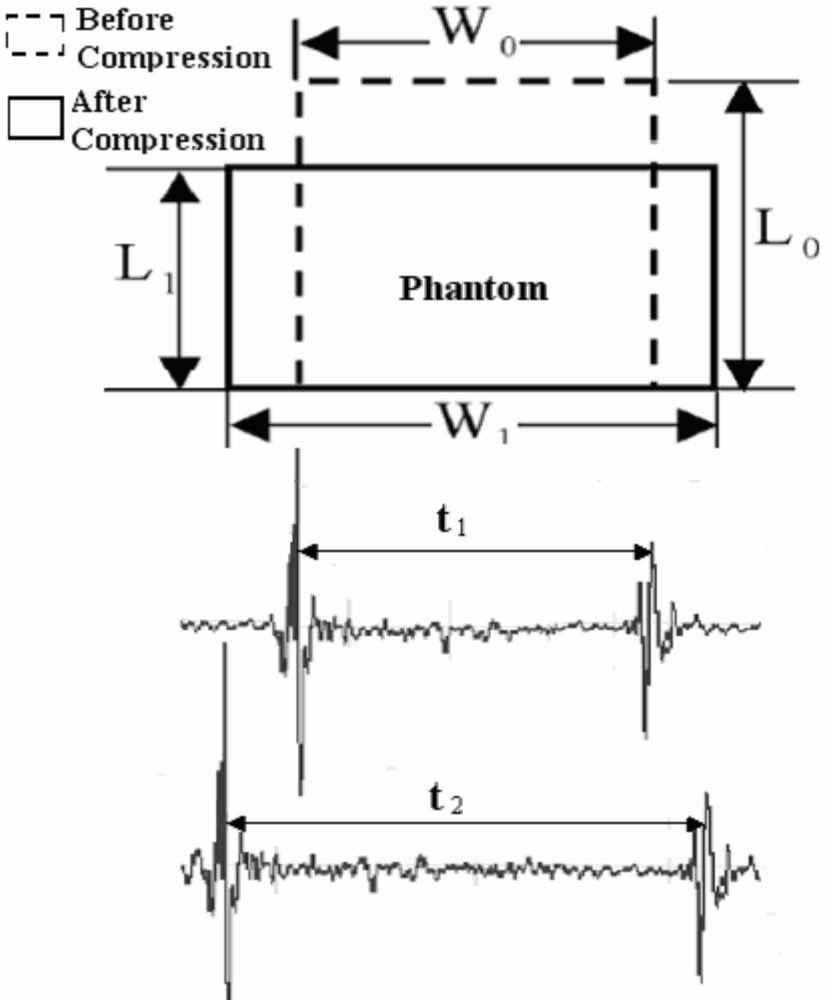

Figure 3-8. Schematic diagram for the estimation of the Poisson's ratio of the uniform phantom: t_1 and t_2 are the times of flight of ultrasound from the two parallel surfaces of the phantom before and after compression, respectively.

3.1.3 Modeling of the Interaction between Water Jet and Soft Tissue

The interaction between the water beam and tissue or phantom surface during the compression is very complicated. It is expected that the deformation profile as well as the pressure distribution along the interaction interface keeps changing as the increase of the water jet pressure. Moreover, the pressure distribution may also vary across the water

beam. Although the relationship between the water pressure within water pipe and the overall force applied on the platform has been preliminarily studied, the measurement or calculation of the pressure applied on the tissue surface in the contact area remains a difficulty.

According to the basic Bernoulli's equation and the control volume formulation in fluid dynamics (Stanley 1998), the relationship between the pressure within the water pipe P_{wp} (Point 1, as shown in Figure 3-9) and that at the water jet head P_{wh} (Point 2, as shown in Figure 3-9) can be described as follows:

$$\frac{P_{wp}}{\rho} + \frac{v_1^2}{2} + gz_1 = \frac{P_{wh}}{\rho} + \frac{v_2^2}{2} + gz_2 \quad (3\text{-}3)$$

$$v_1 A_1 = v_2 A_2 = Q \quad (3\text{-}4)$$

$$z_1 - z_2 = h_{ph} \quad (3\text{-}5)$$

where v_1 and v_2 are the flow rates, A_1 and A_2 are the cross-section areas of the water flow, z_1 and z_2 are the relative heights at point 1 and point 2 respectively. ρ is the density of water and g is gravity. Q is the quantity of the flow. As described in the section 3.1.1.1, variables P_{wp}, A_1, A_2 and h_{ph} could be measured at the current settings. The flow rate v_2 at the water jet head was measured by a measuring cylinder with a resolution at 0.1 mL. The flow rate at point 1 v_1 could be calculated from Equation 3-4; therefore, P_{wh} could be obtained using Equation 3-6:

$$P_{wh} = p_{wp} + \frac{\rho}{2} \cdot v_2^2 \cdot (1 - \frac{A_2^2}{A_1^2}) + \rho \cdot g \cdot h_{ph} \quad (3\text{-}6)$$

The relationship between P_{wh} and P_{ss} may depend on not only the distance from the water jet head to the sample surface, but also the material properties, the shape of the sample as well as the size of the indenter.

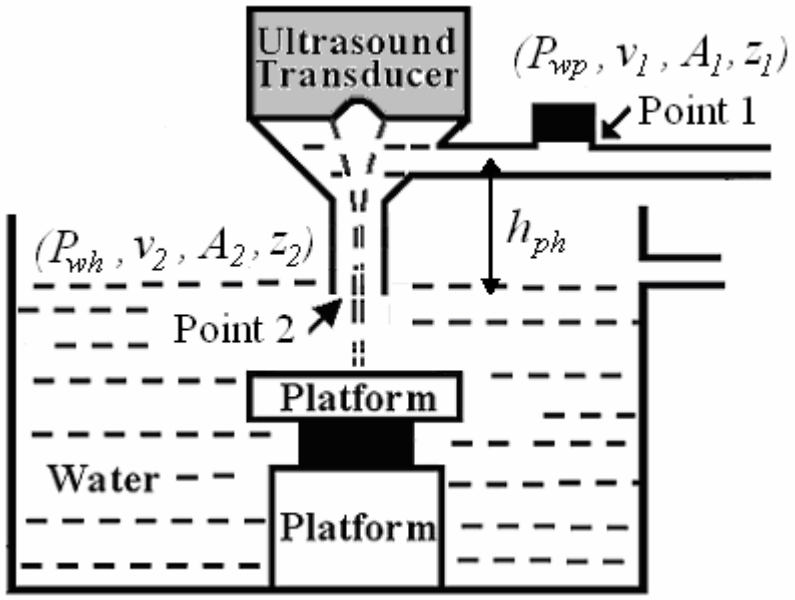

Figure 3-9. Schematic diagram of the water jet ultrasound indentation system for the calculation of pressure applied on the sample surface.

Besides the theoretical analysis, the interaction between the water jet and the sample was also studied using ultrasound B-mode scanners. As shown in Figure 3-10, the deformation profile of the phantom under water jet indentation was detected using a real-time, B-mode ultrasound scanner (SonoSite 180 PLUS, SonoSite, Inc., Bothell, WA, USA). The frequency of SonoSite ranged from 5 to 10 MHz with the axial resolution at 0.47 mm and the lateral resolution at 0.51 mm. During the indentation loading process,

the deformation profile at the center of contact interface was recorded at a frame rate of 25 Hz.

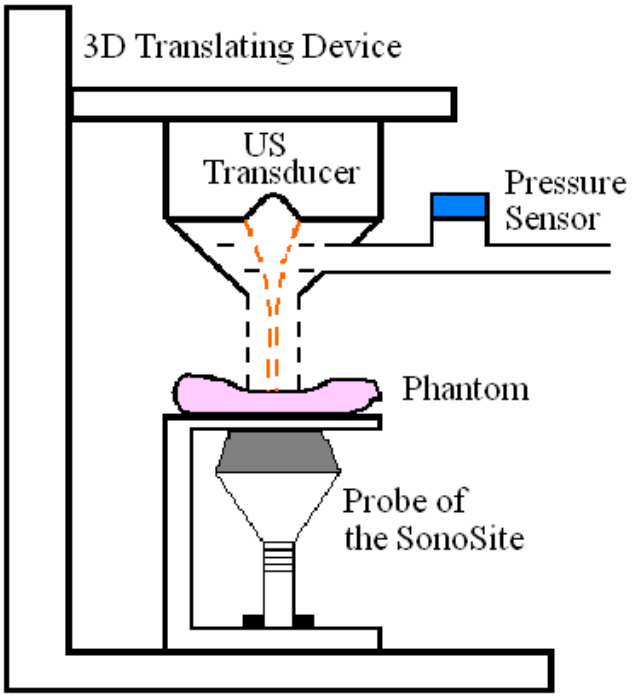

Figure 3-10. Deformation profile detection using SonoSite. The probe of the SonoSite was placed under the phantom. Its frequency ranged from 5 to 10 MHz.

3.2 Phantom Study for Modulus Imaging

Ultrasound C-scan imaging provides a useful view of an object, showing a plane perpendicular to the ultrasound beam. It has been widely used in the aerospace industry to detect the surface corrosion, delaminations, voids, cracks and other faults in aging aircraft. In this part, the new ultrasound water indentation system was used to perform C-scan imaging. By applying different water pressures for C-scan sequences, the modulus images of the phantoms could be obtained.

3.2.1 Phantom Preparation

To fabricate phantoms with varied stiffness distribution, several kinds of compositions were tried for both the inclusion and backgrounds of the phantom, such as sponge, jelly and silicone. It was reported that phantoms with cylindrical inclusion made from reinforced sponge materials and backgrounds made from gelatine-agar-water mixture were suitable for fabrication to obtain different stiffness contrast (Srinivasan et al. 2004). However, the reflected ultrasound signals were very poor when scanning over the sponge surfaces. After many pilot trials, phantoms with inclusion made from silicones and background made from gelatine-agar-water mixture were adopted for this modulus imaging test.

Six pieces of tissue-mimicking phantom with a diameter of 25 mm and a height of 5 mm were prepared for the experiments. Figure 3-11 shows a typical photo of one phantom and its B-mode image. Each phantom consisted of a stiff cylindrical inclusion with a diameter of 8 mm inside a homogeneous background. This axisymmetric cylindrical geometry was chosen as an approximation of the cross-section of a hard cancerous and noncancerous inclusion inside soft tissue (Garra et al. 1997). The stiff inclusion cylinders were made of silicones (Rhodia RTV 573, Rhodia Inc. CN7500, Cranbury, NJ, USA; Wacker M4648 and M4600, Wacker Chemicals Hong Kong Ltd. HK, China). The backgrounds were made of agar-water mixture with different concentrations of agar,

ranging from 10.0 g/L to 30.0 g/L. To produce a homogeneous background, the agar powder (Fisher Scientific Co. Fairlawn, NJ, USA) was hydrated with a solution of deionized water and *n*-propanol and heated to 70ºC to disperse the colloid, clarify the solution, and release the trapped gasses. When the mixture was cooled to 30ºC (near its congealing point), a small quantity of formaldehyde (Fisher Scientific Co. Fairlawn, NJ, USA) was added to raise the melting point of the congealing point of the congealed gel (Hall et al. 1997). A total of six phantoms labelled as CP1 to CP6 were made and used for the C-scans. Table 3-1 shows the descriptions of the gel samples used in this study.

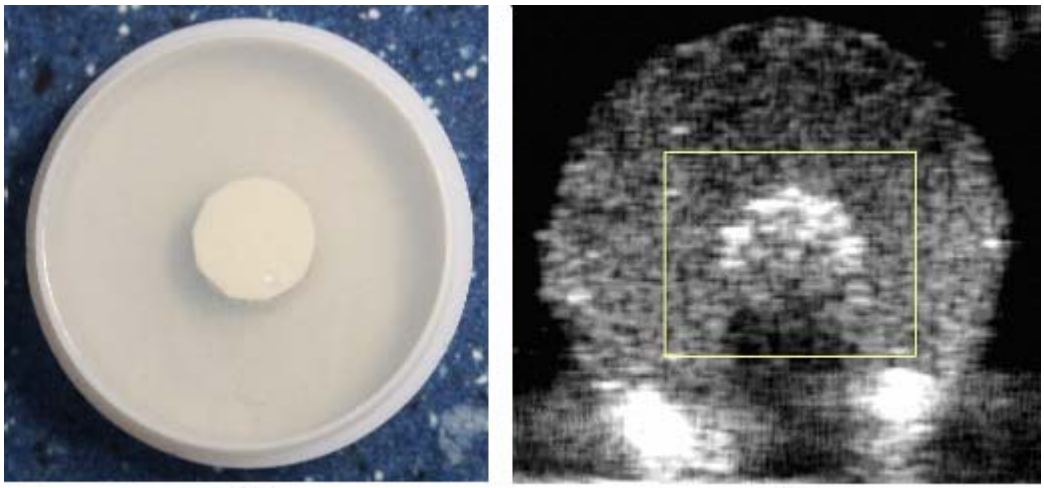

Figure 3-11. A typical phantom prepared for the C-scan experiment: (a) Photo of the phantom; (b) Ultrasound B-mode image of the phantom.

In addition, uniform cylindrical samples with the same dimension as the mixed phantoms (with a diameter of 25 mm and a height of 5 mm) but without inclusion were also prepared for each phantom material. Their Young's moduli were measured using uniaxial

compression tests by a Hounsfield standard material testing machine (H10KM, Tinius Olsen, Ltd. UK). Typically, samples were preloaded to 2% and then compressed to an additional 5%. The interfaces between the sample and the compressor and the plate were lubricated by oil to avoid frictions. All the measurements were performed at room temperature (20.5ºC ± 0.5ºC).

Table 3-1. Descriptions of the phantoms used in the study of modulus imaging:

Phantom	Background [#] (Agar weighted concentration, g/L)	Inclusion (Silicone [*])	Modulus Contrast[**] (dB)
CP1	10	RTV 573	10.02
CP2	15	RTV 573	8.78
CP3	15	M4648	7.05
CP4	20	RTV 573	4.97
CP5	20	M4600	3.38
CP6	30	M4600	0.97

[#] The background gel phantom was made of agar powder hydrated with a solution of deionized water. N-propanol and formaldehyde were added with weighted concentrations of 8.02% and 0.05‰, respectively.

[*] The silicones used for the inclusion cylinders were Rhodia RTV 573 and Wacker M4648 and M4600.

[**]The modulus contrast was defined as the ratio of the compressive Young's modulus of the inclusion to that of the background material, which was measured using the uniaxial compression test.

3.2.2 One-dimensional Scan on Phantom

One-dimensional scanning experiment was conducted on one of the phantoms (CP2) using the three-dimensional translating device. The phantom was first scanned by the ultrasound transducer at a moving rate of 1 mm/s when the pressure was kept as 0 kPa. Then it was scanned again along the same line after the pressure changed to 58 kPa. The deformation of the phantom at each site along the scanned line was obtained.

3.2.3 C-scan on Phantom

During the scan experiment, the phantom was placed on the specimen platform and slightly fixed to avoid the slip. An area of 12 mm × 12 mm was scanned along both directions with a step of 0.2 mm. The scan area was selected based on the boundary requirement of indentation that the lateral dimension of the sample should be at least three times larger than the diameter of the indenter (Galbraith and Bryant 1989). The water temperature used for the water jet indentation was approximately 20ºC. The water pressure during a single C-scan was maintained to be a constant. The scan time for each phantom was at most 20 minutes. Typically, the phantoms were preloaded with a pressure of 3 kPa to obtain the first C-scan and were then scanned with a pressure of no more than 20 kPa for the second C-scan. For each phantom, the maximal strain was controlled at 5%, within which level the phantoms could be normally modeled as linear elastic materials. The ultrasound pulsed echoes reflected from the sample surface and bottom were tracked for each corresponding measurement site for the 12 mm × 12 mm area to compose the strain image (60 × 60 pixels). The stiffness ratio of each indentation

site was calculated from the pressure applied on the phantom surface and local strain to compose the modulus image with the assumption that the Poisson's ratios of the inclusion and background material were the same. For our experiment which usually applied quick loading on phantom and the stiffness ratio was calculated from its instantaneous response, the Poisson's ratios of both inclusion and background may regarded as approximately 0.5 and meets our assumption. The strain contrast (S_c) was defined as the ratio of the average strain of the background (S_b) to that of the inclusion (S_i):

$$S_c(dB) = 10 * \log\left(\frac{S_b}{S_i}\right) \quad (3\text{-}7)$$

Correspondingly, the modulus contrast (E_c) was defined as the ratio of the average stiffness ratio of the inclusion (E_i) to that of the background (E_b):

$$E_c(dB) = 10 * \log\left(\frac{E_i}{E_b}\right) \quad (3\text{-}8)$$

In our study, the modulus contrasts of the phantoms calculated from the modulus images were correlated with those measured using the uniaxial compression tests.

To assess the reproducibility of the modulus image obtained by the ultrasound water jet indentation system, a repeatability test was conducted on phantom CP1. The phantom was scanned twice under the approximately same indentation level. Two modulus images were obtained from these two independent scan sequences. The cross-correlation was used to quantify the similarity between the corresponding modulus images. The correlation coefficient (r) was calculated by:

$$r = \frac{\sum_{i,j}(x[i,j]-\mu_x)(y[i,j]-\mu_y)}{\sqrt{\sum_{i,j}(x[i,j]-\mu_x)(x[i,j]-\mu_x)\sum_{i,j}(y[i,j]-\mu_y)(y[i,j]-\mu_y)}} \quad (3\text{-}9)$$

where x[i,j] and y[i,j] are the modulus values of the two modulus images at pixel [i,j], and μ_x and μ_y are the mean modulus values of the two images, respectively.

3.3 Assessment of Articular Cartilage Degeneration

3.3.1 Samples - Simulated Articular Cartilage Degeneration

Eight fresh mature bovine patellae without obvious lesions were obtained from the local slaughterhouse within 2 hours post mortem and stored at -20^{o}C before use. The patella articular joint was selected as it provided a flat articular cartilage surface for indentation. During specimen preparation, the patellae were first thawed in normal saline solution (0.15 M NaCl) at room temperature 20^{o}C for 1 hour, then the lateral lower part (1/4 of the patella) of each patella (Figure 3-12) was cut for the experiment by a bandsaw (Buehler, Lake Bluff, IL, USA), and the bone was cut into a flat layer with its thickness varying from 3 mm to 8 mm. During the process, the cartilage surface was kept moist with normal saline solution (0.15 M NaCl) without immersing the sample. All the samples were wrapped with bandage and wetted with normal saline, then were stored at -20^{o}C before later use.

Simulated Articular cartilage degeneration was achieved by a trypsin digestion for the cartilage (n = 8). Before digestion, the sample was first thawed in normal saline solution

(0.15 M NaCl) at room temperature 20^{o}C for 1 hour; it was then put into a container and immersed in the 0.25% trypsin solution (Gibco Invitrogen Corp., Grand Island, NY, UA) (Figure 3-13). The container was kept for 4 hours inside an incubator (MMM, Medcenter Einrichtungen GmbH, Schulstrasse, DE, Figure 3-14) at 37^{o}C for inducing degeneration of articular cartilage. Trypsin reduces the content of proteoglycans in cartilage which was thought to simulate cartilage degeneration (Andrew et al. 1993; Lyyra et al. 1999a; Qin et al. 2002). It has been well documented that in osteoarthritis there is a decrease in proteoglycans and an increase in water content (Mankin et al. 1994; Lohmander 1988). The concentration and duration of the digestion treatment were selected according to the previously developed protocols (Qin et al. 2002, Cheung 2005). All samples were washed by normal saline solution after the digestion treatment was finished.

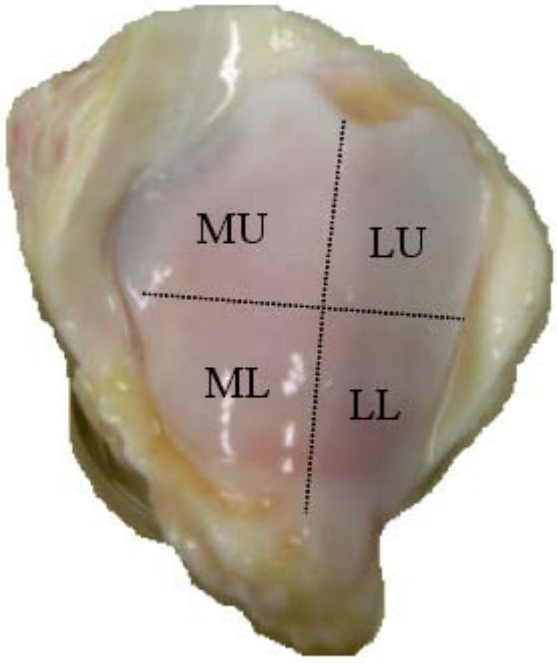

Figure 3-12. The lateral lower (LL) quarter of normal bovine patella without obvious lesions was cut as the sample for experiment.

Figure 3-13. A typical sample of articular cartilage being immersed in the 0.25% trypsin solution for digestion treatment.

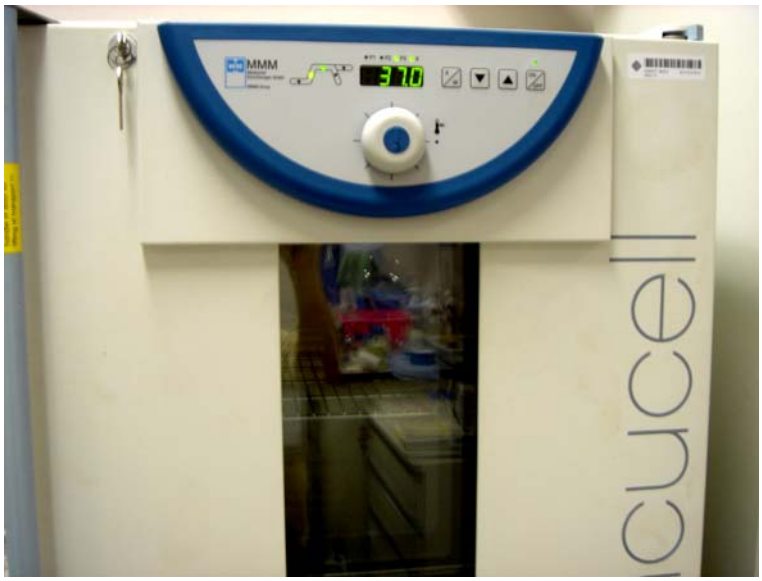

Figure 3-14. The incubator used for the digestion of cartilage. The temperature was set as 37^{o}C, and the sample was kept inside for 4 hours.

3.3.2 Stiffness and Thickness Measurement with Ultrasound Water Jet Indentation

The bovine patella samples (n = 8) before and after trypsin digestion were assessed by both the ultrasound water jet indentation and a mechanical indentation. As mentioned in the sample preparation procedure, the lateral lower quarter of the patella was cut as the sample for experiment, and the thickness of bone layer was not constant; therefore, the shape of the sample was not regular. To fix the sample rigidly and keep the articular cartilage surface flat and perpendicular to the ultrasound transducer, a fixation device (Figure 3-15) was carefully designed. During the experiment, the sample was placed on a head of a tripod (#115, Manfrotto, Italy) which provided a rigid support and meanwhile allowed for 3 degrees of freedom in orientation. This device was convenient for the experimental use since it could be easily adjusted to keep the cartilage surface perpendicular to the ultrasound transducer. Its rigidity also allowed for deforming the cartilage layer instead of pushing the whole sample down during the loading phase of the indentation. In addition, two clamps were used to fix the sample at the edges of the sample to avoid the slip of the sample during indentation.

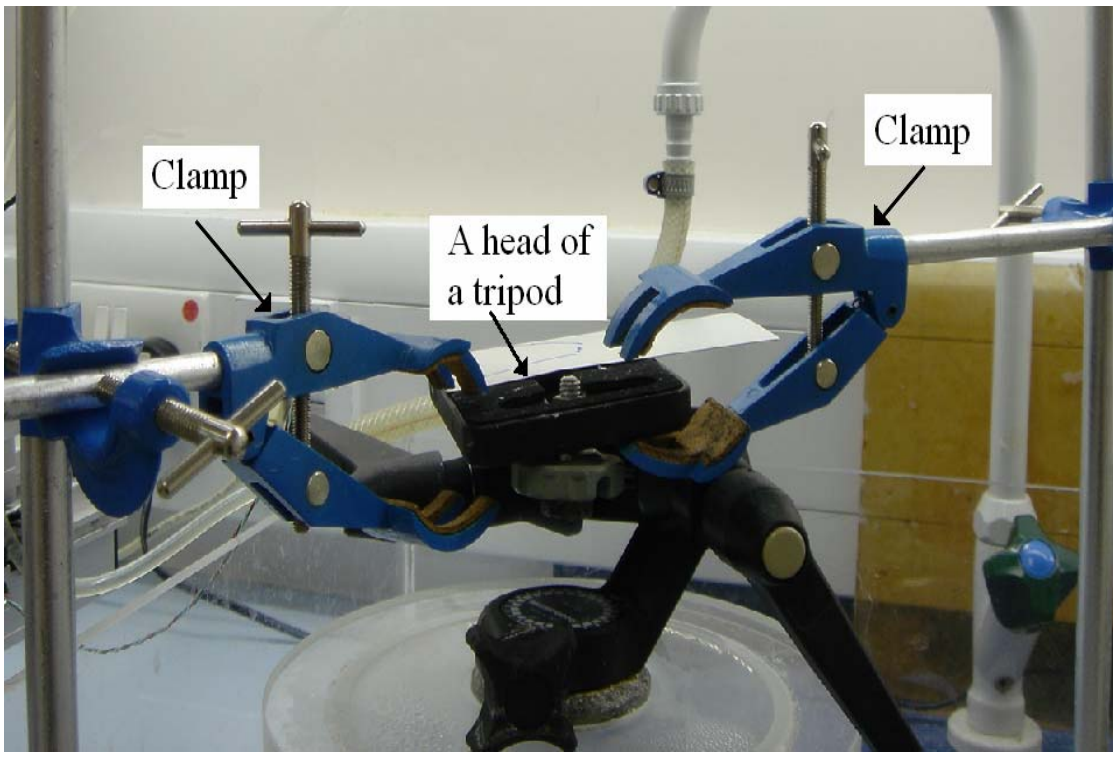

Figure 3-15. Fixation device for the experiment of assessment of articular cartilage: the head of a tripod provides a rigid support and allows for 3 degrees of freedom in orientation; the two clamps can fix the sample to avoid its slip.

The sample was first thawed in normal saline solution at room temperature 20^{o}C for 1 hour, and then it was fixed with its cartilage surface perpendicularly facing the ultrasound transducer. For each sample, three indentation sites were carefully selected through the following procedure: firstly, the sample was scanned across by the 20 MHz ultrasound, and those regions with strong echoes reflected from both the cartilage surface and the cartilage/subchondral bone interface were selected; secondly, three sites in those regions were selected with the distances between each pair of them larger than 8 mm; and finally, at each test site, fine adjustment of the orientation of the platform was made

to obtain the maximal echo amplitude. In addition, the distances from the test site to the edges of the sample were also larger than 8 mm. Such a selection criterion could fulfill the boundary condition of indentation proposed by Galbraith and Bryant (1989). The indentation sites were marked using a permanent marker pen (Lumocolor, Staedtler, Germany). Figure 3-16 shows a typical sample with three marked indentation sites.

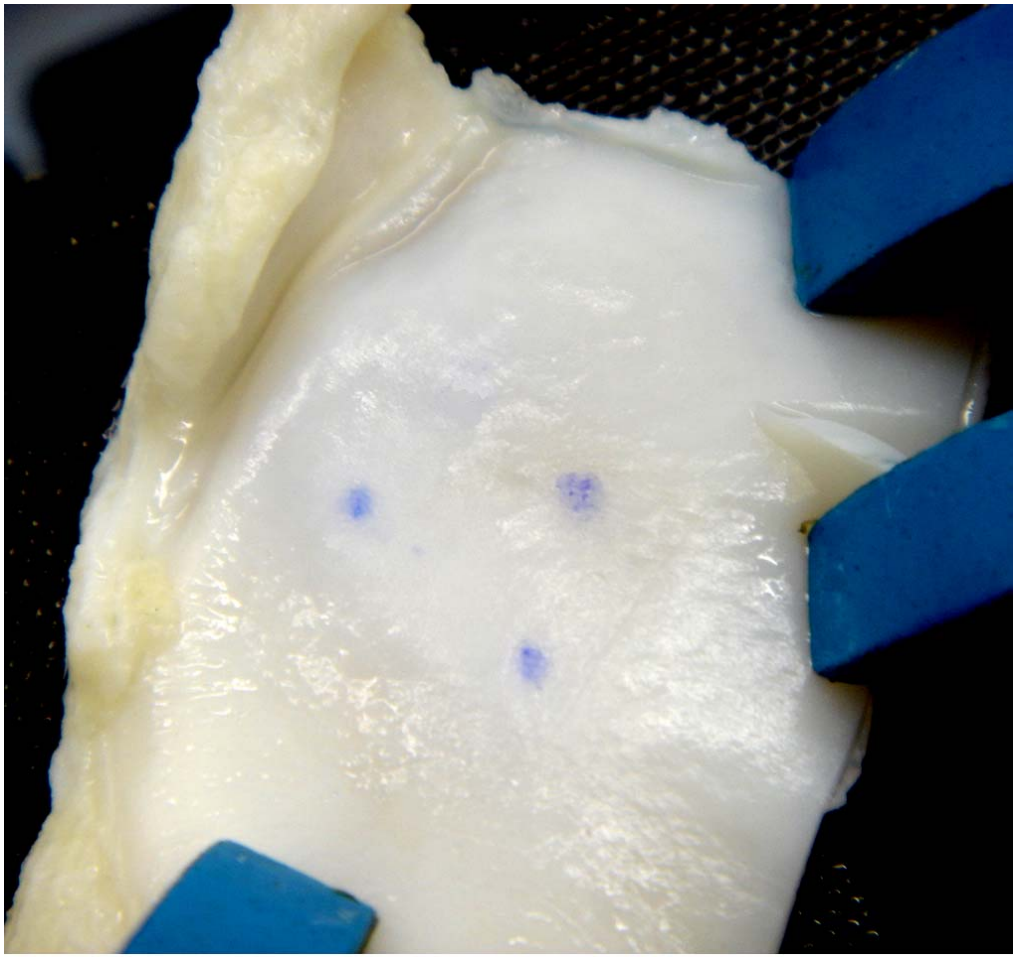

Figure 3-16. A typical cartilage sample with three marked indentation sites.

The sample was first scanned using deionized water with the water pressure no more than 1 kPa and the indentation sites were determined. This process last for about 15 minutes which allowed the cartilage swelling caused by change of the concentration of solution from 0.15 M to approximately 0 M (Wang and Zheng, 2006). The cartilage was first preloaded with a pressure of 20 kPa for 3 seconds, and then it was indented with the pressure increased to approximately 180 kPa within 1 second. The loading and unloading process repeated for 3 cycles in an indentation. The stiffness ratio of cartilage was determined by calculating the slope of pressure applied on the cartilage to the local strain induced in the loading phase. As described in the literature review section (chapter 2), instantaneously induced deformation of a biphasic tissue, such as articular cartilage, consisting of a solid matrix and an interstitial fluid phase, can be modelled as that of an equivalent incompressible single phase elastic material (Hayes et al. 1972, Mak et al. 1987). According to this conclusion, the loading/indentation curve was fitted by linear regression to obtain its slope since the strain was relatively small (no more than 1%). During the measurements, the thickness and deformation of the sample were determined with the 20 MHz ultrasound being calculated from the time of flight and the deflection of the time of flight of ultrasound signals from the surface to the substrate (cartilage/bone interface), respectively. The inner parts of cartilage were mostly unechoic and therefore it was straightforward to determine the echoes from the interfaces. It was found that the calcified cartilage of young bovine was very thin or might even be absent (Toyras et al. 1999). Thus, it is a reasonable assumption that the echoes from the deep cartilage arose from the subchondral bone. The cartilage thickness was determined based on the constant

sound velocity. The speed of ultrasound in bovine cartilage $c_{cartilage}$ was assumed as 1636 m/s (Patil et al. 2004).

The cartilage sample was immersed in normal saline for 2 hours for full recovery (Mow et al. 1989) before the next indentation. The indentation was repeated for three times at each selected site. The stiffness ratio and thickness of each site were obtained as mean values of the three measurements.

3.3.3 Ultrasound Reflection Measurements

Besides the determination of the mechanical properties of articular cartilage, the ultrasound reflection measurements could also provide an evaluation of the quality of cartilage which could suggest diagnosis on the type of tissue degeneration (normal, collagen degradation, PG loss or both) (Laasanen et al. 2002, Hattori et al. 2003). Our water jet ultrasound indentation system could easily obtain A-mode or B-mode ultrasound echogram of articular cartilage for the analysis of the acoustic properties.

During the test, the maximal ultrasound echo amplitude reflected from the articular cartilage surface was recorded six times at each selected site for every cartilage sample at a constant small flow rate (1.08 ± 0.24 mm/s) before the indentation was applied. The peak-to-peak echo amplitude recorded from the intact cartilage sample A_{intact} and that recorded from the sample after digestion treatment A_{digest} at the identical indentation site were compared to investigate if there was significant difference between them.

3.3.4 Evaluation of the Effect of Repositioning

The accuracy of the ultrasonic evaluation highly depends on the position of the ultrasound transducer relative to the indentation site. In this study, we compared the variation of both mechanical properties and ultrasound reflection of the articular cartilage before and after trypsin treatment. During the experimental procedure, the sample was repositioned on the fixation device after it was digested. Therefore, the effect of sample repositioning should be evaluated. Two samples were used for this test. The sample was first assessed by the ultrasound water jet indentation system on the selected test sites; then it was taken away from the platform and immersed into the saline solution. The sample was repositioned to the original place for the repeated test after it was fully recovered. During this process, the orientation of the platform was kept and the position of the sample was marked on the platform. The three-dimensional translating device could retrieve the transducer back to the recorded position of each test site. Thus the same test sites were indented. This process was repeated for three times. The obtained stiffness ratio, thickness and peak-to-peak ultrasound echo amplitude of each test site were used to evaluate the variation caused by the repositioning.

3.3.5 Comparison with Mechanical Indentation

To compare with the measurements using the ultrasound water jet indentation, mechanical indentation was conducted on the same samples. A custom made computer controlled material testing device was used to perform the mechanical indentation. The

system consisted of a 10N load cell, precision motion controller and a computerized data acquisition system. As shown in Figure 3-17, a cylindrical, plane-ended, impermeable, stainless steel indenter with a diameter of 1.6 mm was utilized for the mechanical indentation. The indenter was connected to a load cell (ELFS-T3M, Entran Devices, Inc., Fairfield, NJ, USA, calibrated for a range of 10N) and was installed on a three dimensional translating device (Parker Hannifin Corporation, Irvine, CA, USA). During indentation, the indenter was first moved to the marked test site, and a preload of 0.04 N (a prestress at 20 kPa) was applied to the sample. After 3 seconds holding, the sample was loaded up to a maximal strain of 10% by moving the indenter perpendicularly down to the tissue. The movement of the indenter was controlled by the three dimensional translating device which has a high positional resolution of 0.1 μm. The loading was recorded by the load cell synchronously with the movement of the indenter by the program and the accuracy of the force sampled by the data acquisition card was better than 1 μN. The indentation rate was controlled approximately at 2 mm/s.

The Young's modulus of the cartilage was obtained using Hayes' model (Hayes et al. 1972) from the instantaneous load/indentation response of the sample. For a plane-ended cylindrical indenter, at a given value of the parameters *a/h* and *v*, the relation between the applied force *P*, and the displacement, ω, is given by

$$E = \frac{P(1-\nu^2)}{4a\omega\kappa(a/h,\nu)} \qquad (3\text{-}10)$$

in which *a* is the radius of indenter, *E* Young's modulus, and *v* Poisson's ratio. Values of the scale factor κ were numerically determined for Poisson's ratio *v* ranging from 0.3 to

0.5 (Hayes et al. 1972) and from 0.0 to 0.3 (Jurvelin et al. 1990). For an instantaneous response, the Poisson's ratio of cartilage was regarded as 0.45 (Mak et al. 1987, Wong et al. 2000). The Poisson's ratio can be determined using unconfined or confined compression test (Armstrong and Mow 1982), or optical method (Jurvelin et al. 1997) etc. However, these methods are only suitable for in situ or in vitro test and the sample should be well prepared. Therefore, we didn't conduct experiments to find the exact value of Poisson's ratio at each test site on a bulk bovine cartilage sample. The test should be performed by preparing cartilage samples with the shape fulfilling the requirement of both water jet indentation and confined compression. The thickness of cartilage determined from the ultrasound water jet indentation system was used for the determination of the scale factor κ from the given tables by Hayes et al. (1972).

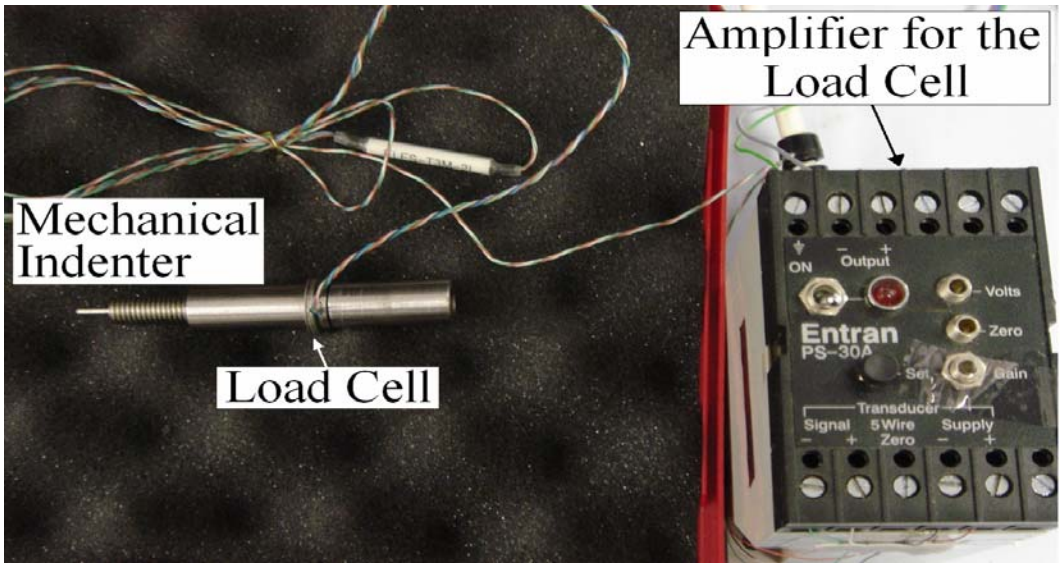

Figure 3-17. A mechanical indenter and its amplifier used for the mechanical indentation on articular cartilage. The indenter is a cylindrical, plane-ended, impermeable, stainless steel one and its diameter is 1.6 mm.

3.3.6 Statistical Analysis

Data were expressed as mean ± standard deviation (SD). For the comparison of various parameters, i.e., the stiffness ratio and thickness obtained by the water jet indentation as well as the Young's modulus measured by the mechanical indentation, paired *t*-test was used to find if there were significant differences between the cartilage samples before and after the trypsin digestion. The Pearson correlation test was used to test the relationship between the stiffness ratio and Young's modulus for both intact samples and the samples after trypsin digestion treatment. One-way ANOVA was conducted to find if there were site-dependent properties of all the cartilage samples before and after digestion. All the statistical analyses were conducted by using the commercial software SPSS (SPSS Inc., Chicago, IL, USA). $P < 0.05$ was used to indicate a significant difference.

The reproducibility of the ultrasound water jet indentation measurement, for stiffness ratio, thickness and ultrasound reflection, i.e. the maximal ultrasound echo amplitude reflected from the articular cartilage surface, were determined using a standardized coefficient of variation (sCV) (Gluer et al. 1995, Blake et al. 1999). The standardized coefficient of variation takes into account the biological range of the measured parameters and it is defined as:

$$\text{sCV} = \frac{CV_{RMS}}{4\sigma_{\mu} / \overline{\mu}} \qquad (3\text{-}11)$$

where σ_μ is the standard deviation of all samples, $\bar{\mu}$ is the average of the population and CV_{RMS} is the root-mean square average of coefficient of variation of the measured parameter. The smaller the sCV value, the better the reproducibility (0% indicates a perfect reproducibility).

3.4 Assessment of Bone -Tendon Junction Tissues

Many trauma surgeries and reconstructive surgeries involve re-establishment of the bone-tendon junction (BTJ) tissues. Experimental and clinical findings have shown that a direct BTJ repair requires longer period of immobilization which may be associated a postoperative weak knee. BTJ, such as patellar tendon-patella junction, is characterized with a unique transitional fibrocartilage zone, with calcified fibrocartilage connecting to bone and non-calcified fibrocartilage connecting to tendon. BTJ healing is slow due to the poor regenerative capacity of the fibrocartilage zone between bone and tendon. To enhance the tissue healing, researchers use postoperative mechanical stimulation, such as low intensity pulsed ultrasound (LIPUS), to accelerate the BTJ repair and the restoration of fibrocartilage zone. It is necessary to assess the mechanical properties and thickness of the transition zone (junction) during the healing process to monitor the formation of a fibrocartilage layer.

3.4.1 Animal Model

Forty-three mature female New Zealand White rabbits (18-weeks-old) were randomly divided into 4 groups and prepared for the experiments. The standard and established

partial patellectomy model was used for BTJ junction repair (Qin et al. 1999; Leung et al. 1999). Under general anesthesia with sodium pentobarbital (0.8 mL·kg-1, i.v., Sigma Chemical Co., St. Louis, MO) and aseptic technique, one of the knees was shaved and approached through an anterolateral skin incision. Transverse open osteotomy was performed between the proximal 2/3 and the distal 1/3 of the patella using an oscillating handsaw with a 0.4-mm thick saw blade (Synthes, Mathys AG, Bettlach, Switzerland). After excising the distal one-third of the patella (35.8 ± 8.2% of the original patella length of all 43 experimental patellae), two holes with 0.8 mm in diameter were drilled vertically along the patellar. Then the patella tendon was sutured directly to the proximal two-thirds of the patella via the two drilled holes with nonabsorbable suture (3/0 Mersilk, Ethicon Ltd. Edinburgh, UK) and protected with figure-of-eight tension band wire (0.4 mm in diameter, Biomet Ltd., Waterton, UK) which was drawn around the superior pole of the patella to the tibia tuberosity to reinforce the ligament repair according to a previous surgical protocol in patients (Hung et al. 1993). After closing the incision using 4-0 absorbable polyglycolic acid suture (Dexon II, Beige Braided, DG. Davis-Geck, UK), antibiotic spray (Nebactin, Byk Gulden Konstanz, Germany) was used for disinfection. A custom-made tension meter was used to standardize the tension of the tension band fixation at the knee flexion angle of 90 degrees before closing the wound. Intramuscular analgestic (Temgestic, 0.5 ml/head/day) was given daily for 3 days after surgery. Immobilization for 6 weeks was followed using an established cast – splints immobilization device with an “open window” on the upper cast (Qin et al. 1997) which allowed placement of ultrasound transducer on the surface of the patella for ultrasound

treatment. Figure 3-18 shows a picture of a typical sample which was harvested at the end of week 6 after operation. The intact contralateral knee was served as control. Figure 3-19 shows a photo of typical control sample, and Figure 3-20 describes the patella-patella tendon complex, indicating the patellar cartilage, fibrocatilage and subchondral bone. Animals were individually kept in metal cages in a central animal house and supplied with standard rabbit food and water.

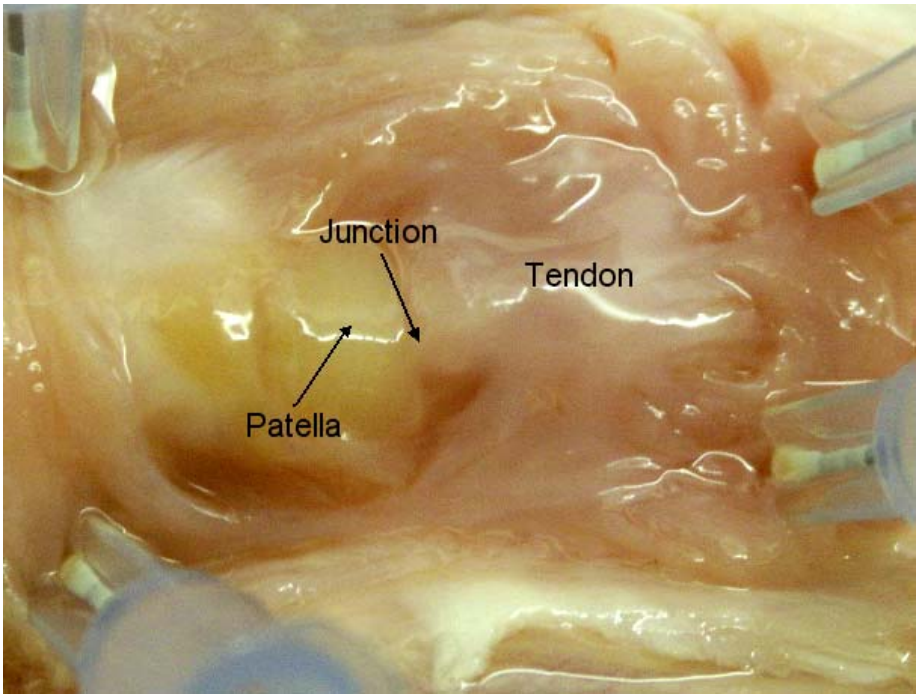

Figure 3-18. A typical sample which was harvested at the end of week 6 after operation. The animal did not get any postoperative treatment during the immobilization for 6 weeks.

The 43 animals were randomly grouped into 4 groups and sacrificed at time intervals of 6, 12, and 18 weeks postoperatively. Animals in Group A did not get any postoperative

treatment. Animals in Group B and D were treated using LIPUS during immobilization from day 3 to the end of week 6. Under sedation with ketamin (0.25 ml/kg, i.m.), LIPUS was delivered by a 2.5 cm diameter ultrasound transducer (SAFHS, Exogen, Inc, USA) via the "open window" of the cast and placed against the anterior surface of the healing

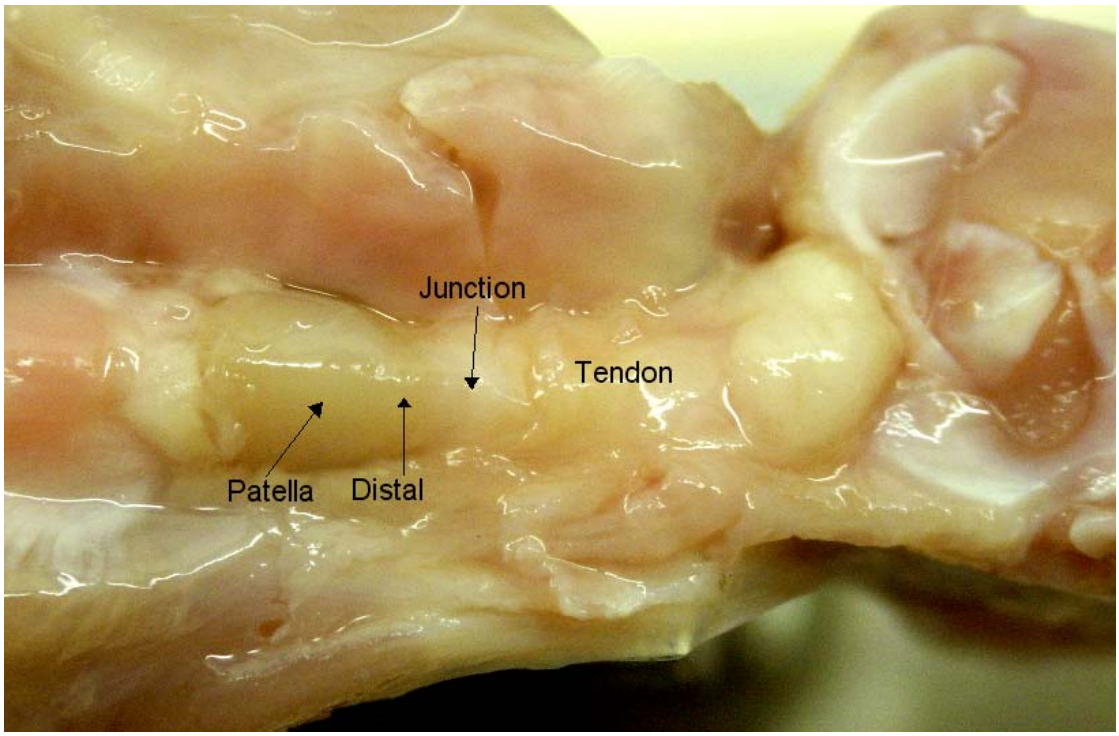

Figure 3-19. A typical control sample harvested from the intact contralateral knee.

junction of the operated knee via coupling gel (Acoustix, Conmed Corp., USA). The ultrasound signal composes a 200 μs burst of 1.5 MHz and 30.0 ± 5.0 mW/cm^2 spatial average and temporal average incident intensity (Hadjiargyrou et al. 1998). The ultrasound treatment was started at 3 days after operation, kept 20 minutes for each day and ended at the end of week 6. At postoperative week 6, fixation devices for immobilization were removed. Animals in Group C and D were treated by surface

functional electronic stimulation (FES). Quadriceps muscles of the previously operated hindlimb were stimulated via a modified surface FES protocol using a BMR-2-Powerstim-Trainer (Freiburg, Germany) (Qin 1992; Qin et al. 1997). The square wave stimuli at 50 Hz (pulse width 20 ms, 1 second on and 2 seconds off for simulating a cyclic tensile loading) were applied daily for 30 minutes, 5 times per week during the immobilization period. The amplitude of the FES was increased from 10% of the maximal contraction of the intact contralateral knee, with an increment of 5% per week. The surface FES treatment was applied from the beginning of week 7 to the end of week 12. Table 3-2 gives the descriptions of the animal models.

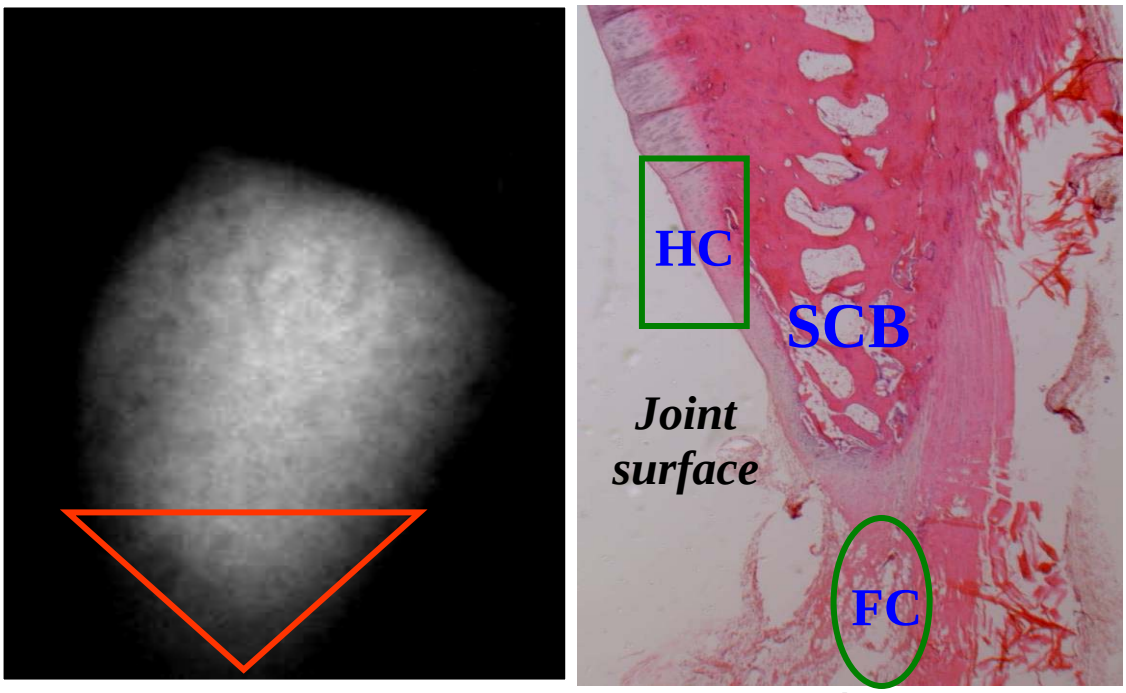

(a) (b)

Figure 3-20. Patella-patella tendon complex: (a) the anterior-posterior digital radiograph of patella; (b) mid-sagittal section of distal patella and patellar tendon, prepared from the distal patella within the triangle region in (a). FC: firocartilage; HC: hyaline cartilage; SCB: subchondral bone. (H&E staining, 16×).

Table 3-2. Descriptions of the samples for the bone-tendon junction repair assessment.

Group		Time for sample harvesting after operation					
		End of week 6 (Immobilization with or without LIPUS)		End of week 12 (Remobilization with or without FES)		End of week 18 (Remobilization without any treatment)	
		Control	Post-operative	Control	Post-operative	Control	Post-operative
A	Without any postoperative treatment	n = 6	n = 6	n = 2	n = 3	n = 3	n = 3
B	With LIPUS starting from day 3 to end of week 6	n = 4	n = 4	n = 5	n = 5	n = 7	n = 7
C	With surface FES from begin of week 7 to end of week 12			n = 3	n = 3	n = 6	n = 7
D	With LIPUS starting from day 3 to end of week 6, followed by surface FES from begin of week 7 to end of week 12			n = 3	n = 3	n = 2	n = 2

3.4.2 Stiffness and Thickness Measurement with Ultrasound Water Indentation

All the samples were stored at -20^{o}C before use. The sample was first thawed in normal saline solution (0.15 M NaCl) at room temperature 20^{o}C for 1 hour, and then it was fixed

by a fixation device (Figure 3-21) with the AC surface facing the ultrasound transducer (Figure 3-22) perpendicularly. The sample was first scanned along the patella-junction-tendon direction with a scan step at 50 μm under a preloading of 2.12 ± 0.07 kPa by the water jet ultrasound indentation system. The scan line was carefully selected by obtaining the maximal ultrasound reflection echoes from the interface of water/AC surface, usually at the most prominent convex site of the patella. The scan distances were typically 6 mm for a control sample and 5 mm for a postoperative sample. After the first scan was finished, the sample was quickly scanned again along the identical line under a pressure of 135.32 ± 0.36 kPa. Figure 3-23 shows a typical ultrasound image obtained from the scanning in which the cartilage, junction and the tendon parts could be clearly identified.

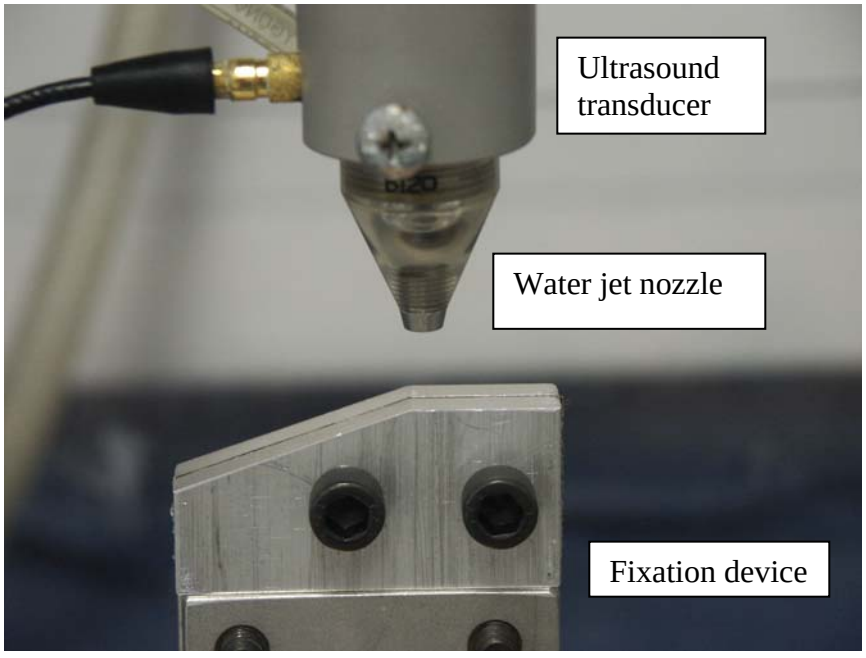

Figure 3-21. The fixation device for the bone-tendon junction tissue assessment.

Figure 3-22. The sample was fixed by the fixation device with the AC surface facing the ultrasound transducer.

To determine the tissue thickness, the ultrasound signals obtained from the first scan were analyzed. Three sites from each part, including patella cartilage, the distal of cartilage, junction and tendon (Figure 3-23) were selected, and the thickness at each site was calculated from the time of flight of ultrasound signals from the surface to the substrate (cartilage/bone interface or tendon/stiff substrate interface). The speed of ultrasound in cartilage $c_{cartilage}$ was assumed as 1636 m/s (Patil et al. 2004) and in tendon c_{tendon} was assumed as 1580 m/s (Duck 1990). The averaged values calculated from the three sites were used as the thickness value for each tissue part.

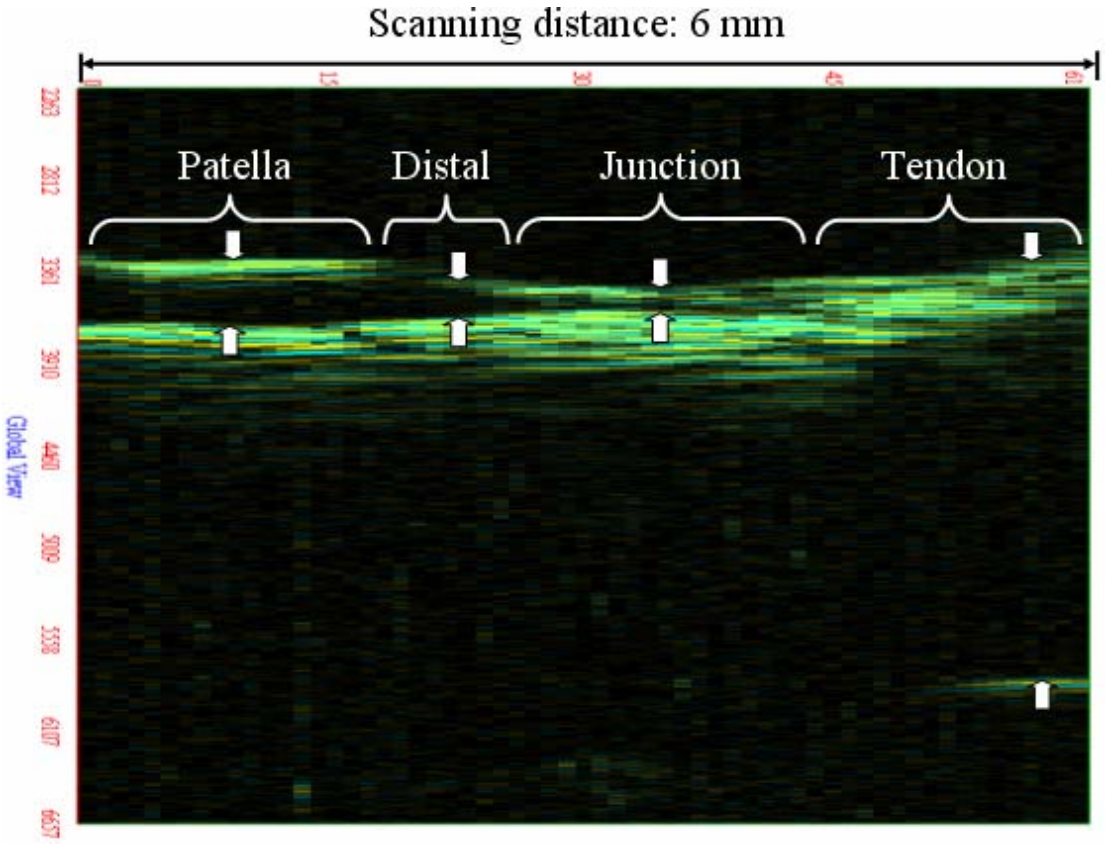

Figure 3-23. A typical ultrasound image obtained from the scanning in which the patella cartilage, the distal of patella, junction and the tendon parts could be clearly identified.

For the determination of the tissue stiffness, the thickness change Δh of each selected site under two consequent scans was calculated from the deflection of the flight of time of ultrasound echoes Δt. The stiffness was then calculated by the force applied to the tissue F which was calculated from the pressure difference ΔP_{ss}, divided by the thickness change Δh (Equation 3-12):

$$\text{Stiffness} = F / \Delta h, \qquad (3\text{-}12)$$

where $\Delta h_{cartilage} = \Delta t \times c_{cartilage}$ for the deformation of cartilage, distal of cartilage, and junction; $\Delta h_{tendon} = \Delta t \times c_{tendon}$ for the deformation of tendon. The stiffness ratio was

calculated by the pressure divided by the local strain, and the Young's modulus could be derived from the stiffness ratio according to the relationship between the stiffness ratio and the instantaneous Young's modulus which was obtained from the bovine articular cartilage (Sec. 3.3.5). Same as the thickness determination, the averaged values of the stiffness and Young's modulus calculated from the three sites were used as the value of stiffness and Young's modulus for each tissue part, respectively.

3.4.3 Statistical Analysis

Data were expressed as mean ± SD. For the control samples, comparisons of both stiffness ratio and thickness of patella, the distal of patella, junction and patella were made by using two-way ANOVA to investigate if the group separation and the sacrificed time would significantly affect these parameters. If no significant difference was found among different groups or at different sacrificed time intervals, the parameters were pooled and averaged values were given at different test regions. The averaged values at patella, junction and patella would be used as references and be compared with those obtained from the post-operative samples. The results of the post-operative samples were analyzed in two ways: 1) paired *t*-tests were conducted between the control sample and the post-operative samples; 2) two-way ANOVA was used to analyze if different treatments and sacrificed time intervals would significantly affect the stiffness ratio and thickness. All the statistical analyses were conducted by using the commercial software SPSS. $P < 0.05$ was used to indicate a significant difference.

CHAPTER IV RESULTS

4.1 System Development and Validation

4.1.1 Results of System Calibration

The calibration measurements indicated highly linear responses for both pressure and force transducers (r = 0.99 for the pressure sensor, Figure 4-1; r = 0.99 for the load cell, Figure 4-2). Moreover, it was found that there was a linear relationship (r = 0.99) between the overall force applied on the platform F_{ov} collected by the load cell and the water pressure within water pipe P_{wp} measured by the pressure sensor (Figure 4-3). Since the pressure applied on the phantom surface P_{ss} was calculated from the overall force applied on the platform F_{ov} divided by the cross-section area of the water jet, such a relationship suggested that we could calculate the pressure applied on the phantom surface P_{ss} directly from the pressure measured within the water pipe $P_{wp.}$ Hence, the use of the load cell is not a must. This finding would help to design the hand-held ultrasound water jet indentation system.

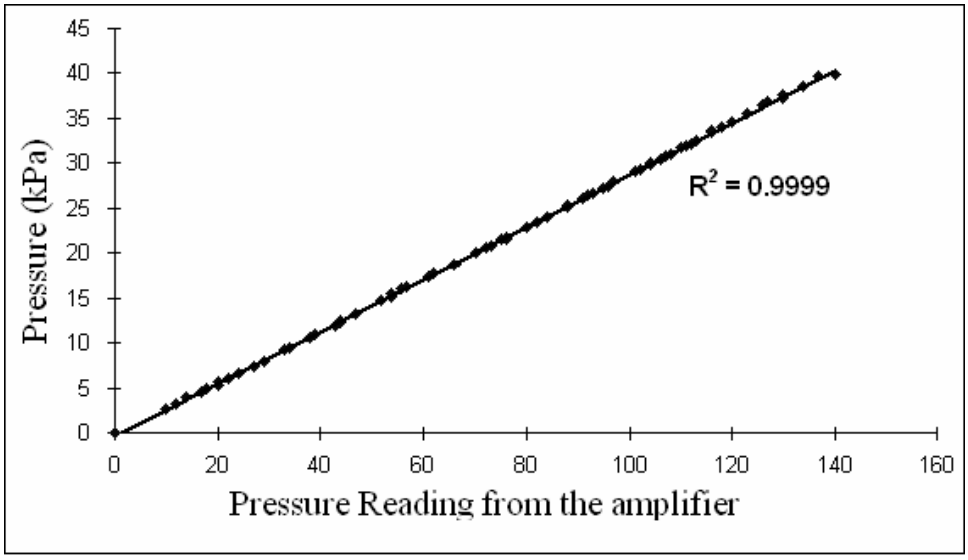

Figure 4-1. Calibration of the pressure sensor: relationship between the applied pressure and the reading from the amplifier.

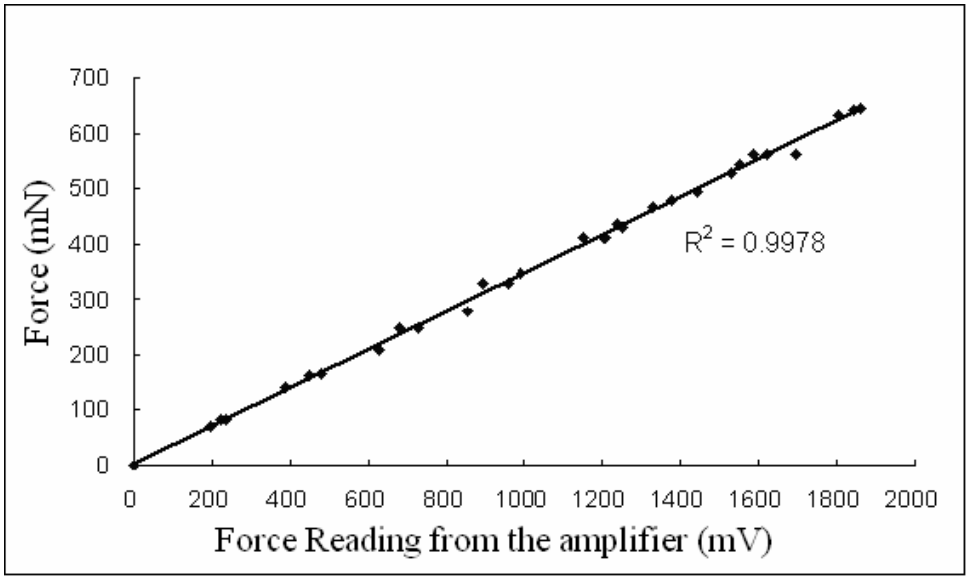

Figure 4-2. Calibration of the load cell: relationship between the applied force and the reading from the amplifier.

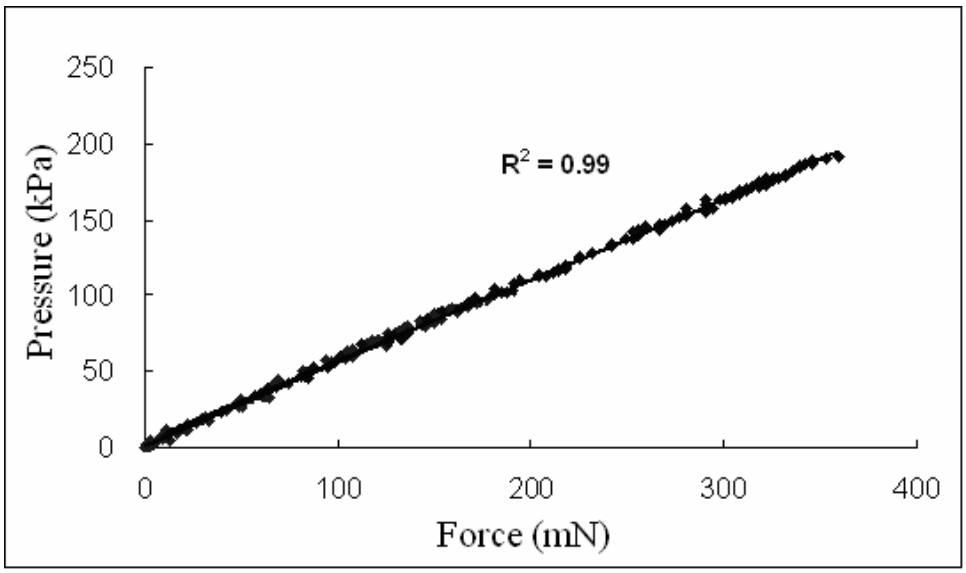

Figure 4-3. Relationship between the overall force applied on the platform and the water pressure measured within the water pipe.

4.1.2 Results of System Validation

4.1.2.1 Measurement Results Using the Ultrasound Water Jet Indentation System

Figure 4-4(a) shows the pressure/deformation curves during the loading and unloading cycles applied on phantom A, and Figure 4-4(b) shows the relationship between the pressure P_{ss} and the surface deformation of the phantom. It was found that the relationship between the deformation of the phantom and the applied water pressure loading was linear; therefore, the data were fitted using linear regression (average r = 0.99). The obtained slope, i.e. the ratio of the applied pressure to the relative deformation which was calculated by the surface deformation divided by the thickness of the phantom, was defined as the stiffness ratio of the phantoms with a unit of kPa. Table 4-1 lists the measured stiffness ratio and the thickness of each piece of phantom.

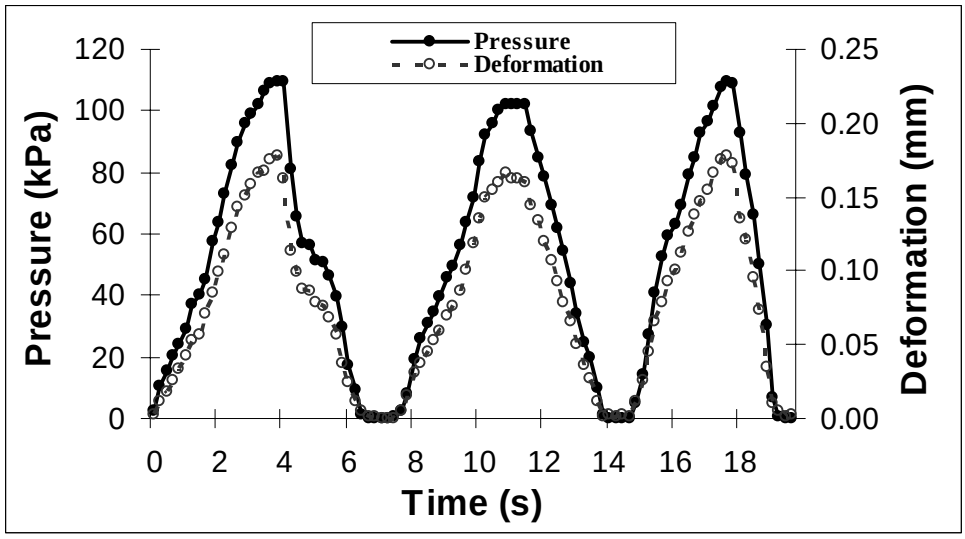

(a)

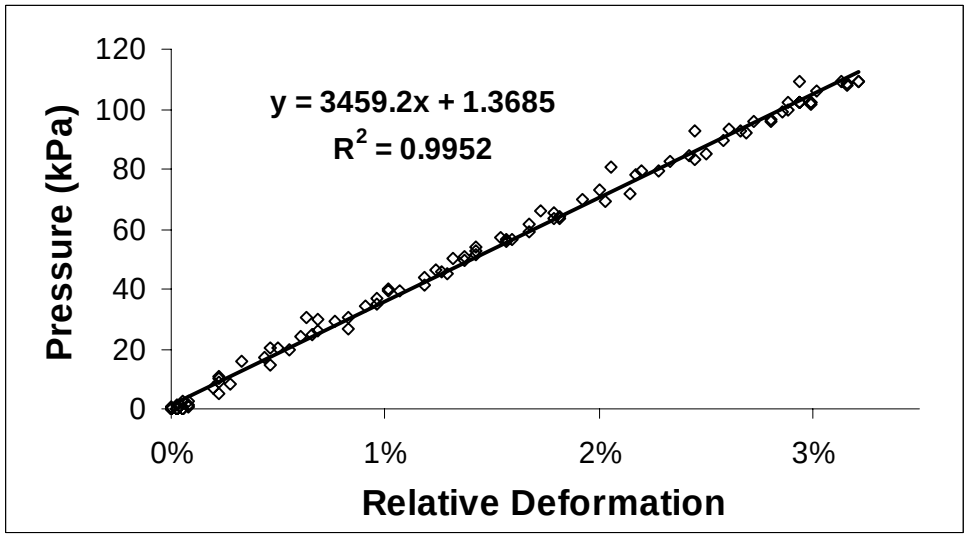

(b)

Figure 4-4 (a). Pressure-deformation curves obtained during the loading and unloading cycles applied on one uniform phantom. (b) The relationship between the pressure measured within the water pipe and the relative deformation of the phantom.

Table 4-1. The stiffness ratio and the thickness of each piece of phantom.

Phantom	**Stiffness ratio (kPa)**					**Thickness***
	test 1	test 2	test 3	*Mean*	*SD*	(mm)
A1a	2043.1	2101.1	2084.8	*2076.3*	*29.9*	5.23
A1b	2064.8	2106.7	2056.1	*2075.9*	*27.1*	5.16
A1c	2090.6	2066.4	2067.2	*2074.7*	*13.7*	5.21
A2a	3823.4	3831.2	3767.8	*3807.5*	*34.6*	9.85
A2b	3958.4	3937.8	3988.9	*3961.7*	*25.7*	10.31
A2c	3624.8	3594.1	3615.8	*3611.6*	*15.8*	10.03
A3a	4939.6	5033.8	5021.0	*4998.2*	*51.1*	15.25
A3b	5038.7	5136.5	5164.3	*5113.2*	*66.0*	15.06
A3c	4360.8	4447.4	4415.6	*4407.9*	*43.8*	15.05
B1a	2685.7	2744.5	2773.4	*2734.6*	*44.7*	5.34
B1b	2382.5	2430.0	2448.3	*2420.3*	*33.9*	5.38
B1c	2663.4	2872.4	2893.0	*2809.6*	*127.0*	5.53
B2a	4571.5	4528.2	4584.2	*4561.3*	*29.3*	10.2
B2b	4305.4	4277.9	4247.5	*4276.9*	*28.9*	10.22
B2c	3935.7	3892.4	3884.8	*3904.3*	*27.5*	10.28
B3a	4630.3	4798.0	4954.7	*4794.3*	*162.2*	15.43
B3b	5322.3	5427.5	5427.6	*5392.5*	*60.8*	15.28
B3c	5610.4	5570.5	5605.2	*5595.4*	*21.7*	15.35
C1a	2412.0	2491.1	2530.6	*2477.9*	*60.4*	5.25
C1b	2215.0	2290.8	2242.2	*2249.3*	*38.4*	5.28
C1c	2418.6	2483.0	2537.7	*2479.8*	*59.6*	5.17
C2a	4057.7	3992.0	4063.5	*4037.7*	*39.7*	10.08
C2b	3208.8	3281.4	3323.7	*3271.3*	*58.1*	10.07
C2c	4139.2	4128.4	4153.6	*4140.4*	*12.6*	10.14
C3a	4797.7	4880.6	4914.6	*4864.3*	*60.1*	15.22
C3b	4493.1	4419.9	4468.4	*4460.4*	*37.3*	15.06
C3c	5031.6	5160.7	4982.8	*5058.4*	*91.9*	15.08

*The thickness was measured using a micrometer.

The measurements of the stiffness ratio of the phantoms showed a good repeatability (ICC>0.99, Intra-class Correlation Coefficient, SPSS Inc. Chicago, USA) for the three tests. The stiffness ratio of the phantoms ranged from 2075 to 5595 kPa.

4.1.2.2 Mechanical Properties of Uniform Phantoms Measured from Uniaxial Compression Test

The mechanical properties of the phantoms were found to be dependent on the applied strain. Therefore, the Young's moduli and Poisson's ratios were measured at the strain level according to the indentation depth on each phantom by using the noncontact water indentation system. Table 4-2 lists the Young's modulus and the Poisson's ratio of each phantom obtained from the uniaxial compression test. The results showed a good repeatability with an *ICC=0.99* for the measurement of Young's modulus and an *ICC=0.98* for the measurement of Poisson's ratio respectively. The Young's modulus of the phantoms ranged from 273 to 522 kPa and their Poisson's ratio ranged from 0.26 to 0.44. It was noted that the phantoms could have different moduli even if they were made from the same silicone materials.

4.1.2.3 Comparison of the Results between Ultrasound Water Jet Indentation and the Uniaxial Compression Test

A good linear relationship between the compressive Young's modulus and the stiffness ratio was found with the correlation coefficient $r = 0.87$ ($n = 27$) (Figure 4-5). The Young's modulus, E_w, was estimated from the obtained relationship between the

Table 4-2. The Young's modulus and Poisson's ratio of each piece of phantom.

Phantom	**Young's modulus (kPa)**					**Poisson's ratio**				
	test 1	test 2	test 3	*Mean*	*SD*	test 1	test 2	test 3	*Mean*	*SD*
A1a	283.5	299.8	291.5	*291.6*	*6.7*	0.40	0.41	0.40	*0.40*	*0.00*
A1b	285.1	295.2	286.3	*288.9*	*4.5*	0.38	0.39	0.39	*0.39*	*0.01*
A1c	298.1	302.2	290.3	*296.9*	*4.9*	0.43	0.43	0.43	*0.43*	*0.00*
A2a	293.2	302.6	308.5	*301.4*	*7.8*	0.32	0.35	0.36	*0.34*	*0.02*
A2b	354.5	345.8	351.5	*350.6*	*4.4*	0.41	0.42	0.41	*0.41*	*0.00*
A2c	341.7	340.6	344.0	*342.1*	*1.7*	0.42	0.42	0.43	*0.42*	*0.00*
A3a	376.3	376.4	385.3	*379.3*	*5.2*	0.43	0.43	0.43	*0.43*	*0.00*
A3b	392.2	393.8	390.6	*392.2*	*1.6*	0.40	0.41	0.38	*0.40*	*0.02*
A3c	353.8	365.8	373.8	*364.5*	*10.1*	0.39	0.40	0.42	*0.40*	*0.01*
B1a	328.3	330.0	331.3	*329.9*	*1.5*	0.35	0.32	0.32	*0.33*	*0.02*
B1b	289.6	283.4	286.3	*286.4*	*3.1*	0.33	0.34	0.34	*0.34*	*0.01*
B1c	336.8	346.8	350.2	*344.6*	*7.0*	0.33	0.32	0.32	*0.33*	*0.01*
B2a	483.8	464.2	464.1	*470.7*	*11.4*	0.41	0.40	0.38	*0.40*	*0.01*
B2b	370.7	386.8	389.4	*382.3*	*10.1*	0.25	0.27	0.25	*0.26*	*0.01*
B2c	363.5	342.5	365.0	*357.0*	*12.6*	0.29	0.33	0.31	*0.31*	*0.02*
B3a	495.4	513.8	507.8	*505.7*	*9.4*	0.38	0.40	0.40	*0.39*	*0.01*
B3b	521.9	526.3	520.1	*522.8*	*3.2*	0.41	0.43	0.43	*0.42*	*0.01*
B3c	489.8	512.0	513.1	*505.0*	*13.1*	0.42	0.43	0.44	*0.43*	*0.01*
C1a	291.0	286.8	290.5	*289.4*	*2.3*	0.25	0.28	0.28	*0.27*	*0.02*
C1b	268.2	263.3	288.2	*273.2*	*13.2*	0.30	0.30	0.30	*0.30*	*0.00*
C1c	304.3	296.0	327.9	*309.4*	*16.6*	0.38	0.37	0.39	*0.38*	*0.01*
C2a	371.6	385.9	394.8	*384.1*	*11.7*	0.31	0.30	0.31	*0.31*	*0.01*
C2b	358.8	341.8	352.3	*351.0*	*8.6*	0.33	0.34	0.30	*0.32*	*0.02*
C2c	396.1	382.8	402.3	*393.7*	*9.9*	0.32	0.33	0.35	*0.33*	*0.01*
C3a	400.8	405.4	397.8	*401.3*	*3.8*	0.40	0.40	0.41	*0.41*	*0.01*
C3b	388.4	396.7	409.8	*398.3*	*10.8*	0.40	0.39	0.40	*0.40*	*0.00*
C3c	430.2	444.4	446.0	*440.2*	*8.7*	0.45	0.44	0.45	*0.44*	*0.00*

stiffness ratio and the compressive Young's modulus, *E*, of the phantoms. A Bland-Altman plot (Figure 4-6) was added to give indication of the size of errors between E_w and *E*. The mean difference $\bar{d}$ was 0.02 kPa and the standard deviation *s* was 35.43 kPa.

From the Bland-Altman plot, most of the differences lied between $\bar{d}$ - *2s* and $\bar{d}$ + *2s*, therefore, the result was acceptable for clinical applications (Bland and Altman, 1986). The thickness of the phantom was also significantly correlated with the Young's modulus ($P < 0.001$, linear regression by SPSS). Moreover, significant correlation between the stiffness ratios and the Poisson's ratios was found ($P = 0.04$). However, the extraction of the intrinsic mechanical properties of the test materials from the water indentation needs further investigations.

The phantom study showed a good agreement between the stiffness ratio measured using the ultrasound water jet indentation system and the compressive Young's modulus measured by uniaxial compression test using a developed compression device. Such a result indicated that this novel system was feasible to quantitatively measure materials with different stiffness although the relationship within the Young's modulus, Poisson's ratio, thickness and the indentation force could not be precisely described for the water indentation model. The stiffness ratio could be used as an effective index to presenting the stiffness of the measured material.

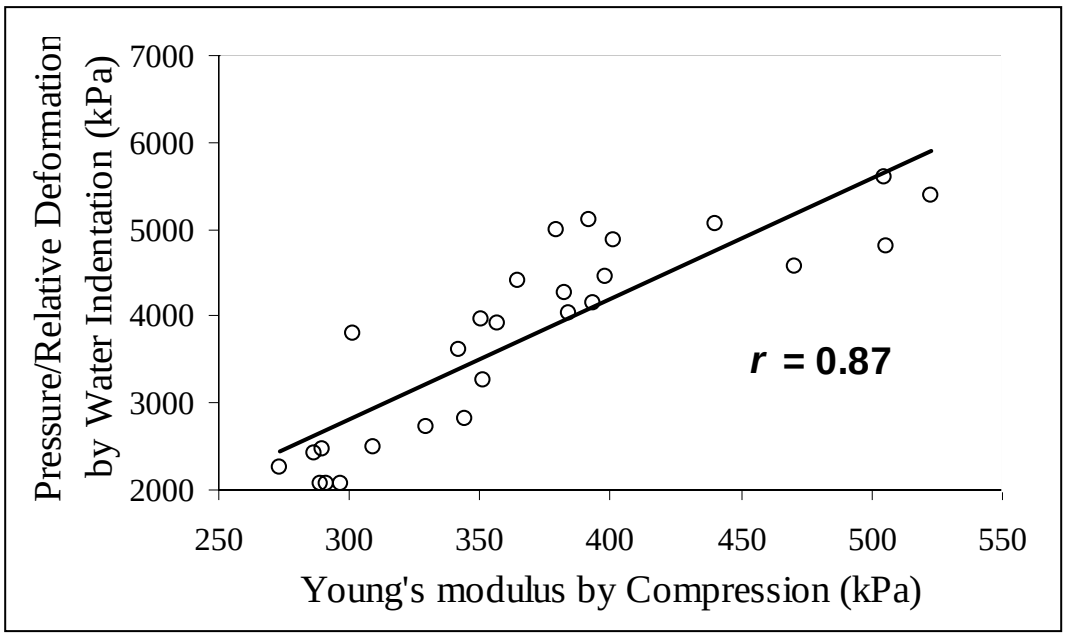

Figure 4-5. The correlation between the compressive Young's modulus and the stiffness ratio obtained using the ultrasound water indentation (r = 0.87, n = 27).

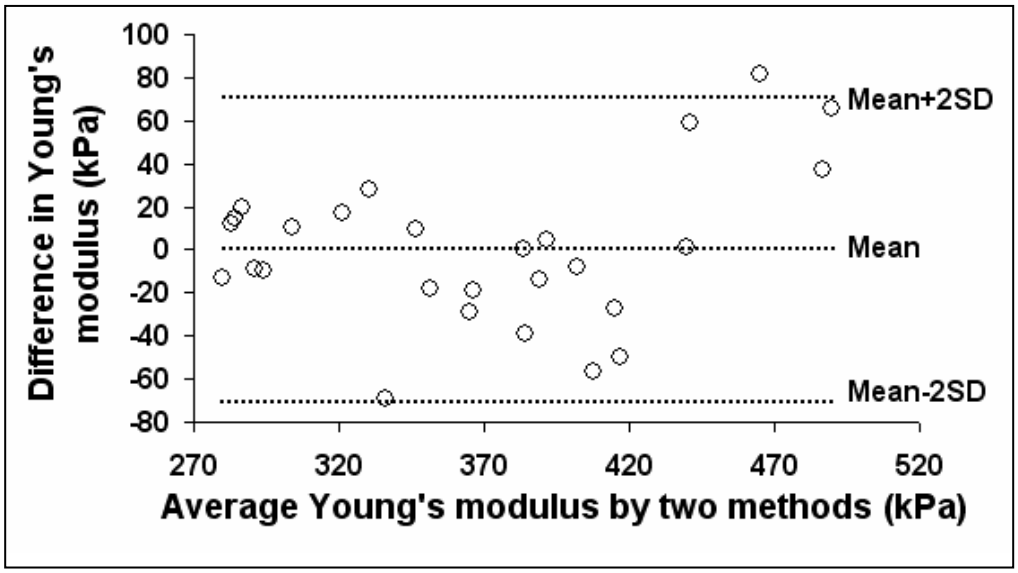

Figure 4-6. Bland-Altman plot to test the agreement between the estimated Young's modulus by water indentation and the measured modulus by compression.

4.1.3 Modeling of Interaction between Water Jet and Soft Tissue

According to the calibration result, the relationship between the pressure within the water pipe P_{wp} and overall force applied on the platform F_{ov} was:

$$P_{wp} = 565.89 \times 10^3 F_{ov}, \quad (4\text{-}1)$$

The pressure applied at the sample surface P_{ss} was assumed as:

$$P_{ss} = F_{ov}/A_{ci}, \quad (4\text{-}2)$$

where A_{ci} is the area of initial contact interface between the water jet and the sample. Since the distance between the water jet head and the sample was only about 5 mm during indentation, A_{ci} was assumed to be equal to the cross area of the water jet head A_2. Hence,

$$P_{ss} = F_{ov}/A_2 = 0.598\, P_{wp} \quad (4\text{-}3)$$

Such an estimation of the pressure on tissue surface was based on the assumption that the contact area between the water jet and the phantom was kept as a constant, and the reaction force measured under the platform was equal to the force applied on the phantom.

On the other hand, the relationship between the pressure within the water pipe P_{wp} and the flow rate measured at the nozzle head v_2 is shown in Figure 4-7. The diameters of the water pipe and the water jet were 3.525 mm and 1.94 mm respectively. The height between point 1 and 2 was 8 cm. Therefore, Equation 3-6 could be rewritten as the follows:

$$P_{wh} = p_{wp} + \frac{\rho}{2} \cdot v_2^2 \cdot (1 - \frac{A_2^2}{A_1^2}) + \rho \cdot g \cdot h_{ph}$$

$$= (1 + \frac{499}{2171.3}(1 - \left(\frac{1.94}{3.525}\right)^4)) \cdot P_{wp} + 3129.6$$

$$= 1.2087\ P_{wp} + 3129.6 \qquad (4\text{-}4)$$

The relationship between P_{wh} and P_{ss} needs further investigation since the nonlinear behaviours of fluid would occur during the deformation of phantom, particularly for a large deformation. Therefore, it is expected that the deformation profile as well as the pressure distribution along the interaction interface may keep changing with the increase of the water jet pressure.

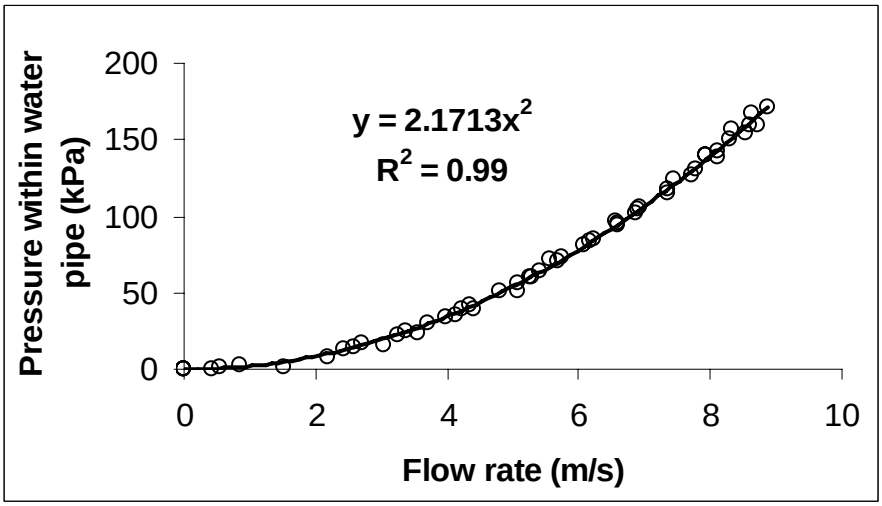

Figure 4-7. The relationship between the pressure within the water pipe P_{wp} and the flow rate measured at the nozzle head v_2.

The deformation profile of the phantom under the indentation induced by the water jet was investigated by the ultrasound B-scan machines. Figure 4-8 shows the deformation

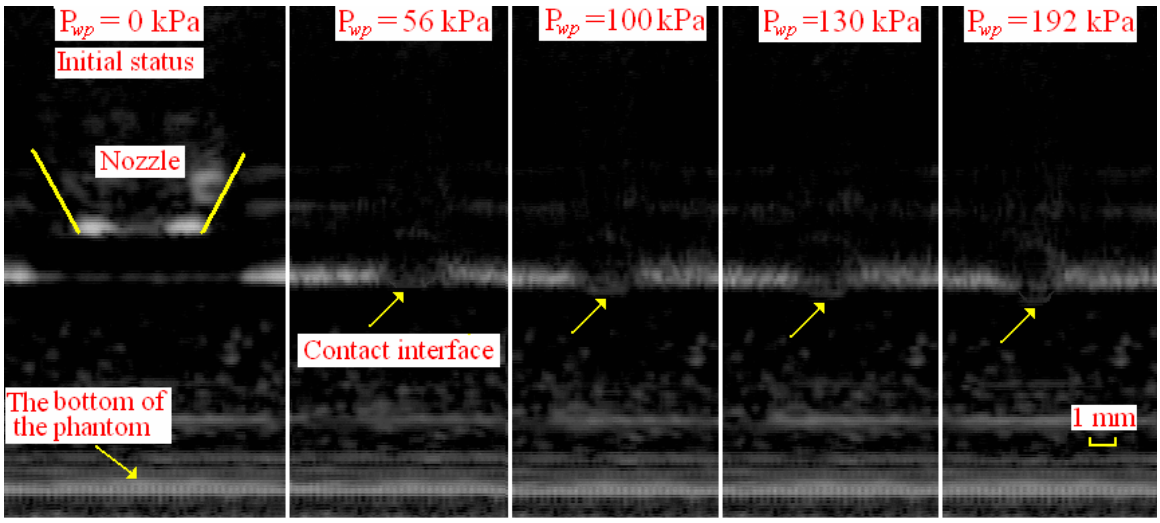

Figure 4-8. The deformation profiles of the phantom recorded by the ultrasound B-mode scanner (SonoSite) at different pressure levels. The arrows indicate the contact interface between the water jet and the phantom.

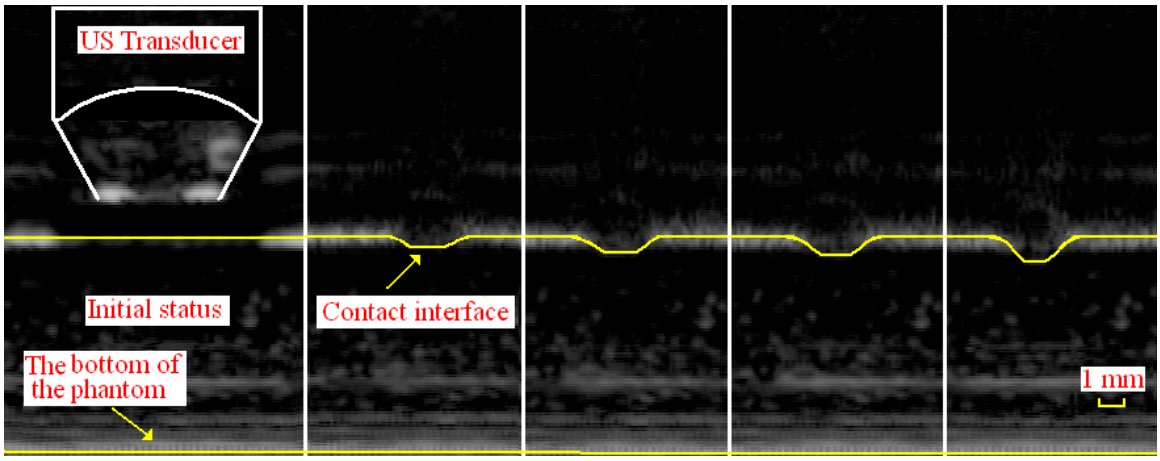

Figure 4-9. The lines were manually drawn for a clear presentation of the deformation profiles of the phantom under different water jet loading.

profiles recorded by the “Sonosite” at different pressure levels. The arrows indicate the contact interfaces between the water jet and the phantom. The profiles are clearly drawn by the lines in Figure 4-9. It was found that the deformation profile was relatively flat

during the indentation process, although the resolution of the images was not good enough for us to draw the conclusion.

4.2 Phantom Study for Modulus Imaging

4.2.1 Results of One-dimensional Scan on the Phantom

Figure 4-10a shows the comparison of the M-mode ultrasound images obtained under two different pressures (0 and 58 kPa). It could be observed that the surface of the combined phantom was not flat. Figure 4-10b is the deformation distribution along the scanned line derived from Figure 4-10a. The result showed that under a certain pressure, the deformation of the region made from material A was larger than that made from material B, i.e. the region made from material A was softer than that from material B. The Young's moduli of these two regions were 288 ± 2 and 433 ± 5 kPa, respectively.

The measured deformation distribution under a certain pressure well demonstrated the stiffness distribution of the combined phantom. The preliminary results demonstrated the feasibility of using the water indentation to map the distribution of the stiffness ratio of soft tissues.

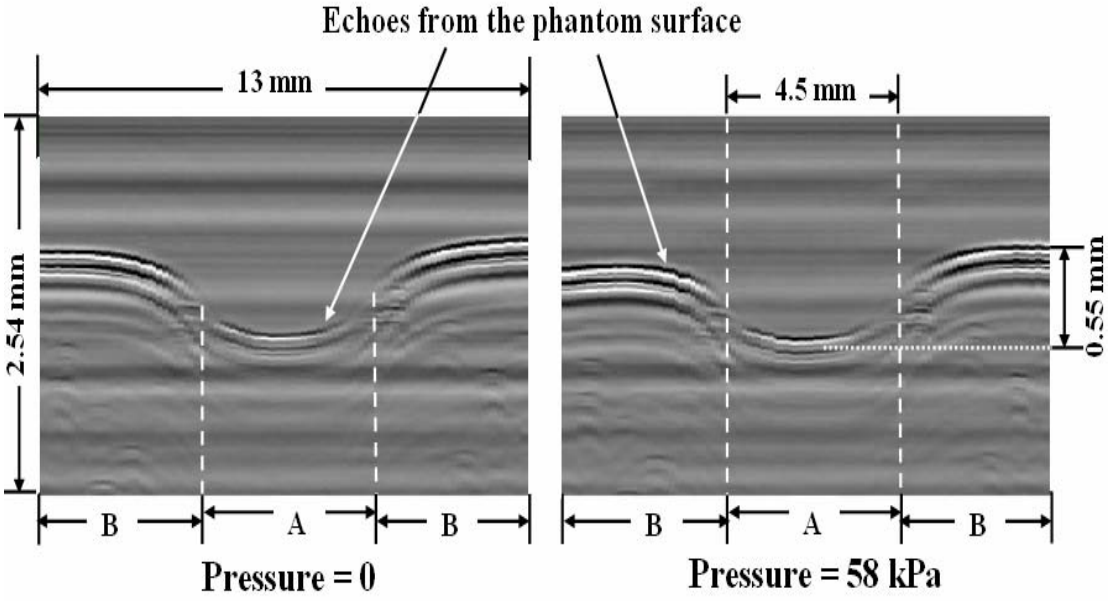

(a)

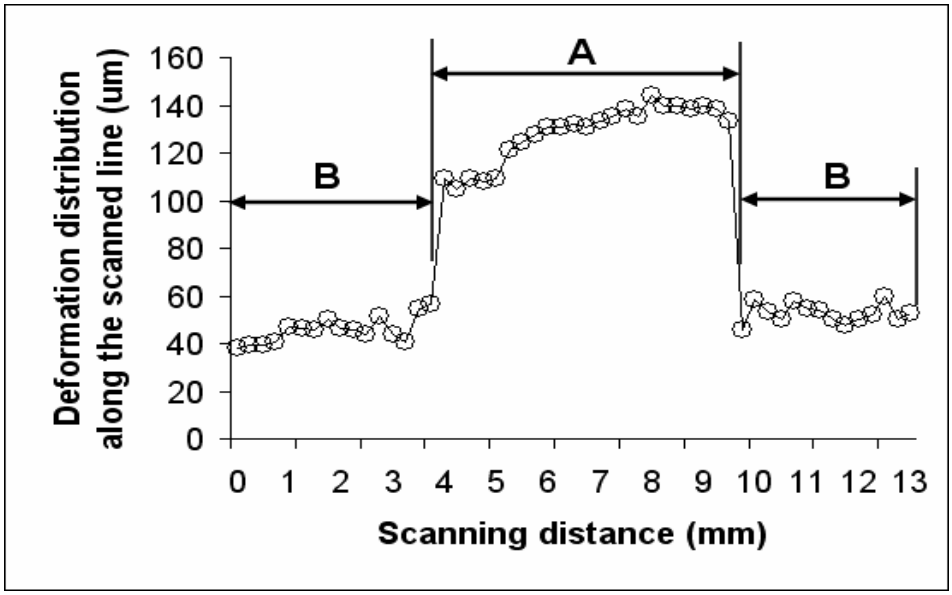

(b)

Figure 4-10. Typical results of one-dimensional scanning on the combined phantom. (a) Comparison of the M-mode ultrasound images obtained under two different pressures. (b) The deformation distribution along the scanned line as derived from (a).

4.2.2 Results of C-scan on the Phantom

Figure 4-11 shows a typical stress and strain data set of a gel phantom with a 15 g/L agar weighted concentration. It is obvious that the phantom behaved as an approximately linear elastic material in this strain range. The slope of the loading portion was chosen to calculate the modulus (stress/strain) of the sample, where the stress was calculated using the force applied on the phantom surface by the water jet divided by the cross-section area of the water beam, and the strain was calculated using the local deformation divided by the original thickness. Figure 4-12 shows the Young's modulus of each phantom measured by the material testing machine using the uniaxial compression test. The actual modulus contrasts for phantom CP1 to CP6 were thus obtained (see Table 3-1).

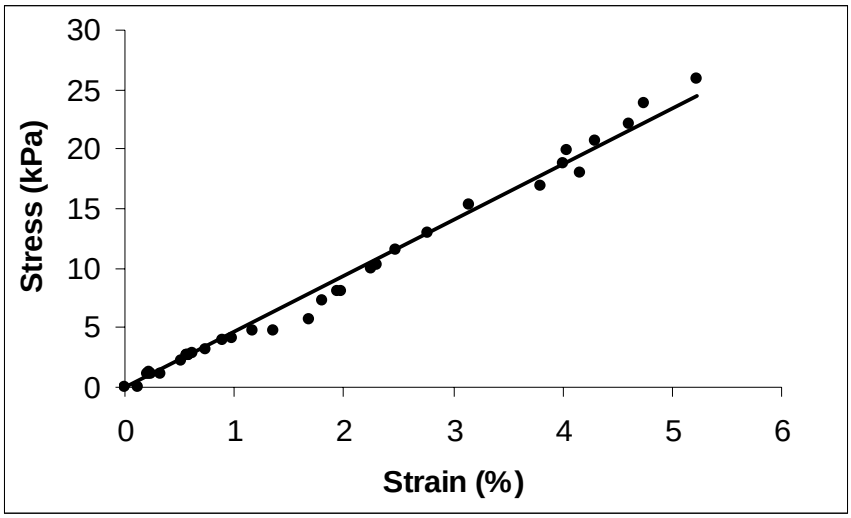

Figure 4-11. A typical stress-strain curve obtained from a gel sample with a 15 g/L agar weighted concentration using water jet ultrasound indentation. The slope of the loading curve was used to calculate the stiffness ratio.

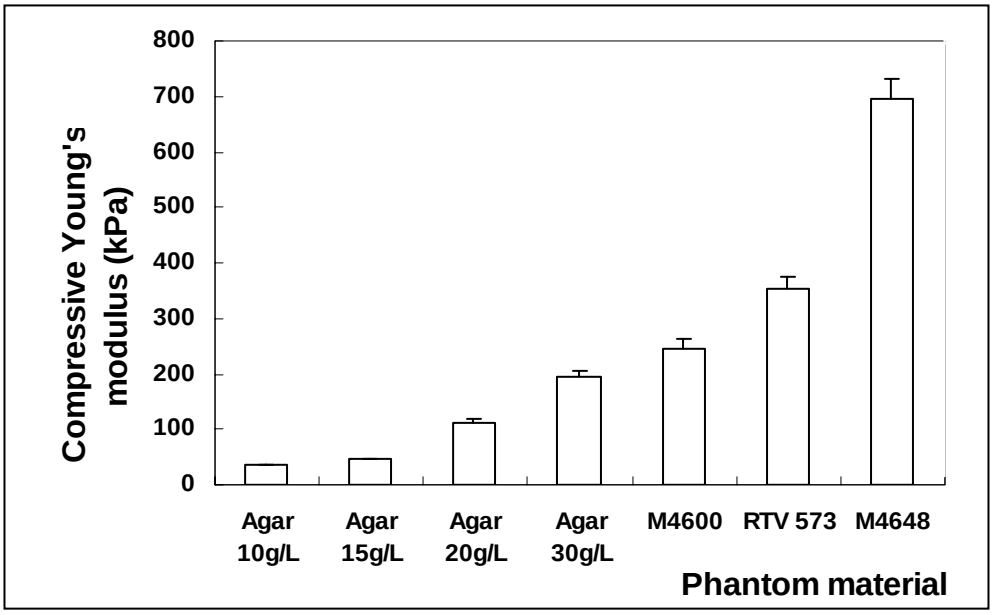

Figure 4-12. The compressive Young's modulus of each phantom material which was listed in Table 1. The modulus was measured by the uniaxial compression test using the material testing machine.

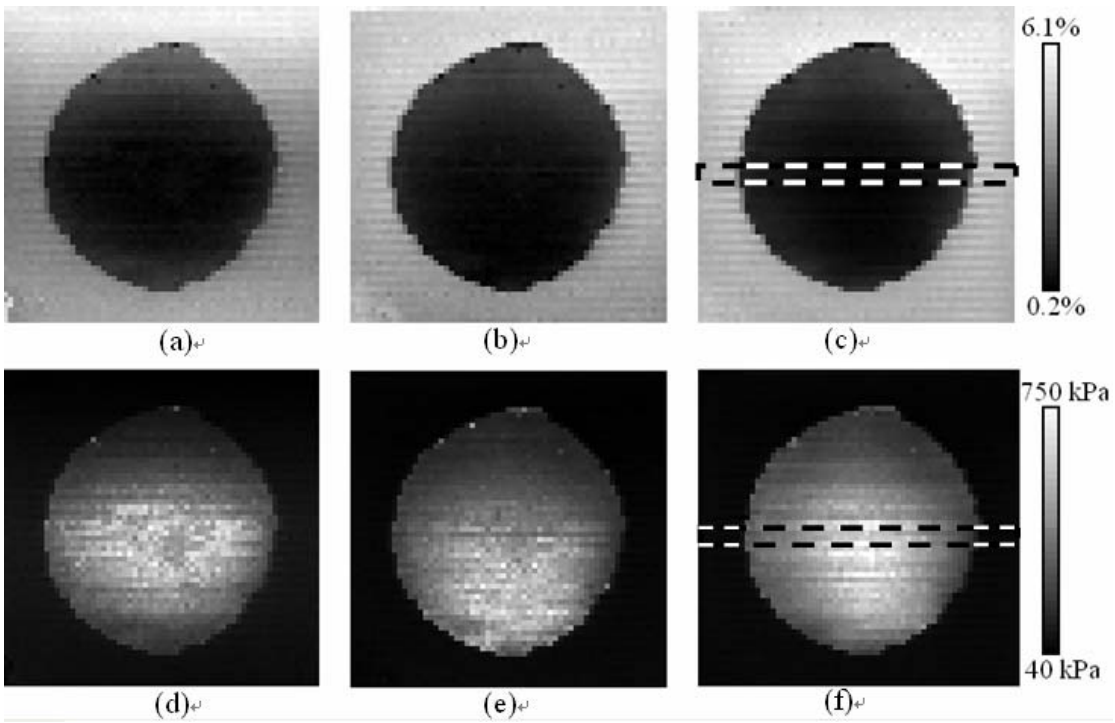

Figure 4-13. Typical strain and modulus images of a phantom named CP2 with a stiffer inclusion (the diameter of the inclusion was 8 mm) obtained under different indentation levels. The scanning area was 12 mm × 12 mm with a step of 0.2 mm. Figures (a), (b) and (c) are the strain images obtained under different pressure levels, i.e. from 0 to 7.3 kPa, from 0 to 10.7 kPa, and from 0 to 15.5 kPa respectively and figures (d), (e), (f) are the corresponding modulus images. The average strains of the whole background materials were 2.0%, 2.7%, and 4.0% respectively. The dashed rectangles indicated the regions used for the plot of strain and modulus profiles in Figure 4-14.

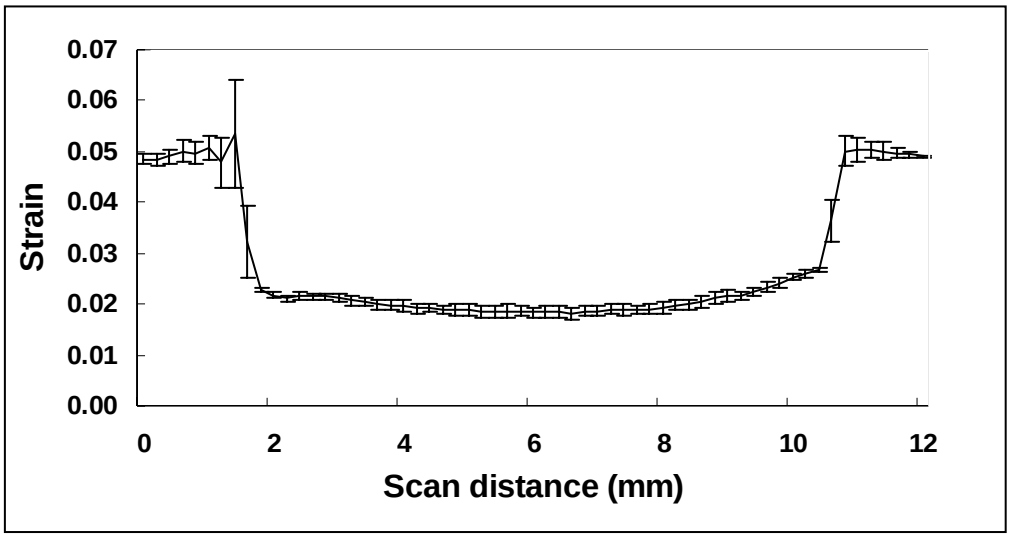

(a)

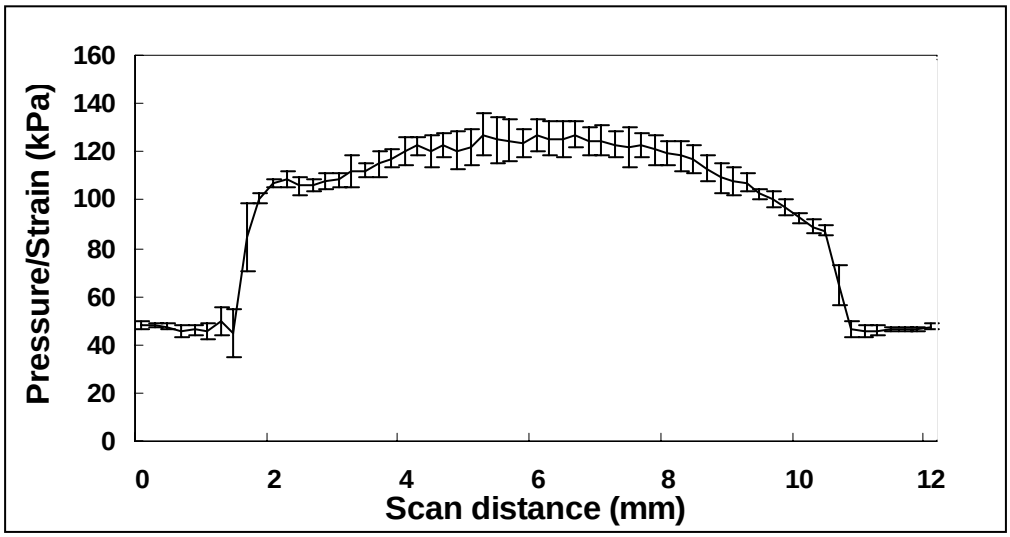

(b)

Figure 4-14. (a) Average strain and (b) corresponding modulus profiles taken from the center of the strain image (Figure 4-13c) and the corresponding modulus image (Figure 4-13f). The error bar indicates the strain and modulus variation across 0.6-mm wide region around the center. The 0.6-mm wide region was indicated by the dashed rectangles in Figure 4-13. The scan distance means the horizontal distance of a measurement region with reference to the left side of the image.

Figure 4-13 shows the typical strain and modulus images of a phantom obtained under different indentation levels. Images (a), (b) and (c) in Figure 4-13 are the strain images and images (d), (e) and (f) are the corresponding modulus images obtained under different pressure levels, i.e. from 0 to 7.3 kPa, 0 to 10.7 kPa, and 0 to 15.5 kPa, respectively. The average strains of the whole background materials were 2.0%, 2.7%, and 4%, respectively. It was found that a relatively larger strain level could improve the contrast of the modulus image.

Figure 4-14 shows the strain and corresponding modulus profiles across the selected horizontal zones of the images (c) and (f) in Figure 4-13, as indicated by the dashed lines. Each value in Figure 4-14 represents the mean of the data within the 0.6-mm wide vertical region and the error bar indicates the standard deviation of these data.

Figure 4-15 shows the modulus images obtained from two independent scan sequences on the same phantom under the approximately same indentation level. Both of the images were obtained under the indentation pressure of 15.5 ± 2.8 kPa. As shown in Figure 4-16, the modulus profiles obtained from the modulus images are identical within the measurement standard deviation (SD). Moreover, the correlation coefficient value of these two modulus images was r = 0.92, indicating a high similarity between the two images. This demonstrated a good reproducibility of the modulus imaging using the ultrasound water indentation system.

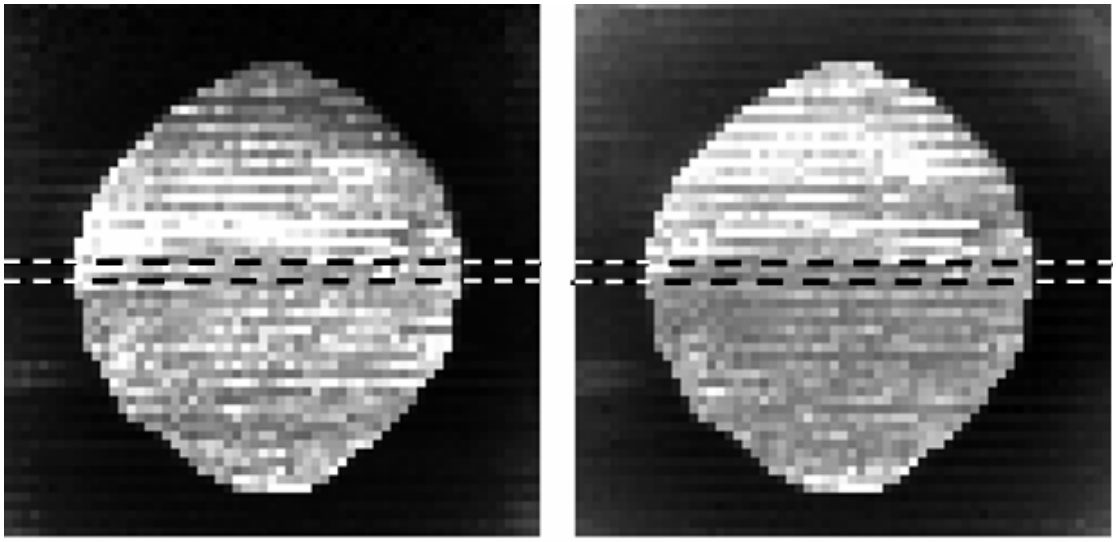

Figure 4-15. The modulus images obtained from two independent scans of the same phantom under the approximately same indentation level. The resemblance of the images demonstrated the reproducibility of the modulus imaging using the ultrasound water indentation system. The dashed rectangles indicated the regions used for the plot of modulus profiles in Figure 4-16.

Figure 4-17 shows the six strain images obtained from the six different phantoms with varying inclusion/background modulus contrast at a pressure level of 14.5 ± 2.2 kPa. Figure 4-18 shows the corresponding modulus images of CP1 to CP6. The modulus contrast was measured by estimating the average modulus of the inclusion and that of the background material. As the scan area was typically 12 mm × 12 mm and the inclusion size was 8 mm, the average modulus of the inclusion was obtained from a region of interest (ROI) of 3 mm × 3 mm at the center of the inclusion and the average modulus of the background was obtained from the average modulus in four ROIs (2 mm × 2 mm) at the four corners of the modulus image. The selection of ROIs was based on the criterion

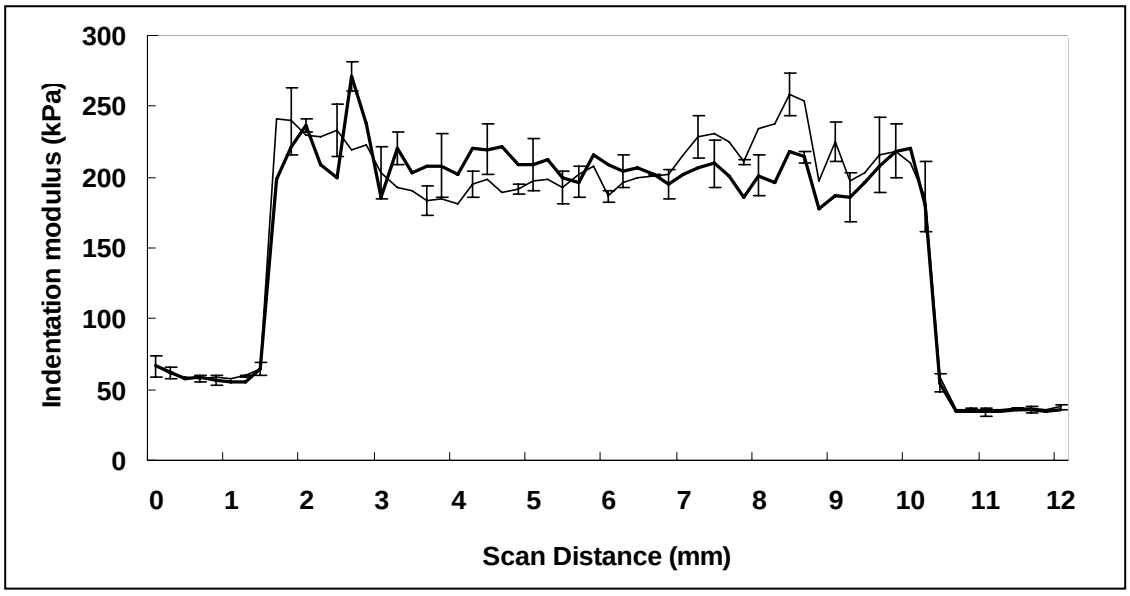

Figure 4-16. Average modulus profile taken from the modulus images of Figure 4-15a (the solid thin line) and Figure 4-15b (the solid thick line). The error bar was plotted once per three points for a clearer view and indicated the modulus variation across the 0.4-mm wide region around the center, which was indicated by the dashed rectangles in Figure 4-15.

that the sites around the connective regions between the stiff and soft materials should not be included. The measured moduli of both inclusion and background materials were compared with their actual values obtained from the uniaxial compression tests. Figure 4-19 shows the relationship between these two sets of modulus. The high correlation coefficient (r = 0.99) indicated a very good agreement between them, though some differences between the absolute values were noted. Figure 4-20 is the correlation between the measured modulus contrast values and those obtained using the uniaxial compression tests. A good correlation was also found with a correlation coefficient ratio r = 0.98.

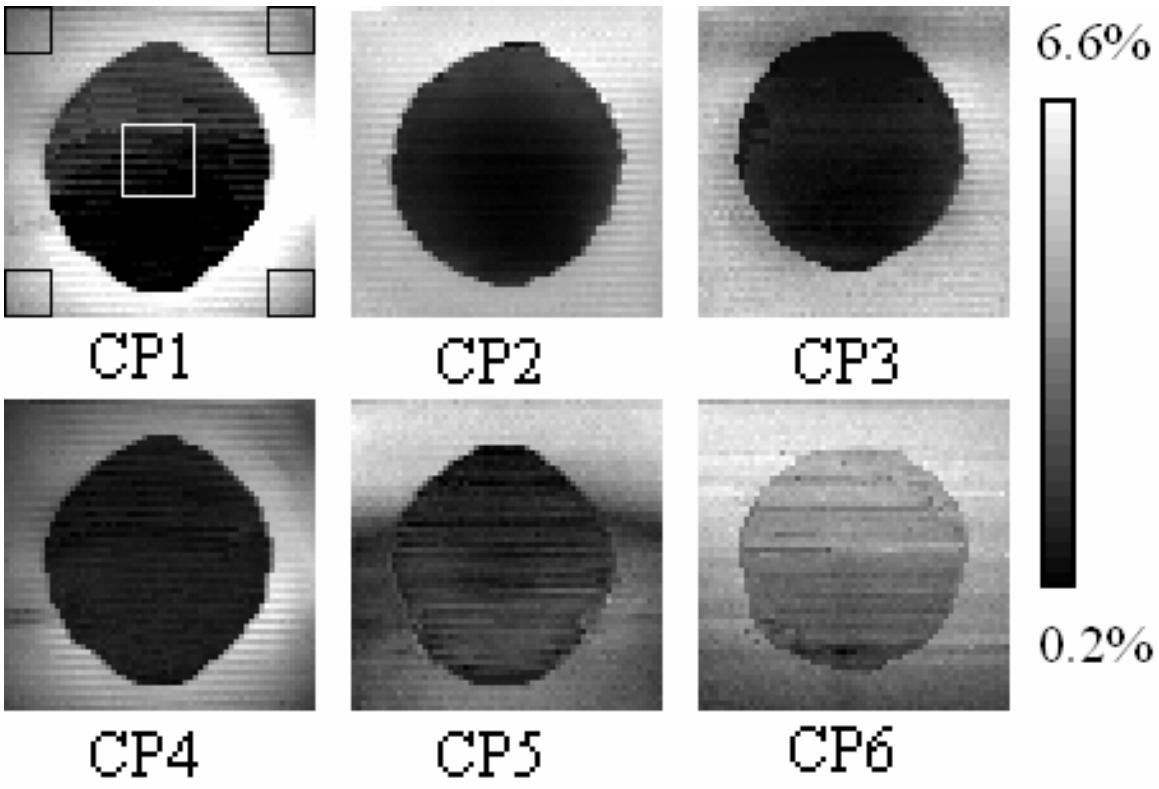

Figure 4-17. Strain images obtained from the six phantoms with different inclusion/background modulus contrast. The pressure level to obtain these results was 14.5 ± 2.2 kPa.

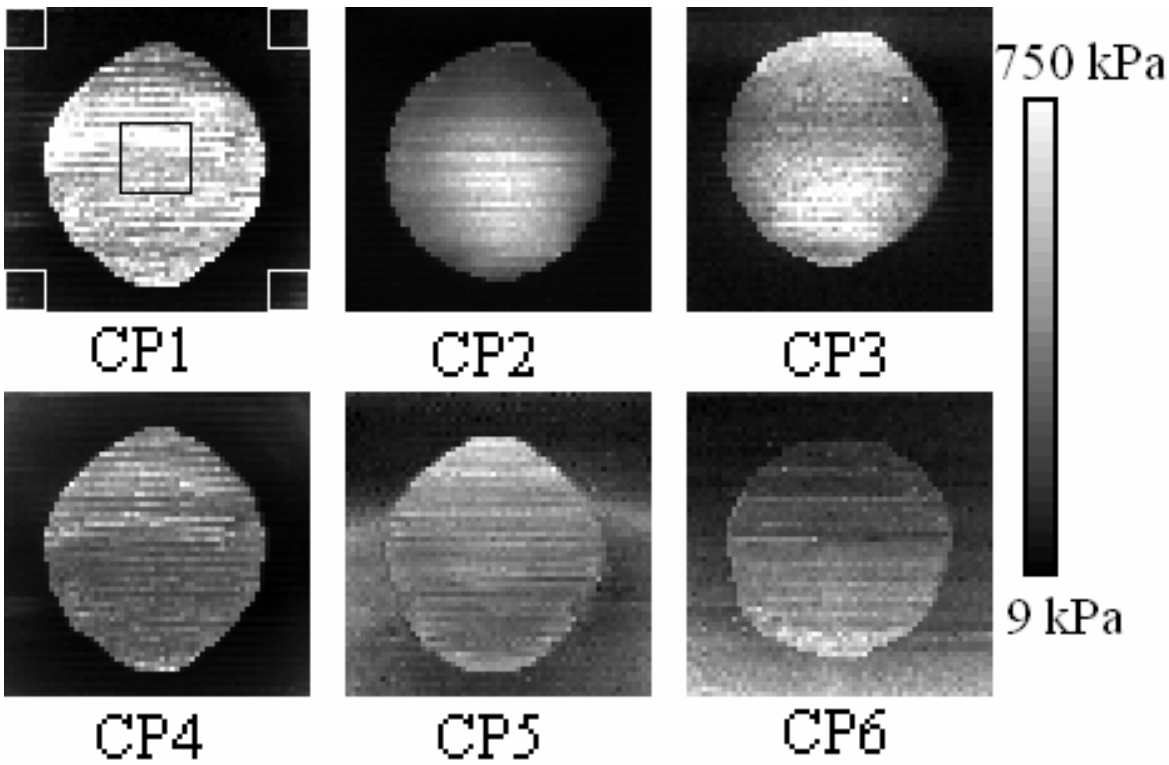

Figure 4-18. Modulus images of phantoms CP1 to CP6 using a water jet pressure level of 14.5 ± 2.2 kPa. The diameter of the cylindrical stiff inclusion was 8 mm and the scanning area was 12 mm × 12 mm. All images are displayed using the same dynamic range. The measured modulus contrast was 9.61, 8.96, 7.71, 3.95, 1.32, 0.10 dB for phantom CP1 to CP6, respectively. The rectangles marked in the center of the inclusion and four corners of background of the modulus image of phantom CP1 indicated the regions used to calculate the modulus of the inclusion and background, respectively.

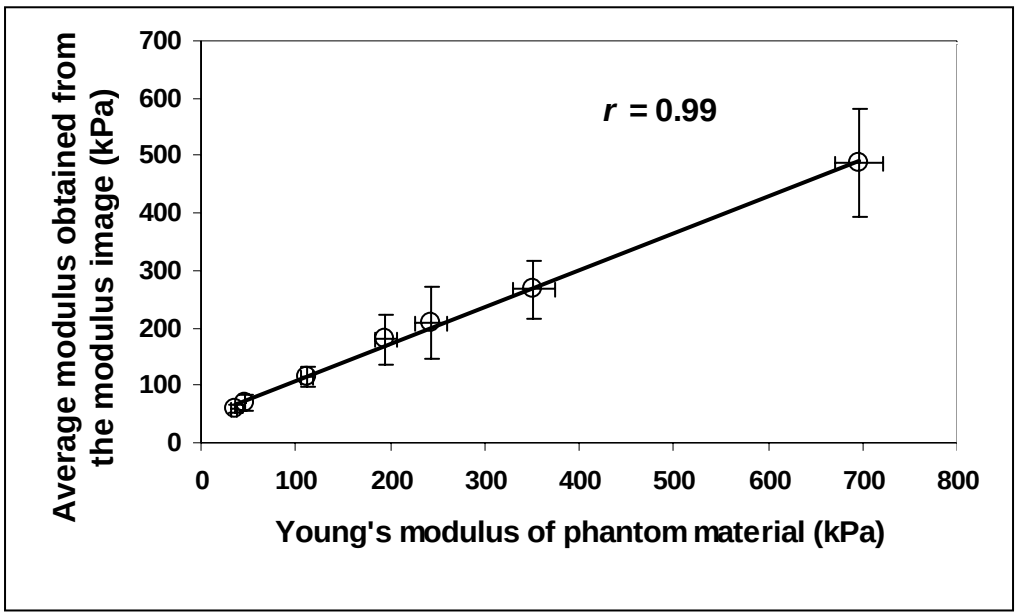

Figure 4-19. The correlation between the moduli of the phantom materials determined using the water jet indentation and those measured using the uniaxial compression. The error bar indicates the standard deviation of the measurements.

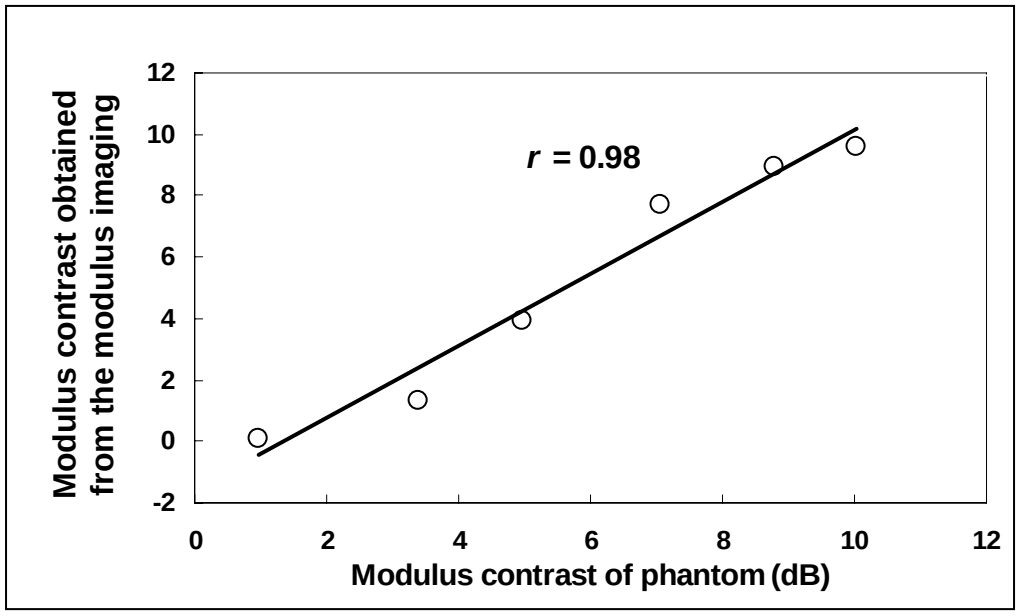

Figure 4-20. The measured modulus contrasts of phantom CP1 to CP6 were compared to the corresponding modulus contrasts obtained from the uniaxial compression test.

4.3 Assessment of Articular Cartilage Degeneration

4.3.1 Stiffness and Thickness of Normal and Digested Articular Cartilage

The bovine patella samples (n = 8) before and after trypsin digestion were assessed by the water jet ultrasound indentation. Figure 4-21 shows a typical curve of the loading and unloading cycles obtained from a test site of one cartilage sample. It was noted that the strain curve followed the pressure curve well, though not so well as the result obtained from the tissue-mimicking phantoms (Figure 4-4a). Since the indentation process was applied very quickly (within 1 s) and the local strain was small (< 1%), the cartilage was assumed as an incompressible elastic solid with no interstitial fluid flow during the indentation. Therefore, the relationship between the applied pressure and the local strain was regarded as the instantaneous response of the sample.

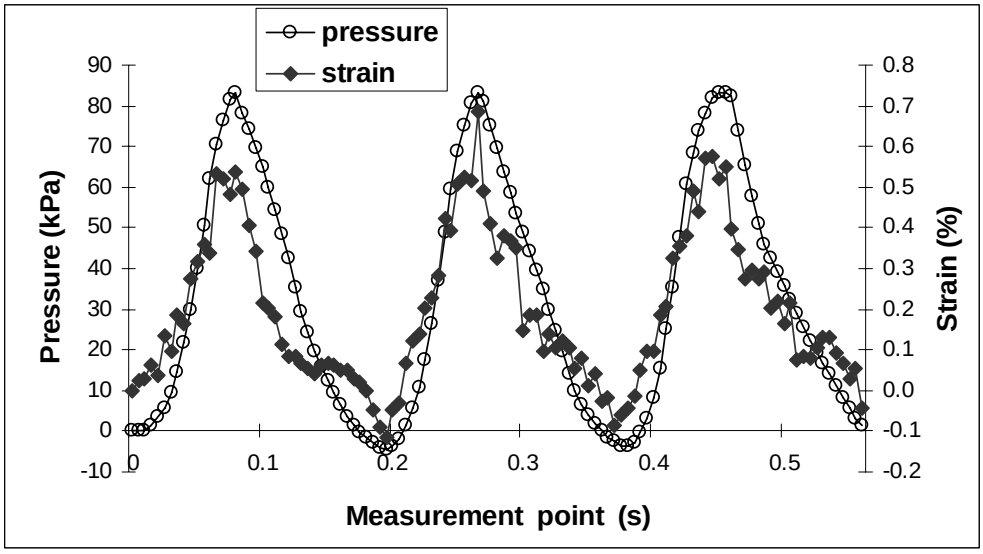

Figure 4-21. A typical curve of the loading and unloading cycles obtained from a test site of one cartilage sample.

The data obtained at the loading phases were used to extract the stiffness ratio of the cartilage. As shown in Figure 4-22, the data were fitted very well with the linear regression (average $R > 0.9$). For the native samples, the stiffness ratio and thickness were 18.83 ± 7.52 MPa and 1.75 ± 0.23 mm, respectively. A stiffness ratio of 7.90 ± 3.37 MPa was found for the degenerated samples, and the corresponding thickness was 1.76 ± 0.24 mm. Figures 4-23 and 4-24 show the boxplots of the stiffness ratio and thickness of the cartilage samples measured before and after the trypsin treatment. It was found that the stiffness ratio significantly decreased after the sample was digested by trypsin ($P < 0.001$, Figure 4-23) while no significant difference was found between the thickness values of the cartilage samples before and after the trypsin treatment ($P = 0.87$, Figure 4-24).

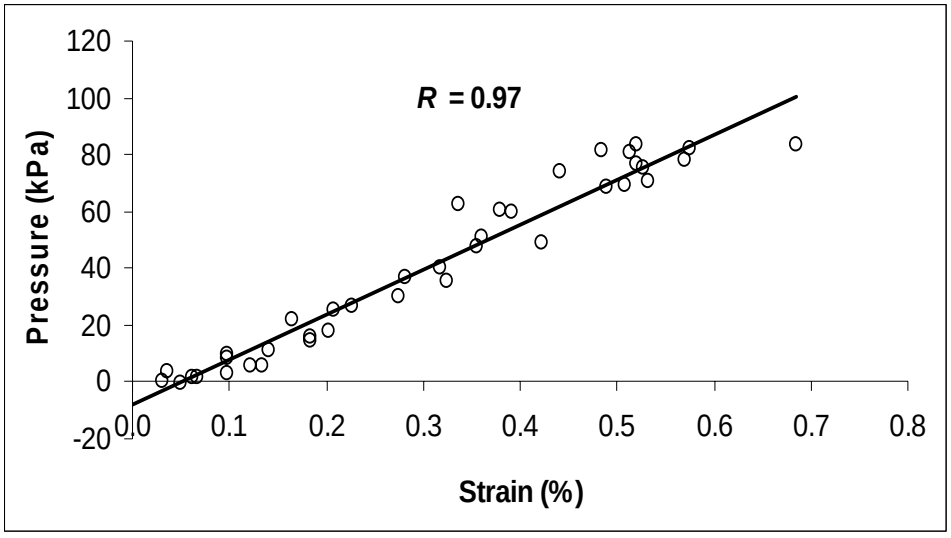

Figure 4-22. The relationship between the pressure and strain which was fitted by a linear regression model.

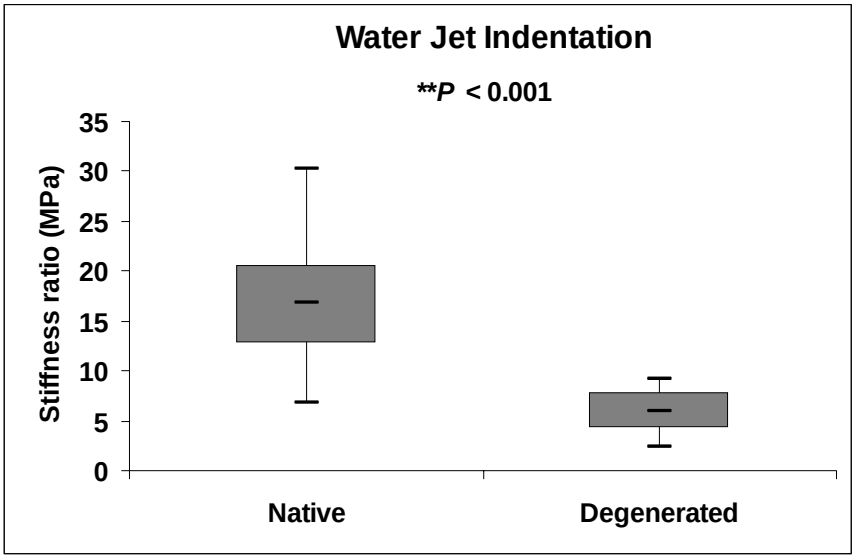

Figure 4-23. Box plot of the stiffness ratio obtained using the ultrasound water jet indentation. Significant difference was found between the stiffness ratios of native and degenerated samples ($P < 0.001$, $n = 20$).

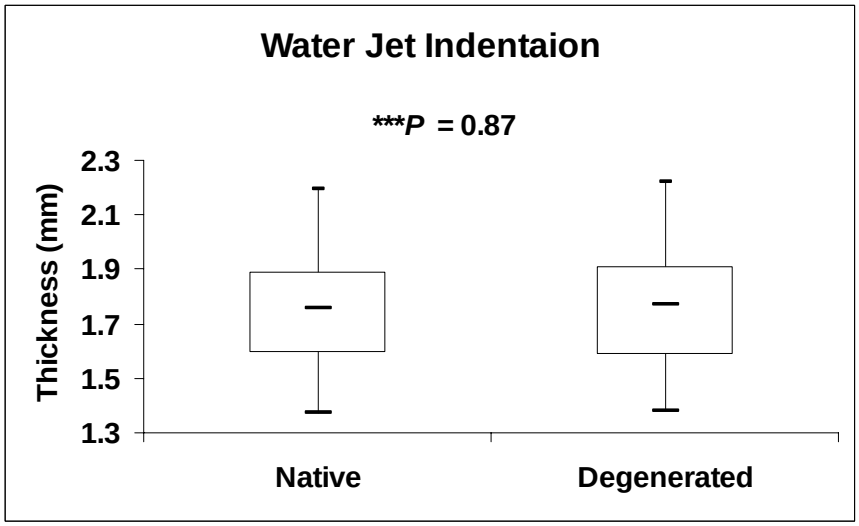

Figure 4-24. Box plot of the thickness obtained using the ultrasound water jet indentation. No significant difference of thickness was found between the samples before and after trypsin digestion ($P = 0.87$, $n = 20$).

The reproducibility of the measurement using the ultrasound water jet indentation system was assessed by the standardized variation of three repeatable measurements of the stiffness ratio and thickness on each test site of four cartilage samples (number of test sites n = 12). The values of sCV were 8.01% for the stiffness ratio measurement and 1.56% for the thickness measurement, indicating a good reproducibility of the ultrasound measurements.

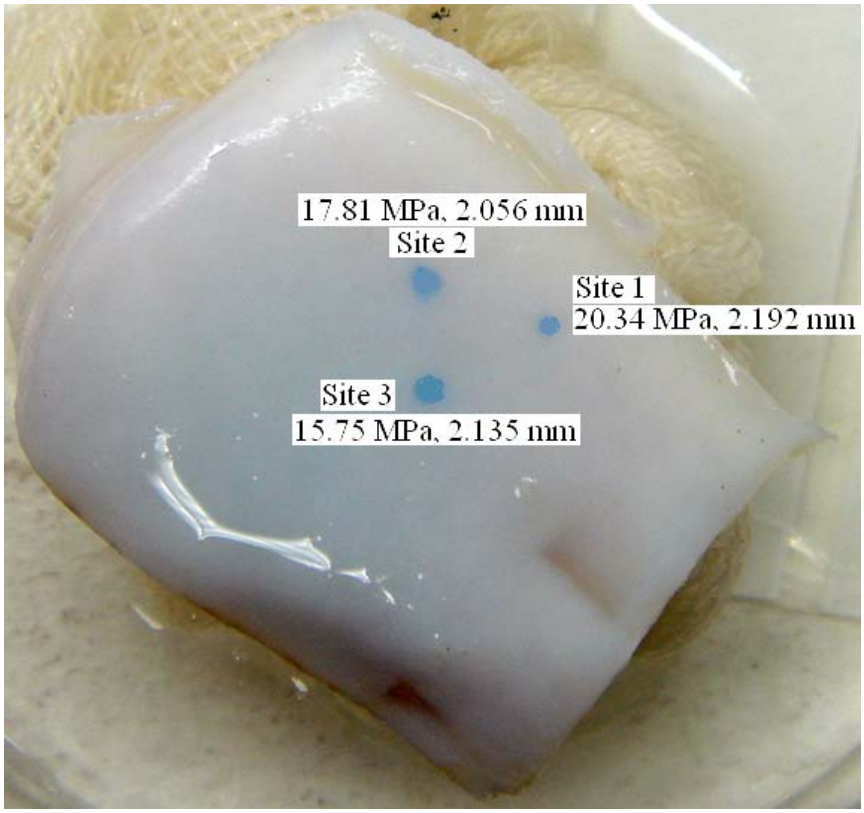

Figure 4-25. A typical sample with varied stiffness ratio and thickness measured using the ultrasound water jet indentation system. The stiffness ratio and thickness of each site (site 1, 2 and 3) were labelled.

It was also found that the stiffness and thickness of the cartilage varied among different test sites. Figure 4-25 shows a typical sample with varied stiffness ratio and thickness measured using the ultrasound water jet indentation system. The site-dependent effect was significant for every cartilage sample ($P < 0.02$ for both stiffness ratio and thickness measurement). It was believed that the novel ultrasound water jet indentation system could map the elastic modulus and thickness of the bulk articular cartilage.

4.3.2 Ultrasound Reflection Measurements

For the ultrasound reflection measurements, the standardized coefficient of variation (sCV) was 1.93% for the peak-to-peak amplitude measurement of all the test sites. Figure 4-26 shows typical A-mode ultrasound signals from the sample before (a) and after the trypsin digestion (b). A significant decrease of 35.64% ± 19.51% of the peak-to-peak amplitude at the interface of water/cartilage surface ($P < 0.001$, $n = 20$) was found after the cartilage sample was treated by the trypsin, however, no significant decrease of the signal amplitude was observed ($P = 0.053$, $n = 20$) at the interface of cartilage/subcondral bone. The decrease of the ultrasound reflection at the cartilage surface indicated that trypsin may have induced not only proteoglycans degradation but also small degradation of collagens.

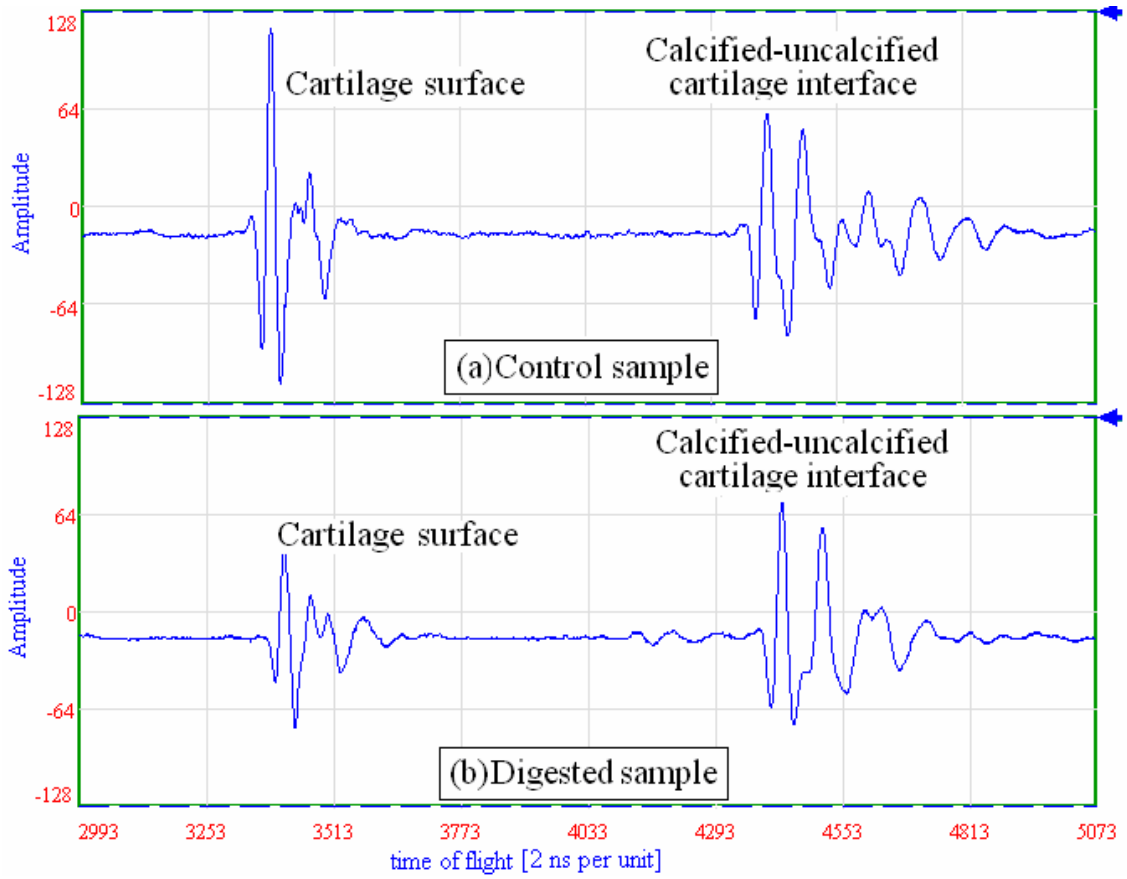

Figure 4-26. Typical A-mode ultrasound signals from (a) the control sample and (b) the digested sample. The first echo indicates the cartilage surface and the second echo indicates the calcified-uncalcified cartilage interface.

4.3.3 Evaluation of the Effect of Repositioning

For the evaluation of the effect of repositioning, it was found that the values of the standardized coefficient of variation were 6.64%, 0.62% and 4.93% for the stiffness ratio, the cartilage thickness and the peak-to-peak amplitude measurements, respectively. The coefficient of variation was small, indicating that the reproducibility of the measurement was good and the effect of repositioning was not significant.

4.3.4 Comparison with Mechanical Indentation

Using the mechanical indentation system, an instantaneous Young's modulus of 1594.2 ± 493.9 kPa was obtained for the native cartilage samples and 471.0 ± 133.9 kPa for the degenerated samples (Figure 4-27). The thickness values obtained from the ultrasound water jet indentation were used in the Hayes' model to derive the instantaneous Young's modulus of cartilage.

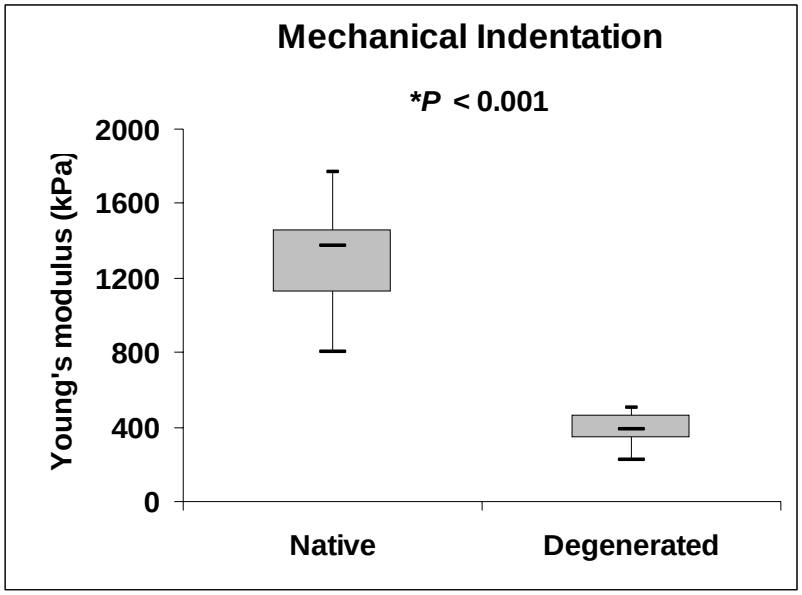

Figure 4-27. Box plot of the Young's modulus obtained using mechanical indentation. It was found that the Young's modulus significantly decreased after trypsin treatment ($P < 0.001$, $n = 20$).

The stiffness ratio obtained using the ultrasound water jet indentation system was found very well correlated with the Young's modulus measured by the mechanical indentation with a correlation ratio $r = 0.87$ ($P < 0.001$, Figure 4-28). We estimated the Young's

modulus of cartilage, E_{eAC}, from the obtained relationship between the stiffness ratio and the instantaneous Young's modulus, E_{ins}, of the cartilage. A Bland-Altman plot (Figure 4-29) was added to give an indication of the size of errors between E_{eAC} and E_{ins}. The mean difference $\bar{d}_{AC}$ was 0 kPa and the standard deviation s_{AC} was 243.1 kPa. From the Bland-Altman plot, most of the differences lied between $\bar{d}_{AC}$ - *2* s_{AC} and $\bar{d}_{AC}$ + *2* s_{AC}. Such a result was good enough for clinical applications (Bland and Altman, 1986).

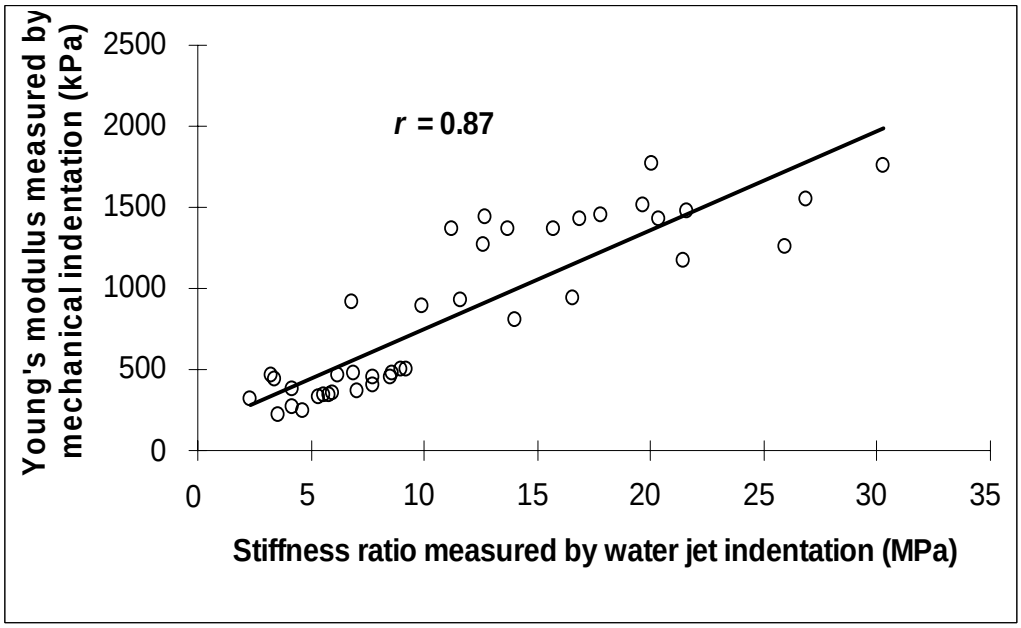

Figure 4-28. Correlation between the stiffness ratio obtained using the ultrasound water jet indentation system and the Young's modulus obtained from the mechanical indentation for both native and degenerated cartilage samples (r = 0.87, P < 0.001).

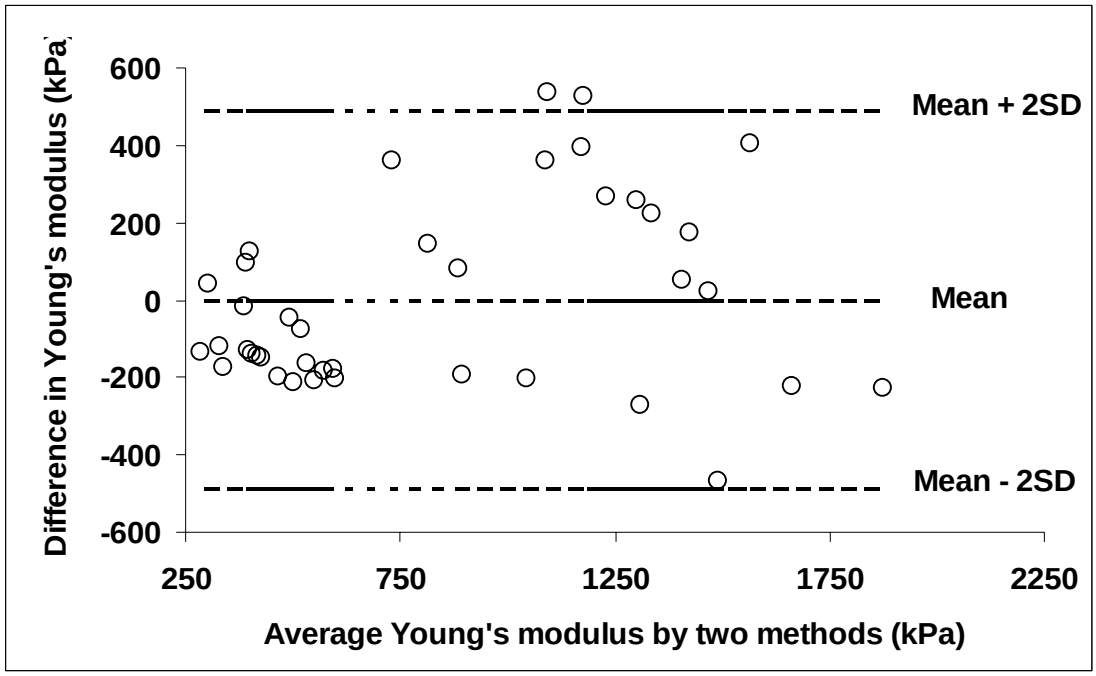

Figure 4-29. Bland-Altman plot to test the agreement between the estimated Young's modulus of cartilage samples by ultrasound water jet indentation and the measured modulus by mechanical indentation.

It was found that the elastic modulus was significantly reduced after the treatment with trypsin, independent of the measurement method used. Stiffness ratio was reduced to 44.3% ± 17.0% ($P < 0.001$, Paired T-test, SPSS) measured with the ultrasound water jet indentation system (Figure 4-23), and the instantaneous Young's modulus decreased to 30.5% ± 7.4% ($P < 0.001$) obtained using the mechanical indentation system (Figure 4-27). The decrease of the mechanical properties was due to the loss of the proteoglycans. Figure 4-30 gives a typical histological presentation of a sample before and after trypsin treatment indicating that most of the proteoglycans were digested after the trypsin

treatment. However, no significant difference was found between the thickness of the samples before and after digestion (P = 0.87, Figure 4-24).

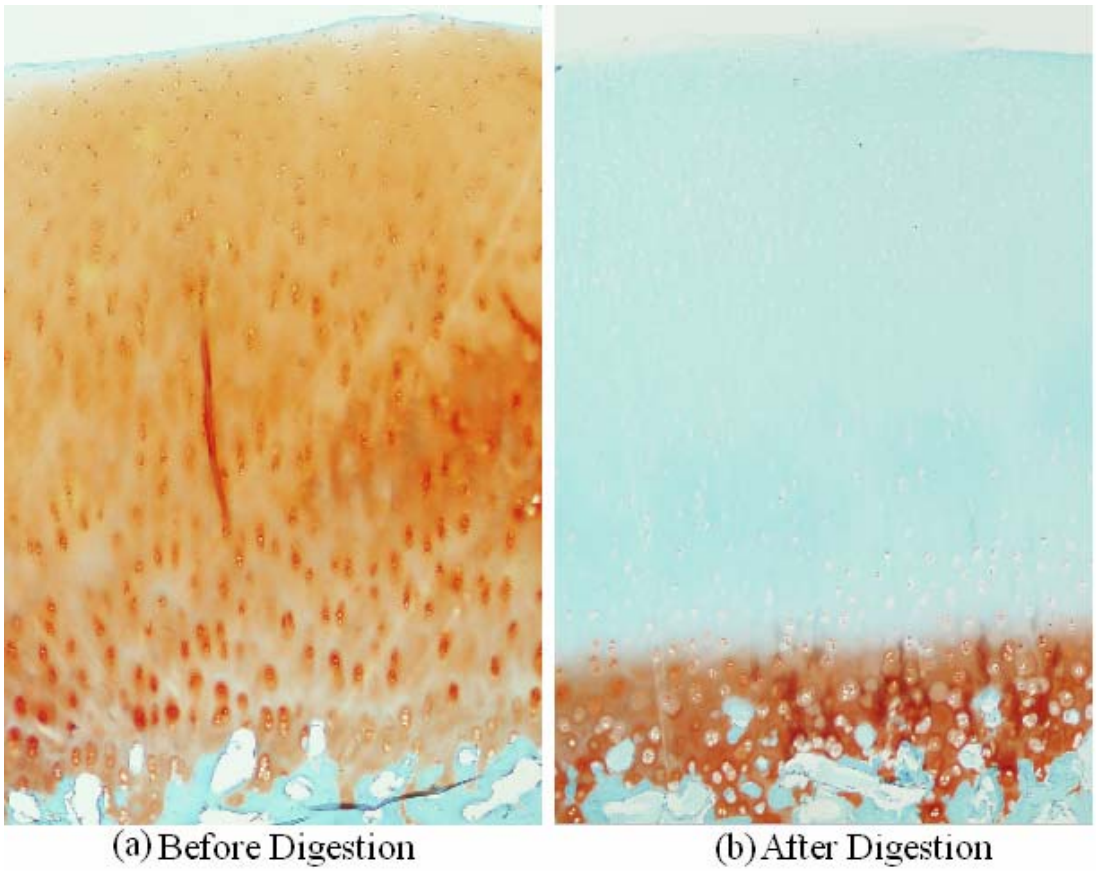

Figure 4-30. Representative micrographs of articular cartilage stained with Safranine O and fast green of a typical sample: (a) native status; (b) after trypsin treatment.

4.4 Assessment of Bone -Tendon Junction Tissues

4.4.1 Stiffness and Thickness of Bone -Tendon Junction Tissues

The stiffness and thickness were assessed for the control samples. Figure 4-31 shows a typical result of a control sample. The values of thickness for patella cartilage, the distal of the cartilage, the junction and the tendon were first measured by the ultrasound water jet indentation when a very small pressure was applied (Figure 4-31a), then the values of stiffness were determined after a loading applied (Figure 4-31b). Table 4-3 lists the values of stiffness, thickness and Young's modulus of the patella cartilage, the distal of patella cartilage, the junction and the tendon of the control samples. All the corresponding values measured from the postoperative samples were listed in Table 4-4.

For the control samples, it was found that there's no significant difference among the four groups and the three harvest time slots (all $P > 0.07$), i.e. the group separation and the sacrificed time do not have significant effects on the material properties of the control samples at 95% significance level. Therefore, the values of all the control samples were averaged (Table 4-5) as the corresponding reference values of each part which would be used to compare with those obtained from the post-operative samples.

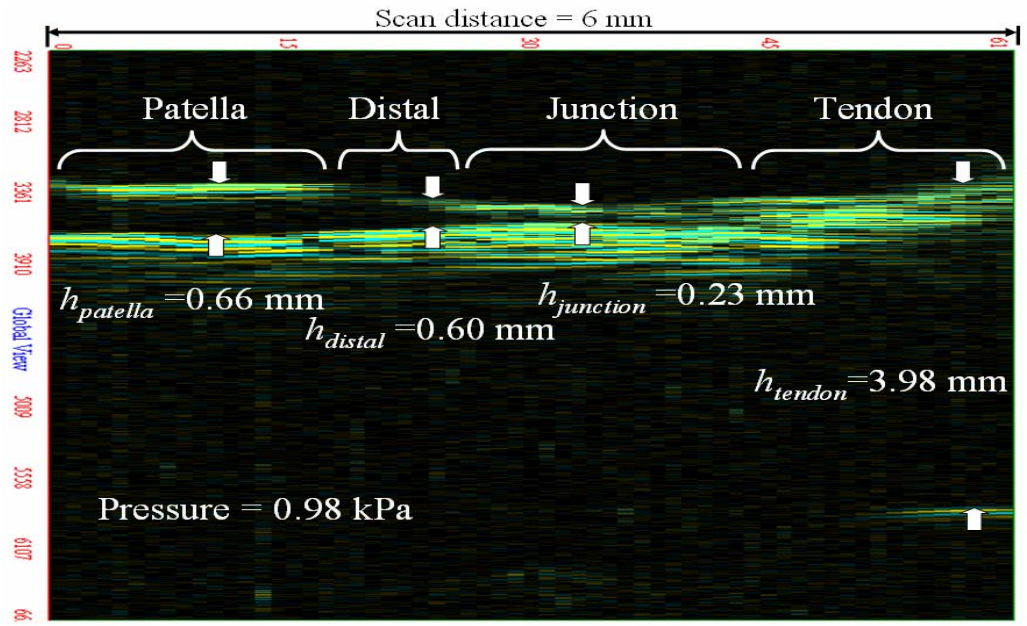

(a)

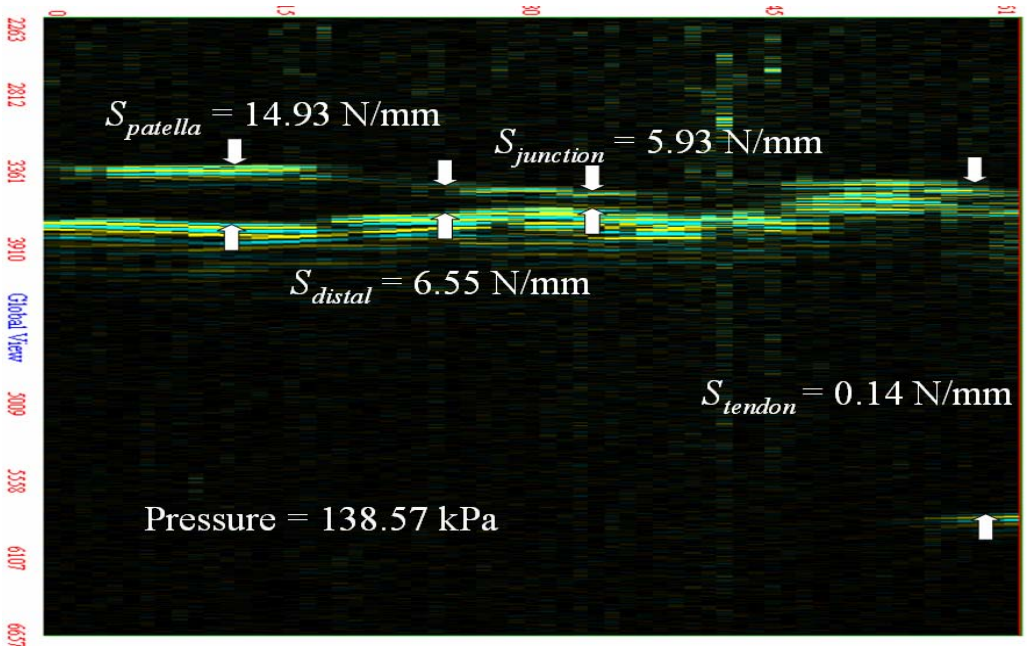

(b)

Figure 4-31. a) The values of thickness for patella cartilage, the distal of the cartilage, the junction and the tendon for a typical control sample; b) the corresponding stiffness of each part.

Table 4-3. The values of stiffness (a), thickness (b) and Young's modulus (c) of each part of the control samples in four groups at three sacrificed times.

(a)		**Stiffness** (N/mm)		
		Week 6	Week 12	Week 18
Group A	Patella Cartilage	8.83 ± 3.96	11.80 ± 2.56	8.65 ± 0.64
	Distal of Patella	5.94 ± 2.39	5.87 ± 3.64	6.03 ± 1.35
	Junction	4.97 ± 1.60	5.01 ± 2.20	4.72 ± 2.69
	Tendon	0.22 ± 0.09	0.24 ± 0.04	0.19 ± 0.05
Group B	Patella Cartilage	10.51 ± 2.58	12.71 ± 2.68	8.99 ± 2.16
	Distal of Patella	6.16 ± 1.80	6.47 ± 1.45	7.89 ± 2.40
	Junction	4.57 ± 0.81	5.76 ± 1.51	6.24 ± 2.33
	Tendon	0.32 ± 0.12	0.24 ± 0.06	0.21 ± 0.10
Group C	Patella Cartilage		11.57 ± 0.93	10.11 ± 2.23
	Distal of Patella		7.29 ± 1.78	7.20 ± 1.43
	Junction		4.16 ± 0.11	5.64 ± 1.61
	Tendon		0.22 ± 0.06	0.23 ± 0.06
Group D	Patella Cartilage		14.19 ± 0.93	10.45 ± 2.27
	Distal of Patella		6.84 ± 2.09	7.52 ± 2.37
	Junction		6.61 ± 0.90	5.95 ± 3.94
	Tendon		0.20 ± 0.05	0.17 ± 0.02

(b)		**Thickness** (mm)		
		Week 6	Week 12	Week 18
Group A	Patella Cartilage	0.56 ± 0.10	0.56 ± 0.16	0.49 ± 0.39
	Distal of Patella	0.36 ± 0.17	0.32 ± 0.08	0.38 ± 0.17
	Junction	0.26 ± 0.04	0.21 ± 0.01	0.37 ± 0.21
	Tendon	3.76 ± 0.45	3.71 ± 0.25	3.58 ± 0.11
Group B	Patella Cartilage	0.55 ± 0.05	0.55 ± 0.20	0.62 ± 0.07
	Distal of Patella	0.35 ± 0.08	0.38 ± 0.14	0.38 ± 0.09
	Junction	0.26 ± 0.07	0.21 ± 0.02	0.22 ± 0.04
	Tendon	2.91 ± 1.12	3.59 ± 0.50	3.76 ± 0.28

Group C	Patella Cartilage	0.68 ± 0.06	0.66 ± 0.07
	Distal of Patella	0.38 ± 0.23	0.52 ± 0.17
	Junction	0.27 ± 0.05	0.27 ± 0.06
	Tendon	3.65 ± 0.33	4.09 ± 0.56
Group D	Patella Cartilage	0.61 ± 0.13	0.60 ± 0.03
	Distal of Patella	0.50 ± 0.14	0.47 ± 0.18
	Junction	0.23 ± 0.01	0.30 ± 0.03
	Tendon	3.86 ± 0.26	4.14 ± 0.26

(c)		**Young's modulus** (kPa)		
		Week 6	Week 12	Week 18
Group A	Patella Cartilage	426.3 ± 222.3	543.5 ± 33.8	363.8 ± 290.3
	Distal of Patella	187.8 ± 134.7	146.1 ± 57.1	192.7 ± 83.6
	Junction	107.1 ± 29.8	89.46 ± 36.1	116.2 ± 32.2
	Tendon	69.1 ± 20.5	76.1 ± 16.5	58.3 ± 15.9
Group B	Patella Cartilage	490.3 ± 148.3	553.1 ± 149.6	478.9 ± 147.3
	Distal of Patella	184.1 ± 65.3	207.9 ± 86.0	241.3 ± 47.3
	Junction	98.8 ± 16.0	98.9 ± 19.5	115.7 ± 47.1
	Tendon	71.5 ± 14.5	71.4 ± 13.1	65.7 ± 26.5
Group C	Patella Cartilage		672.3 ± 105.9	562.9 ± 114.5
	Distal of Patella		217.5 ± 76.4	316.9 ± 125.9
	Junction		95.9 ± 18.3	125.4 ± 34.0
	Tendon		68.5 ± 16.6	79.1 ± 19.4
Group D	Patella Cartilage		724.7 ± 141.8	528.9 ± 88.8
	Distal of Patella		276.1 ± 49.5	278.6 ± 21.9
	Junction		126.7 ± 22.4	143.9 ± 84.0
	Tendon		65.1 ± 19.9	59.9 ± 3.2

Table 4-4. The values of stiffness (a), thickness (b) and Young's modulus (c) of each part of the postoperative samples in four groups at three sacrificed times.

(a)		**Stiffness** (N/mm)		
		Week 6	Week 12	Week 18
Group A	Patella Cartilage	3.27 ± 1.38	5.78 ± 2.25	5.20 ± 0.12
	Junction	0.93 ± 0.15	1.83 ± 1.24	1.79 ± 0.65
	Tendon	0.20 ± 0.09	0.26 ± 0.02	0.23 ± 0.05
Group B	Patella Cartilage	6.75 ± 2.07	5.49 ± 1.67	4.50 ± 2.66
	Junction	1.94 ± 1.03	1.30 ± 0.36	3.87 ± 1.95
	Tendon	0.13 ± 0.06	0.16 ± 0.04	0.20 ± 0.07
Group C	Patella Cartilage		6.15 ± 2.58	8.48 ± 2.83
	Junction		2.31 ± 0.08	5.71 ± 0.96
	Tendon		0.29 ± 0.20	0.24 ± 0.10
Group D	Patella Cartilage		4.25 ± 0.65	9.70 ± 3.09
	Junction		3.41 ± 2.31	4.53 ± 2.07
	Tendon		0.18 ± 0.03	0.29 ± 0.09

(b)		**Thickness** (mm)		
		Week 6	Week 12	Week 18
Group A	Patella Cartilage	0.83 ± 0.11	0.52 ± 0.08	0.60 ± 0.08
	Junction	0.84 ± 0.40	0.56 ± 0.35	0.69 ± 0.15
	Tendon	4.59 ± 1.60	4.27 ± 0.46	3.93 ± 0.77
Group B	Patella Cartilage	0.54 ± 0.04	0.51 ± 0.18	0.59 ± 0.28
	Junction	0.61 ± 0.32	0.68 ± 0.35	0.41 ± 0.07
	Tendon	4.97 ± 0.57	4.68 ± 0.96	4.14 ± 1.61
Group C	Patella Cartilage		0.45 ± 0.21	0.53 ± 0.17
	Junction		0.38 ± 0.02	0.35 ± 0.06
	Tendon		3.42 ± 2.38	3.99 ± 1.41
Group D	Patella Cartilage		0.34 ± 0.09	0.58 ± 0.08
	Junction		0.61 ± 0.52	0.54 ± 0.15
	Tendon		4.65 ± 2.69	2.85 ± 0.53

(c)		**Young's modulus** (kPa)		
		Week 6	Week 12	Week 18
Group A	Patella Cartilage	229.9 ± 97.6	262.3 ± 130.8	264.6 ± 40.5
	Junction	62.0 ± 21.5	63.2 ± 31.1	100.4 ± 28.0
	Tendon	80.8 ± 55.1	93.0 ± 1.3	75.8 ± 15.0
Group B	Patella Cartilage	306.8 ± 91.7	246.2 ± 157.3	197.3 ± 102.4
	Junction	79.1 ± 18.5	68.0 ± 25.6	126.8 ± 46.1
	Tendon	55.6 ± 27.8	62.3 ± 12.2	68.4 ± 24.0
Group C	Patella Cartilage		215.0 ± 104.1	397.6 ± 207.6
	Junction		74.4 ± 6.0	168.4 ± 26.6
	Tendon		58.0 ± 26.3	70.9 ± 16.4
Group D	Patella Cartilage		118.9 ± 14.5	484.4 ± 216.3
	Junction		110.6 ± 17.7	194.5 ± 38.3
	Tendon		65.4 ± 31.6	68.8 ± 7.6

Table 4-5. The average values of stiffness, thickness and Young's modulkus of all the control samples (n = 43).

	Stiffness (N/mm)	**Thickness** (mm)	**Young's modulus** (kPa)
Patella Cartilage	10.48 ± 2.79	0.59 ± 0.14	523.0 ± 172.7
Distal of Patella	6.79 ± 1.94	0.41 ± 0.14	229.3 ± 94.5
Junction	5.43 ± 1.78	0.25 ± 0.07	111.7 ± 33.7
Tendon	0.23 ± 0.08	3.62 ± 0.80	69.5 ± 18.0

To assess the bone-tendon junction healing after the operation, the following comparisons were conducted:

1) The comparison between the control samples and postoperative samples without any postoperative treatment in Group A to find if the tissues were degraded after the operation. Results showed that the thickness values of junction tissue and tendon of the

postoperative samples were significantly larger ($P < 0.005$) than those of the control samples, whereas the thickness of the patella cartilage of the postoperative samples did not significantly differ from that of the control samples ($P = 0.14$). The values of the stiffness of patella cartilage and junction of the postoperative samples were significantly decreased after the operation ($P < 0.005$), while that of the tendon showed no significant difference compared with the control samples ($P = 0.74$). The Young's moduli of both patella cartilage and junction of the control samples were significantly higher than those of the postoperative samples ($P < 0.03$), however, the Young's modulus of tendon had no significant difference between the control and postoperative samples ($P = 0.28$).

2) The postoperative samples in Group A without any postoperative treatment were compared with those in Group B which were treated with LIPUS starting from day 3 to the end of week 6 to find if LIPUS had a significant effect on the healing of the BTJ tissues. It was found that only the stiffness values of junction tissue and tendon of the samples in Group B were significantly different from those in Group A ($P < 0.05$), while other parameters showed no significant difference between Group A and B ($P > 0.2$). The samples in Group B were further analyzed. It was observed that both the stiffness and the Young's modulus of the junction tissues of the samples sacrificed in week 18 were significantly higher than those sacrificed in week 6 and week 12 ($P < 0.03$). The sacrifice time showed no significant effect on the tissue thickness, and the stiffness and Young's modulus of both patellar cartilage and tendon did not change with the healing time ($P > 0.19$).

3) The postoperative samples in Group A without any postoperative treatment were compared with those in Group C which were treated by surface FES starting from begin of week 7 to the end of week 12 to find if surface FES has significant effect on the healing of the BTJ tissues. It was found that the stiffness and Young's modulus of the junction tissue of the samples in Group C were significantly higher than those in Group A ($P < 0.03$), whereas the thickness of the junction tissues significantly decreased ($P = 0.006$). However, the parameters of the patella cartilage and tendon, showed no significant difference between the samples in Groups A and C.

4) The postoperative samples in Group D which were treated with LIPUS starting from day 3 to the end of week 6, followed with surface FES from week 7 to the end of week 12 were compared with Group A, Group B and Group C, respectively to find if there were significant differences within those groups with different treatments. Only significant differences of the stiffness and Young's modulus of junction tissues were found within the samples in these four groups ($P < 0.05$), while all the parameters of both patella cartilage and tendon, showed no significant difference when the samples were treated by different methods ($P > 0.08$). The samples in Groups B and D which were sacrificed at the end of week 12 were also compared since both of them were treated by LIPUS. No significant difference was found ($P > 0.08$) except the Young's modulus of the junction tissue ($P = 0.046$). However, when going into the end of week 18, significant difference was found only between the Young's modulus ($P = 0.024$) of the patella cartilage in Groups B and D.

The assessment of bone-tendon junction tissues is one part of the project collaborated with Prof. Qin L in Department of Orthopaedics & Traumatology at Chinese University of Hong Kong. Therefore, the results obtained using the ultrasound water jet indentation system will be later compared with those results obtained from other tests, such as histological analysis, bone density and bone size measurements, and indirect mechanical properties by the staining intensity measurement of the BTJ healing region, provided by Prof. Qin's group.

CHAPTER V DISCUSSION

5.1 The Noncontact Ultrasound Water Jet Indentation System

A noncontact ultrasound indentation system using water jet has been developed for the assessment of tissue mechanical properties. As a water jet was used as the indenter and simultaneously as the medium for coupling the ultrasound beam, the system could obtain better ultrasound echoes using focused high frequency ultrasound in comparison with the contact ultrasound indentation methods, where rigid indenters or compressors are used to compress the tissue. By using the water jet, it could conduct proper loading on small specimen because of the small dimension of the water jet indenter and obtain tissue deformation and thickness at a microscopic level. In addition, the system was convenient for a C-san to obtain the distribution of tissue material properties for a relatively large area.

In the current noncontact ultrasound water jet indentation system, a 20 MHz focused ultrasound transducer was used, enabling the system to achieve high axial resolution of the measurement because the deformation of phantom under water indentation was determined from ultrasound echoes. For a 20 MHz ultrasound transducer with two cycles of damping period, and an ultrasound speed of 1480 m/s (Krautkramer and Krautkramer 1969), the theoretical axial resolution was approximately 58 μm (Bushong and Archer 1991, Foster et al. 2000). The focal length of the transducer was 19.05 mm, and the diameter of the active element of this transducer was 3.175 mm. Therefore, the f-number

(focal length/crystal diameter) was 6. The theoretical lateral resolution was 0.44 mm (Foster et al. 2000). The resolutions could be further improved by using higher frequency ultrasound, such as 50 MHz ultrasound. According to the numerical simulation results, Righetti et al. (2002, 2003) and Srinivasan et al. (2003) reported that the lateral and axial resolution limits of the strain images obtained using ultrasound were on the order of the sonographic lateral resolution and the ultrasonic wavelength, respectively. In the future study on the small specimen of soft tissues, a focused 50 MHz ultrasound transducer may be used which can achieve a theoretical axial resolution of 35 μm, and lateral resolution of 90 μm (Zheng et al. 2004). With further improvement of the system, it should be feasible to perform nanoindentation (Pethica et al. 1983) using the ultrasound water jet indentation.

In the current experimental setup, daily tap water (24.2 ± 0.2ºC) was used for the water indentation system. The variation of the speed of sound caused by the change of water temperature was 0.05%, i.e. a 0.84 m/s change when a speed of sound 1480 m/s was used (Birks and Green 1991). A water pump will be later used in the system so that the water flow can be better controlled. As the medium for ultrasound propagation was flowing during the water indentation, the effect of the water flow rate on the ultrasound speed had to be investigated. The experiment result showed that the maximal change of the speed of sound through water jet was less than 0.04% (a 0.6 m/s change for a speed of 1480 m/s) when the pressure P_{wp} was changed from 0 to 180 kPa. This suggested that the effect of water flow on ultrasound speed could be neglected during the water indentation with the

pressure up to 180 kPa. The water jet formed from the tap water might contain some air bubbles. The backscatter induced by these bubbles may attenuate the ultrasonic beam that propagates through the water jet. It has been reported that the attenuation caused by the air bubbles increases rapidly as the frequency is increased (Ophir and Parker 1989, Naito et al. 1998, Phillips et al. 1998). However, the effects of the bubbles on the current test could be negligible. According to our measurement, no dramatic attenuation and scattering was caused by the air bubbles in the setup used in this study. For the 20 MHz ultrasonic beam, the ultrasound echo from a steel plate located at the focal zone was attenuated by less than -0.6dB when the water flow was adjusted from 0 to the maximum value used in this study. Such a small attenuation to the echo would not significantly affect the experimental result, as the main information involved in the calculation of the deformation was the flight-time of the echo reflected from the surfaces of the phantom.

During the validation experiments, the ratio between the pressure and the local strain was used as the index of the material stiffness. The stiffness ratio had a good linear relationship (with a correlation coefficient larger than 0.8) with the measured compressive Young's modulus. This demonstrated the feasibility of using the new ultrasound water jet system to quantitatively measure the stiffness of the phantoms. The results of Bland-Altman plot indicated that the results were acceptable for clinical applications (Bland and Altman, 1986).

However, the extraction of the intrinsic mechanical properties from the noncontact water

indentation needs further investigation. As previous investigations have reported (Waters, 1965; Hayes et al. 1972; Mak et al. 1987; Mow et al. 1989; Chicot et al. 1996; Yu and Blanchard, 1996; Sakamoto et al. 1996; Haider and Holmes, 1997), the Young's modulus derived from indentation test using a cylindrical indenter is related to the Poisson's ratio of the material, stress distribution, indentation depth, and tissue thickness. When soft tissues are tested for the measurements of mechanical properties, the non-linearity, viscoelasticity, non-homogeneity, and anisotropy of the tissues should also be carefully considered. In the validation experiment, the silicone phantoms with uniform structures were tested. The applied deformation was within 3% and the loading cycle was completed within 4 s so as to reduce the effects of nonlinearity and viscoelasticity. The slope of the pressure/ local strain curve, defined as the stiffness ratio, was used to correlate with the Young's modulus as we found that the thickness of the phantom was also well correlated with its Young's modulus. Moreover, significant correlation between the stiffness ratio and the Poisson's ratio was also found. These observations are useful for the further investigation on the extraction of intrinsic material parameters from the water jet indentation results. However, there's no suitable equation to precisely describe the relationship between the Young's modulus and the Poisson's ratio, tissue thickness, as well as the applied pressure and the indentation depth using the experimental data yet.

The major cause of the discrepancy between the values of stiffness ratios measured using the water jet indentation method and the Young's moduli measured using the uniaxial compression method may be the simplification in modeling the interaction between the

water jet and the phantom surface since the water jet was assumed to maintain its initial diameter and cylindrical shape after hitting the phantom surface under the small deformation. However, nonlinear behaviours of fluids would occur during the deformation of the phantom, particularly for a large deformation. Therefore, it was suggested that the deformation profile as well as the pressure distribution along the interaction interface should be adjusted with the increase of the water jet pressure.

Different methods have been tried to estimate the stress applied on the tissue surface or measure the deformation profile of the sample under water jet indentation. However, no satisfactory results had been obtained yet. Further investigation will be continued on this issue, such as using pressure sensor films, e.g. the SPI pressure film (SPI Sensor Products Inc., NJ, USA) to map the pressure variation across the interface between the water jet and the sample, or a fibre Bragg grating (FBG) sensor which is a optical sensor commonly used for strain, force and pressure measurements (Ling et al. 2004) to study the stress at the striking point by the water jet. All the efforts will contribute to extract the absolute modulus of the phantom more accurately, taking into account of the effects of the Poisson's ratio, the boundary conditions, and the complicated interaction between the water jet and the tissue surface as well.

5.2 Discussion on Modulus Imaging Obtained from C-scan

The phantom study had proved that the ultrasound water jet indentation system could easily be used for modulus imaging. Water jets have been widely used in the aerospace

industry for several decades as they can provide noncontact coupling of ultrasound from the transducers to the test samples over a distance. Compared with the contact indentation instruments, the ultrasound water jet indentation system appeared to be easily used to conduct C-scans for the sample, under different pressure levels of the water jet. By recording the water pressure and ultrasound signal simultaneously at each indentation site, the local stiffness ratio could be obtained from the indentation force, the local deformation and the original tissue thickness. The effective modulus image could be thus constructed. The phantoms with a symmetrical structure were used for the experiment. The modulus contrast of the phantoms ranged from 0.97 dB to 10.02 dB, and a sharp transition of the modulus was assumed at the inclusion/background interface. As demonstrated in this study, the modulus images obtained using the ultrasound water jet indentation system could be used to effectively identify the stiff inclusions. The modulus contrasts obtained from the modulus image agreed very well with those measured using the uniaxial compression tests. The reproducibility of the modulus imaging was good with the correlation coefficient of 0.92 for the two modulus images obtained by two independent C-scans under the same pressure level. The new system showed its potential to obtain the modulus image of soft tissues with different modulus contrast *in vivo*, when the surface of the tissue is accessible. Obviously, many challenges need to be overcome before this water jet indentation method can be used *in vivo*, such as sterilization, collection of the ejected water or saline, miniaturization of the scanning mechanism, etc.

The spatial resolution of the modulus imaging measurements depended on the cross-sectional size and shape of the indenter, the ultrasound transducer parameters including frequency and beam width, as well as the connectivity between the stiff and soft regions. In this study, a simple geometry of the phantom containing a uniform cylindrical stiff inclusion was used. For the modulus imaging experiment, a sharp transition of the modulus was assumed at the inclusion/background interface. The distance over which the transition occurred from 10% to 90% of the modulus values between a stiff and a soft region was estimated as the spatial resolution of the system (Srinivasan et al. 2004). For the current ultrasound indentation system with a water jet indenter of 1.94 mm in diameter and an ultrasound frequency of 20 MHz, the spatial resolution estimated from the modulus profiles was approximately 0.4 mm. The spatial resolution could be further improved by increasing the ultrasound frequency and reducing the beam width (Foster et al. 2000).

The contrast resolution of the measurement using this ultrasound water jet indentation system is related to its ability to differentiate samples having different values of modulus. If the modulus contrast was defined as the smallest difference of the modulus between two samples that was statistically significant, the contrast could be obtained as 4σ from a statistical analysis using a 95% confidence interval by assuming a normal distribution of the measured modulus values (Bendat and Piersol 1986). For a σ value of 1.68 kPa computed from 35 independent measurements, the contrast resolution was expected to be

6.7 kPa at a 0.05 level of significance. This contrast resolution may satisfy the modulus imaging of most soft tissues (Krouskop et al. 1998).

In the current system, the water jet not only served as the indenter but also as the coupling medium for the propagation of the ultrasound beam. A squirter may produce some disturbing reflections at the contact point following the front surface reflection, even when the water jet was smooth. These reflections could make the ultrasound reflection signal difficult to analyze. It was solved by selecting a suitable diameter of the squirter and focused beam width. Although the C-scan system that we used could be translated at a speed up to 500 $mm \cdot s^{-1}$, the scan speed must be kept at a level that would not induce any water turbulence, which might introduce noise and affect the reliability of the test. Further investigations are required to study the optimized scanning speed for the water jet indentation.

In this study, the phantoms were assumed having linear elastic material properties under the applied small deformation, and both inclusions and backgrounds were assumed to be homogeneous according to their fabrication procedures. However, the modulus images obtained from the water jet indentation method did not appear uniform, particularly when the applied pressure was relatively larger. One possible explanation might be that the inclusion materials around the background-inclusion interface may appear to be softer in comparison with those in the middle portion, as the inclusion materials near the interface were less confined, or confined with softer materials. Thus the middle portion would have

a relatively smaller strain and subsequently a larger modulus could be derived even the applied pressure was the same. This boundary effect would increase with the increase of the applied force or the applied deformation. That is why we noted that the inclusion became more inhomogeneous as the increase of the pressure level. This artifact could be avoided if we had a mechanical model for the whole phantom with the boundary conditions included. Further investigations towards this direction are required in the future.

The stiffness ratio obtained by using the water jet indentation to construct the modulus image may be affected by the Poisson's ratio of the phantom materials, the boundary conditions, and the indentation mechanism. In spite of these effects, a good linear relationship was observed between the stiffness ratio obtained using the current ultrasound water jet indentation system and the Young's modulus of the phantoms obtained by the mechanical indentation. In addition, it is required that the lateral dimension of the sample should be 3 times larger than the indenter diameter according to the indentation model using cylindrical indenters (Hayes et al. 1972, Galbraith and Bryant 1989). This requirement might not always be fulfilled for the real tissues so that the lateral boundary conditions should be considered in the indentation model. Further investigation will be continued to extract the absolute modulus of the phantom more accurately by considering the effects of the Poisson's ratio, the boundary conditions, and the complicated interaction between the water jet and the phantom surface.

5.3 Discussion on the Assessment of Articular Cartilage Degeneration Using Ultrasound Water Jet Indentation System

In this study, the mechanical and acoustic properties of bovine patella articular cartilage were quantified using the noncontact ultrasound water jet indentation system *in situ*. It was suggested that changes in cartilage quality can be determined by stiffness measurement at an early stage (Lane et al. 1979). Therefore, the determination of the mechanical properties of articular cartilage has become of great importance in trauma and joint repair surgery. In comparison to the currently available indentation systems, the ultrasound water jet indentation system offers the advantage of no direct contact between the device and the sample. During the indentation, the deformation induced by the water jet compression was small and within the range of cartilage elastic deformation behaviour. The applied load was very small and no structural tissue damage was observed after the experiment. Thus, it was assumed that the risk of tissue damage during water jet examination was minimized compared with those contact indentation measurements. However, further analysis of cell viability is required to exclude any cellular damage resulting from the water jet application (Bae et al. 2003)

The ultrasound water jet indentation system was proved to be able to effectively assess bovine articular cartilage by measuring both mechanical and acoustic properties. No additional apparatus was needed during the measurements compared with the developed ultrasound indentation instrument by Laasanen et al (2002). The measurements of the stiffness ratio, the thickness, and the peak-to-peak amplitude of the A-mode ultrasound

reflection signal from the articular surface were found highly reproducible with low values of sCV (< 10%), even when the sample was repositioned after the digestion, indicating the system was reliable to be used for the diagnosis of cartilage degeneration. The stiffness ratio and the thickness were found significantly site-dependent, demonstrating that the ultrasound water jet system had the potential to map the variation of the stiffness and thickness of articular cartilage.

The stiffness ratio was well correlated with the instantaneous Young's modulus obtained from the mechanical indentation (r = 0.87), and the estimated Young's moduli derived from the linear relationship between the stiffness ratio and the instantaneous Young's modulus were well within the range of previous studies (Athanasiou et al. 1991, Hale et al. 1993, Setton et al. 1999). A Bland-Altman plot indicated that the estimation was acceptable for clinical applications. Creep tests were tried to obtain the equilibrium response of the cartilage. However, it was found that it was not easy to control the pressure as a constant value due to the fluctuation of the flow rate when it was manual operated. A significant decrease was found in both the stiffness ratio and the peak-to-peak amplitude of the A-mode ultrasound reflection signal from the articular surface between the intact samples and those treated by trypsin. Differences between the intact and digested cartilage were found to be quite similar by both ultrasound water jet indentation (Figure 4-23) and mechanical indentation (Figure 4-27). The decrease of the mechanical properties may be caused by the PG content reduction induced by trypsin treatment (Qin et al. 2002). The depth of PG degradation was validated by histological

measurement. More studies will be conducted for the investigation on the relationship between the histological imaging quantification and the ultrasound detection of the mechanical properties of articular cartilage. The amplitude of the echo signal from the articular surface is related to the ratio of acoustic impedance of cartilage and water. In addition, the surface roughness controls the acoustic scattering and, thereby, affects the amplitude of the reflected signal (Adler et al. 1992). After the trypsin treatment, the articular surface looked normal without any fibrillation or other macroscopical signs of degradation. However, a significant decrease of the amplitude of the echo signal from the articular surface was found, indicating that trypsin might have not only digested PG contents, but also caused slight degradation of collagens.

It is well known that articular cartilage will swell when the concentration of the external bathing solution decreases. The swelling is caused by the change of the Donnon osmotic pressure (Donnon 1924, Mow and Hayes 1997). In our test on the articular cartilage, tap water (nearly 0 M NaCl) was used to eject a water jet as the indenter to deform the cartilage after it was taken away from the normal saline solution (0.15 M NaCl). As reported by Zheng et al. (2003), the maximal swelling strain of an intact cartilage sample was less than 0.1% within an average swelling duration of 302 seconds when the concentration of the bathing solution was changed from 0.15 M NaCl to 0.015 M NaCl. During the ultrasound water jet indentation test, the cartilage sample was scanned by the water jet under a very low constant pressure for 15 minutes before it was deformed. The scan duration was long enough to allow the cartilage to fulfil the transient swelling

behaviour when the concentration of its bathing solution was changed from 0.15 M NaCl to the tap water, and the strain caused by swelling during the indentation process was small enough to be neglected. However, it is better to keep the sample in its physiological conditions to maintain its material properties. Therefore, normal saline solution will be used instead of tap water when a medical pump is employed in the system to eject a water jet as an indenter.

One of the main sources of error in indentation measurements is the imperfect contact between the indenter and the articular cartilage. Since a water jet was used as the indenter, the perpendicularity between the ultrasound beam and the cartilage should be ensured to minimize the error. In our measurements, the lateral lower quarter of bovine patella cartilage was fixed on a rigid platform for the indentation and acoustic evaluation. The test sites were carefully selected by moving the transducer and scanning across the cartilage to find those points with maximal echo amplitude reflected from both the water/cartilage interface and the cartilage/subchondral bone interface. Such a selection criterion ensured the perpendicularity between the ultrasound beam and the cartilage. In addition, to achieve a reliable test, the sample was fixed by two clamps to avoid slipping during the indentation. However, even when slipping was successfully prevented, stress concentration may be developed in the region of clamp which may affect the boundary condition of the indentation. This effect was reduced by keeping the test sites far away enough (at least 5 times the diameter of the indenter, i.e. > 1 cm) from those clamping regions.

Cartilage thickness is an essential clinical parameter and necessary for correct measurement of tissue modulus. In this study, the tissue thickness was calculated using a predetermined speed of sound, which was assumed as a constant. However, early research work has reported a variation of speed of sound between different measurement sites and degenerative states (Patil et al. 2004, Toyras et al. 2003). The speed of sound is slightly lower in OA cartilage than in normal cartilage (Toyras et al. 2003). Digestion of PGs may reduce the speed of sound in cartilage as well (Suh et al. 2001). According to an earlier study (Toyras et al. 2003), the use of a predefined speed of sound, 1636 m/s, may induce an error of (mean ± SD) 1.5 ± 1.4% for the measurement of cartilage thickness, which may further cause an error of the stiffness ratio of 0.4 ± 0.4%. The moderate error induced by the variation of the speed of sound in the estimation of thickness and stiffness ratio may be clinically acceptable. Suh et al. (2001) presented an *in situ* calibration method enabling the measurement of tissue thickness, stiffness and speed of sound. However, the apparent complexity of the instrumentation may limit clinical applicability of this calibration method.

Accuracy of deformation measurement depends rather on sampling rate of the A/D converter than on the ultrasound frequency. With the 500 MHz A/D converter we used, a resolution of 2 ns, i.e. 1.6 μm, could be reached. Such a resolution is adequate for the determination of cartilage deformation during indentation. Higher frequency (e.g. 50 MHz) ultrasound transducers would enable a higher axial resolution, and thereby improve resolution of thickness measurements. Utilizing a high frequency ultrasound transducer in

the ultrasound water jet indentation system may also help to measure the layered material properties of articular cartilage without damaging its biomechanical integrity, for the analysis of zonal variation in articular cartilage biomechanical properties (Qin et al. 2002). This will potentially enable the system to identify the grade of degeneration of the cartilage.

The ultrasound water jet indentation system could be easily used for the A-mode reflection measurement. The condition of the cartilage sample could be differentiated from the change of the peak-to-peak amplitude of the A-mode echo signals reflected from the articular surface. Recent studies on the ultrasonic evaluation of trabecular bone quality have suggested that ultrasound backscatter may be suitable for the characterization of bone density, structure ad stiffness (Wear 1999, Wear et al. 2000, Roux et al. 2001, Chaffai et al. 2002). Changes in subchondral bone, related to early osteoarthritis (Radin et al. 1970), could therefore be diagnosed with the ultrasound techniques (Saied et al. 1997). In addition to the A-mode measurement, the ultrasound water jet indentation is capable of performing scanning to obtain B-mode ultrasound images which would provide additional, visual and quantitative information on the cartilage and subchondral bone structure and composition. However, to obtain a deeper insight into the acoustic properties of articular cartilage, it is necessary to develop a theoretical model which describes satisfactorily the behaviour of ultrasound in cartilage.

Based on the present results, it is concluded that the ultrasound water jet indentation system is capable of quantitative evaluation of both mechanical and acoustical properties of native and degenerated articular cartilage. Compared to other ultrasound indentation devices used to assess cartilage, this new system appears to be able to minimize the risk of surface damage to the cartilage during mechanical loading therefore provides a nondestructive way to measure the cartilage degeneration. However, the system needs to be further improved before it is clinically used to assess the cartilage degeneration.

5.4 Discussion on the Assessment of Bone -Tendon Junction Tissues Using Ultrasound Water Jet Indentation System

Bone-Tendon Junction (BTJ) is a unique structure composed of a transitional fibrocartilage zone, characterized by calcified fibrocartilage connecting to the bone and noncalcified fibrocartilage connecting to the tendon. This unique structure is thought to have material property intermediate between that of bone and tendon, providing a gradual transition in stiffness, which diminishes stress concentration, and tearing or shearing at the interface (Woo et al. 1988). Many traumas may result in patella fractures, in which transverse fractures are most common and usually occur in the middle or lower third of the patella. After a standardized partial patellectomy, the reestablishment of BTJ is needed. However, BTJ healing is slow due to the poor regenerative capacity of the fibrocartilage zone between bone and tendon, poor alignment of patella tendon scar tissue and bone loss of the patella at the BTJ healing interface (Qin et al. 1999). Biophysical approaches, such as low intensity pulsed ultrasound (LIPUS) and functional electrical

stimulation (FES) have been used to accelerate the healing process of BTJ. However, the effects of these approaches on the BTJ healing process need to be verified.

A partial patellectomy model has been established by Qin et al. (2006) in rabbits. Since the BTJ structures of the rabbits are very small, it's difficult to find an appropriate method to quantitatively measure the mechanical properties of the tissues. In this study, the ultrasound water jet indentation system provided a unique way to assess stiffness and thickness of the bone-tendon junction tissues after partial patellectomy. The control samples without partial patellectomy were assessed as a reference, and the postoperative samples with and without LIPUS and FES treatments were measured. After scanning across the BTJ tissues using a very small pressure, the tissue thickness could be calculated using the flight of time of ultrasound; the stiffness of each part of tissues, i.e. the patella cartilage, the junction tissue, and the tendon could be obtained after the sample was scanned along the identical line using a higher pressure. The Young's modulus could be derived from the relationship between the stiffness ratio and the instantaneous Young's modulus obtained from the study on the bovine articular cartilage. The values of the stiffness, thickness and Young's modulus were compared between the control samples and the postoperative samples without or with different treatments.

The comparison between the control samples and postoperative samples without any treatment showed that, after the partial patellectomy, the thickness of the junction and tendon were significantly increased, and the stiffness and Young's modulus of both the

patella cartilage and junction were significantly decreased. The decrease of the mechanical properties of the patellar articular cartilage may result from a decreased PG content in the remaining patellar articular cartilage (Leung et al. 1999). It was reported that no functional fibrocartilage zone was re-established at the healing BTJ even after 24 weeks (Wong et al. 2004). The inflammatory response during the initial healing phase and the postoperative development of metaplasia in the scar tissue next to the healing interface may cause the increase of the tissue thickness and the decrease of the mechanical properties of the junction.

Low intensity pulsed ultrasound (LIPUS) is known to stimulate tissue regeneration (Barnett et al. 1997). Ultrasound appears to be specifically beneficial by accelerating the inflammatory response during the initial healing phase (*ter* Haar 1999). In experimental and clinical situations, LIPUS has been successfully proven to stimulate fracture healing and bone growth (Pilla et al. 1990, Yang et al. 1996, Mayr et al. 2001). *In vitro*, LIPUS has been demonstrated to influence the expression of cartilage-specific matrix proteins and growth factors in cell cultures from chondrocytes, fibroblasts and osteoblasts (Parvizi et al. 1999). In our study, the effect of LIPUS on the healing of BTJ was assessed by comparing the postoperative samples with and without LIPUS treatment. Results showed that the stiffness of junction tissue and tendon of the samples with LIPUS treatment was significantly higher than that of the samples without the treatment. Furthermore, the stiffness and Young's modulus of the junction tissues of the samples with LIPUS treatment were significantly increased at week 18 than those in week 6 and week 12.

These findings may agree with those reported by Qin et al. in 2006 to a certain degree and indicate that LIPUS may enhance the regeneration of a fibrocartilage layer. However, the results should be verified with histological analysis.

In order to facilitate early functional recovery of immobilized musculoskeletal tissues, functional electrical stimulation (FES) has been used as an effective approach to decrease muscle atrophy or prevent tendon atrophy, bone loss or cartilage degeneration of the knee join in immobilization or paralyzed conditions during or after immobilization, by inducing tensile mechanical loading via surface FES on quadriceps muscles, in both animal experiments and clinical settings (Burr et al. 1984, Bedell et al. 1996, Qin et al. 1997, Belanger et al. 2000). The beneficial effects of a progressive exercise program or FES induced mechanical stimuli have been subjected to numerous experimental and clinical studies. The results of these studies have showed that FES has beneficial effects not only on the acceleration of healing in tissues by enhancing proliferation and migration of fibroblasts as well as stimulating collagen synthesis, but also on recovery of other associated musculoskeletal tissues, including bone and joint cartilage secondary to the injured tissues (Burr et al. 1984, Bedell et al. 1996, Qin et al. 1997, Belanger et al. 2000). In this study, the effects of FES on the healing of BTJ structures were monitored. It was found that, compared with the postoperative samples without any treatment, the junctions of the samples in FES group had higher stiffness and Young's modulus, and lower tissue thickness, indicating the formation of a fibrocartilage layer in the junction. This agreed with the results reported by Wong et al. (2003), which demonstrated that, cartilage from

the articular cut surface would extend into the healing interface, and later form an area of fibrocartilage with densely packed collagen fibers aligned along the direction of force, containing proteoglycans.

By comparing the mechanical properties and thickness of the BTJ structures in four groups with different treatments, it was found that both LIPUS and FES had beneficial effects for enhancing BTJ healing. However, this is only a preliminary study using ultrasound water jet indentation system to assess the BTJ structures. All the findings and conclusions should be verified by histological analysis and explained from the biological view.

CHAPTER VI CONCLUSIONS AND FUTURE STUDIES

6.1 Conclusions

The development of a noncontact ultrasound water jet indentation system has been reported in this thesis. The new system consisted of a focused high-frequency ultrasound transducer, a water ejector, a pressure sensor and a three-dimensional translating device. The high frequency ultrasound was coupled with a water jet which served as an indenter at the same time. Such a unique configuration enabled the system to perform noncontact indentation on samples and to achieve a high resolution in the measurement of deformation and tissue thickness. A software system was developed for the control of the 3D translating device, data collection, and signal processing and analysis in real time during the indentation process.

The ultrasound water jet indentation system was first validated using phantom studies. Tissue mimicking phantoms with varied stiffness were used in the validation experiment. The new system could quantitatively measure the stiffness of the phantoms, which used the defined “stiffness ratio” as an indicator. The values of stiffness ratio correlated well with the values of Young’s modulus obtained from the uniaxial compression test and the measurement results were proven clinically acceptable. This indicated that, with further improvement of the system and better understanding about the water jet-tissue interaction, the ultrasound water jet indentation approach could be potentially used to quantitatively assess the stiffness of body tissues for clinical diagnosis, such as skin cancer, burn status,

cornea condition, blood vessel stiffening, articular cartilage degeneration, etc. It could also be employed to perform indentation on small specimens in a microscopic level for tissue and material characterization for small animal tissues, bioengineered tissues, semiconductor materials, thin films, and so on, where nanoindentation is widely used.

Besides the ability to quantitatively measure the mechanical properties of uniform phantoms, another advantage of the ultrasound water jet indentation system was demonstrated using the phantoms fabricated with stiffer inclusions. Results proved that the system was able to map the distribution of the compressive mechanical properties of the phantoms by applying ultrasound C-san sequences with different water pressures. The modulus contrasts obtained from the modulus images correlated well with those obtained from the compression test, and a high spatial resolution was achieved. It is expected that the ultrasound water jet indentation approach could be potentially used to image the modulus distribution of body tissues for clinical assessment and diagnosis, including skin tumor formation, tissue scarring, articular cartilage degeneration (together with arthroscopy), etc. For these potential applications, clinically used sterilized saline pump ccould be used to provide water jet and proper mechanisms should be developed to collect the ejected saline.

Since the ultrasound water jet indentation system could quantitatively measure the mechanical properties of tissues at a microscopic level, it was applied to assess the degeneration of articular cartilage. Besides the diagnosis of stiffness ratio as well as

measuring tissue thickness, the system could perform the acoustical assessment using the ultrasound reflection measurement without any additional apparatus. Both the decrease of stiffness ratio and the peak-to-peak amplitude of the A-mode ultrasound echo reflected from articular surface could be used as indicators for cartilage degeneration. Further more, the noncontact way of indentation performed by water jet minimized the risk of tissue damage compared with those contact indentation measurements. As the first instrumentation with these qualities, it may provide significant advantages in the early clinical diagnosis of osteoarthritis as well as in monitoring cartilage regeneration after surgical repair.

As a preliminary study, the ultrasound water jet indentation system was used to monitor the healing of bone-tendon junction tissues after a partial patellectomy in a rabbit model. The irregular shape and small size of the rabbit BTJ structures make it difficult to perform compressive measurement *in situ*. The ultrasound water jet indentation system provided a unique manner to perform indentation on the BTJ tissues. The findings were reasonable according to the previous reports, although a comprehensive explanation and validation should be provided.

This work provides an original contribution to the research in biomechanics. A novel and unique experimental technique had been developed which offers several advantages for the measurement and imaging both the mechanical and acoustical properties of soft tissues, especially for thin layer of tissues with fine structures simultaneously and

conveniently. The system also offers the advantage of no direct contact between the device and the sample thus minimizes the risk of tissue damage during water jet examination compared with those contact indentation measurements.

6.2 Future Studies

Besides the future efforts mentioned in above sections for further improvement of the present work, several additional tasks should be performed in the future to improve the currently developed water jet indentation system with more advanced performances for the measurement of mechanical and acoustic properties of soft tissues and various biomaterials.

The first task is to develop a portable ultrasound water jet indentation probe for *in vivo* measurement of living tissues, especially for articular cartilage. As described in the methodology, the samples were immersed in a water bath during the experiment. This water bath is not a must for the system. The ultrasound water jet indentation can be performed only with the water jet, which provides a load onto the sample and also a coupling medium for ultrasound beam to reach the sample. Therefore, we can design a hand-held probe with an ultrasound transducer and water ejecting mechanism to perform ultrasound water jet indentation for the body tissues at different parts, without the need of a water tank. The configuration of the probe may be designed as shown in Figure 6-1. When it is applied for *in vivo* tests on body tissues, we need to avoid the spattering of the water and to collect the ejected water. A clinically used sterilized saline pump could be

used to provide fluid jet with high fluid pressure. Proper mechanisms should be designed and used to collect the ejected saline. A focused ultrasound transducer with higher frequency (e.g. 50 MHz) can be utilized to achieve better resolutions for the measurement of tissue thickness and deformation. Currently the ultrasound transducer was attached on a three-dimensional translating device. It helps the transducer easily to perform 1-D and 2-D scannings on the samples; however, it does not allow the rotation of the transducer. Therefore, together with the development of the hand-held water jet indentation probe, a support system consisting of robot arms which allow fine adjustment of the probe position and orientation will also be developed. The support system will help the water jet indentation system to achieve more reliable and accurate measurements of both mechanical and acoustical properties of the samples.

The second task is to model the interaction between the water jet and the sample. In present study, the deformation profile of the sample under water jet indentation was assumed as flat and the initial area of the contact interface was used to calculate the pressure applied on the sample surface. The nonlinear behaviours of fluids during the indentation should be carefully studied through experimental and theoretical approaches. The reaction force at the tissue surface may be dependent on the flow rate and the distance between the water jet head and the sample surface. Hence, the flow rate at the water jet head and the actual force acting on the tissue surface can be determined based on the measurable water flow rate and the pressure measured within the water pipe. Moreover, since some water was observed reflected from the tissue surface during the

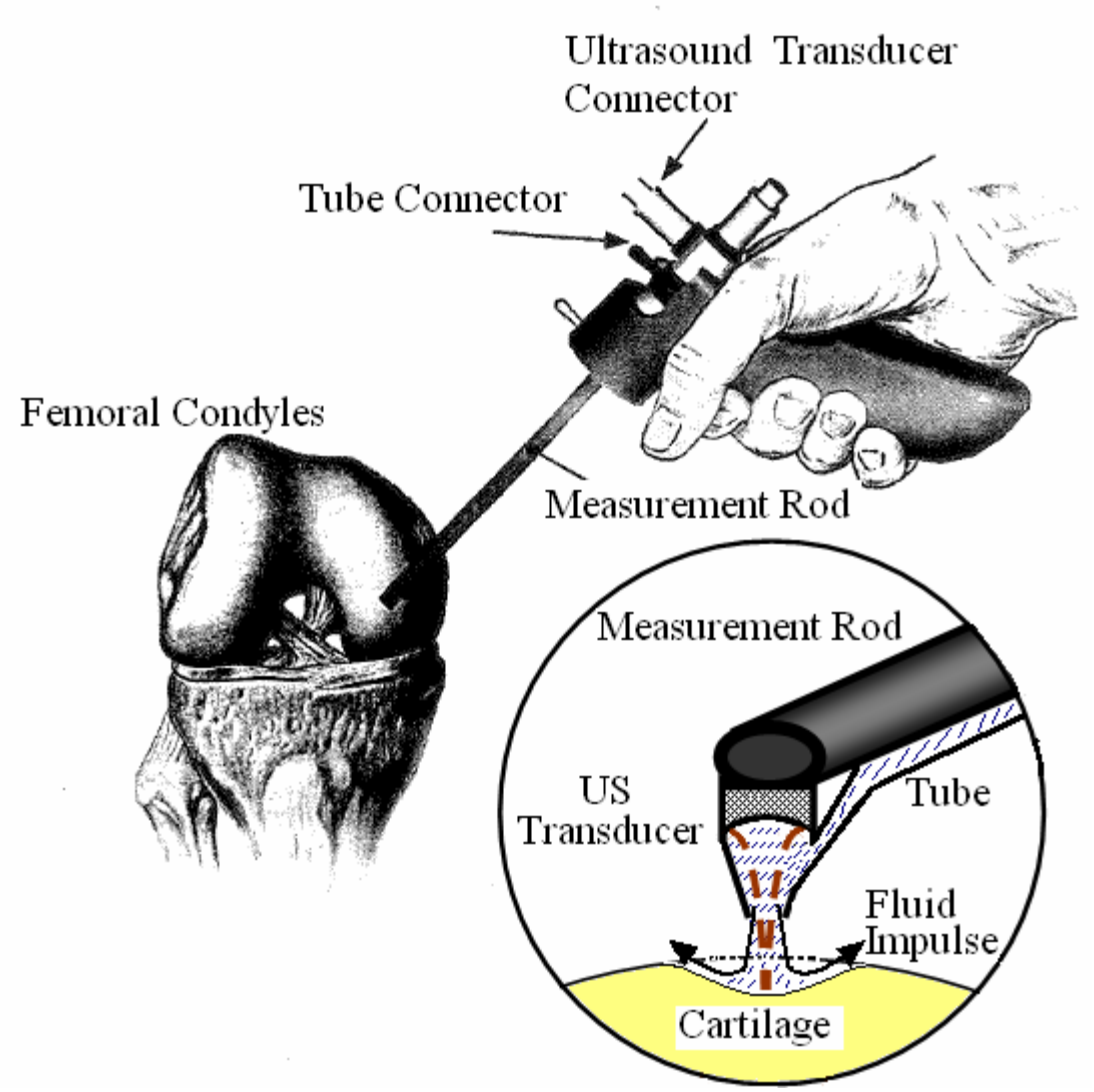

Figure 6-1. Schematic presentation of the hand-held ultrasound water jet indentation system: the measurement principle and the design of the probe.

indentation due to the interaction between the water jet and tissue, the relationship between the flow rate and the severity of the reflected water wave will be established. Together with the theoretical analysis based on the knowledge of fluid dynamics and biomechanics, experimental approaches will be tried to find out the static pressure on the tissue surface and pressure profile at the interface. Multiplexed fibre Bragg grating (FBG)

sensors will be embedded in the phantom to measure the pressure as depicted in Figure 6-2. The FBG sensor is sensitive to the non-uniform strain, therefore it can catch the deformation profile at the interface and then the measured strain can be converted to the pressure by the theory in the mechanics of solids (Ling et al. 2005). Finite element model will also be built to simulate the interaction between the water jet and the soft tissue, in which tissue samples may be modeled as linear elastic, viscoelastic or even poroelastic (Fung 1991).

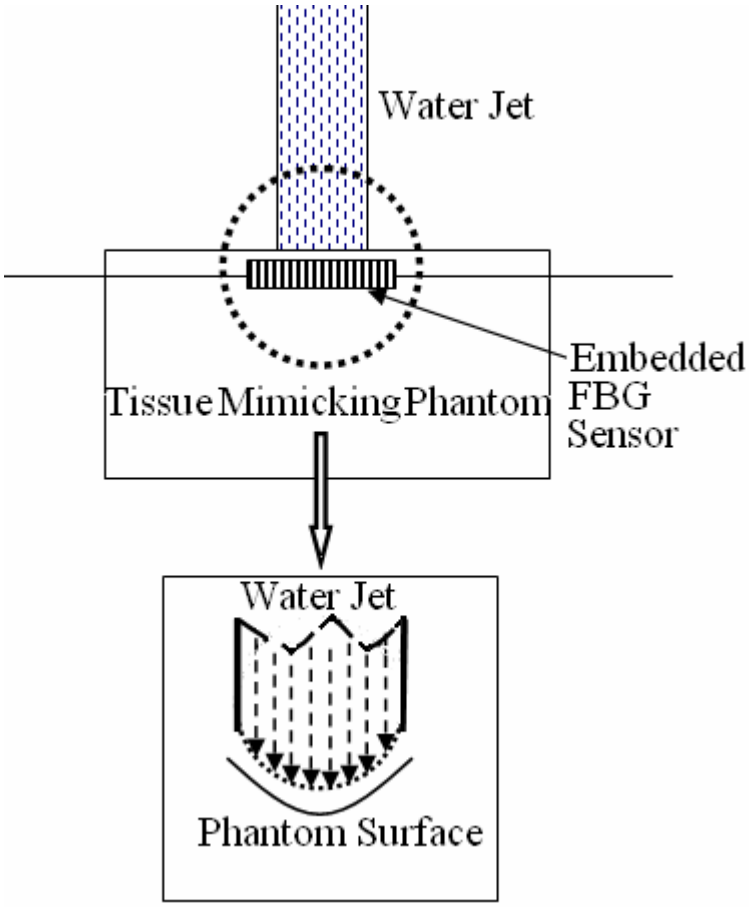

Figure 6-2. Schematic of the deformation profile measurement using embedded FBG sensor.

Another task is to extract the intrinsic mechanical properties of soft tissues from the ultrasound water jet indentation. In present study, the stiffness ratio was calculated as an indicator of the stiffness of the samples based on the assumption of a uniform pressure distribution on the tissue surface and that the samples were modeled as linear elastic materials. Small deformations were obtained under rapid ramp speed to reduce the nonlinearity and viscoelasticity of the samples. In the future studies, creep tests of soft tissue will be conducted through the ultrasound water jet indentation. A controller will be added to the system for the accurate and good control of the flow rate. The measured force-deformation curve will be fitted by the elastic and quasi-linear viscoelastic (QLV) models. The intrinsic material properties of soft tissues may be determined from the creep tests.

The fourth task is to determine the layered properties of soft tissues with ultrasound water jet indentation. Ultrasound indentation has demonstrated its ability to quantify deformations in different layers of soft tissue (Zheng 1997, Huang 2005). The ability of ultrasound indentation to pick up non-homogeneous time-dependent deformation in different sub-layers within a tissue may be useful when more precise biomechanical assessments are required for specific tissue sub-layers. The ultrasound water jet indentation system, using higher frequency ultrasound, can obtain both A-mode and B-mode (can be obtained using 1-D scan across the tissue surface) ultrasound signals from the inner structures of the tissue. By tracking the echoes or patterns reflected from the

inside structure of the tissue, the local strain can be obtained and a micro-elastogram which presents the strain distribution inside soft tissues along the transducer axis at a microscopic level can be constructed. The micro-elastogram should be very helpful for the investigation of the non-homogeneity of thin tissues *in situ* or *in vivo*.

The fifth task is to conduct measurement of acoustical properties of soft tissues. As reported in this thesis, the ultrasound water jet indentation system is convenient not only for the assessment of tissue mechanical properties, but also for the measurement of acoustical properties of tissues. However, only peak-to-peak values of the A-mode echoes reflected from the tissue surface were analyzed for the diagnosis of the degeneration of articular cartilage. In the future studies, both A-mode echoes and B-mode images will be analyzed using wavelet transformation (Hattori et al. 2004). The attenuation and backscatter will also be determined from the power spectrum of the ultrasound reflection signals obtained by the ultrasound water jet indentation system for the diagnosis purpose (Huang 2005).

In addition, optical validations will be conducted using optical microelastography or OCT elastography when the ultrasound water jet indentation system is used to measure the layered mechanical properties of tissues. Optical validation system has been developed using an arthroscopy system (Huang 2004). Besides this arthroscopic validation system, an OCT system, which provides a higher resolution for imaging than any available

clinical technology, will be used for the investigation of the mechanical properties of soft tissue, as well as providing a validation for the ultrasound system.

In summary, based on the future tasks mentioned above to further improve the ultrasound water jet indentation system, it will be used to perform indentation tests on small specimens at microscopic levels for biological tissues and other materials, such as small animal tissues, bioengineered tissues, semiconductor materials, thin films, etc., where nanoindentation is widely used.

REFERENCES

Adam C, Eckstein F, Milz S, Schulte E, Becker C, and Putz R. The distribution of cartilage thickness in the knee-joints of old-aged individuals - measurement by A-mode ultrasound. Clinical Biomechanics. 13: 1-10, 1998.

Adler RS, Dedrick DK, Laing TJ,Chiang EH, Meyer CR, Bland PH, Rubin JM. Quantitative assessment of cartilage surface roughness on osteoarthritis using high frequency ultrasound. Ultrasound in Medicine and Biology. 18: 51-58, 1992.

Ahsan T, Sah RL. Biomechanics of integrative cartilage repair. Osteoarthritis and Cartilage. 7:29-40, 1999.

Appleyard RC, Swain MV, Khanna S, Murrell GAC. The accuracy and reliability of a novel handheld dynamic indentation probe for analysing articular cartilage. Physics in Medicine and Biology. 46: 541-550, 2001.

Ateshian GA, Soslowsky LJ, Mow VC. Quantitation of articular surface topography and cartilage thickness in knee joints using stereophotogrammetry. Journal of Biomechanics. 24: 761-776, 1991.

Athanasiou KA, Agarwal A, Muffoletto A, Dzida FJ, Constantinides G, and Clem M. Biomechanical properties of hip cartilage in experimental animal-models. Clinical Orthopaedics and Related Research. 316: 254-266, 1995b.

Athanasiou KA, Fleischli JG, Bosma J, Laughlin TJ, Zhu CF, Agrawal CM, and Lavery LA. Effects of diabetes mellitus on the biomechanical properties of human ankle cartilage. Clinical Orthopaedics and Related Research. 368: 182-189, 1999.

Athanasiou KA, Niederauer GG, and Schenck RC. Biomechanical topography of human ankle cartilage. Annals of Biomedical Engineering. 23: 697-704, 1995a.

Athanasiou KA, Zhu CF, Wang X, and Agrawal CM. Effects of aging and dietary restriction on the structural integrity of rat articular cartilage. Annals of Biomedical Engineering. 28: 143-149, 2000.

Arokoski JPA, Hyttinen MM, Helminen HJ, and Jurvelin JS. Biomechanical and structural characteristics of canine femoral and tibial cartilage. Journal of Biomedical Materials Research. 48: 99-107, 1999.

Arokoski J, Jurvelin J, Kiviranta I, Tammi M, and Helminen HJ. Softening of the lateral condyle aricular-cartilage in the canine knee-joint after long-distance (up to 40KM/day) running training lasting one-year. International Journal of Sports Medicine. 15: 254-260, 1994.

Bae Wc, Lewis CW, Sah RL. Intra-tissue strain distribution in normal human cartilage during clinical indentation testing. [49th annual meeting of the Orthopaedic Research Society; New Orleans, La]. Transactions on Orthopaedic Research Society. 28: 1, 2003.

Barannik EA, Girnyk A, Tovstiak V, Marusenko AI, Emelianov SY, Sarvazyan AP. Doppler ultrasound detection of shear waves remotely induced in tissue phantoms and tissue in vitro. Ultrasonics. 40: 849-852, 2002.

Barnett SB, Rott HD, ter Haar GR, Ziskin MC, Maeda K. The sensitivity of biological tissue to ultrasound. Ultrasound in Medicine and Biology. 23: 805-812, 1997.

BeDell KK, Scremin AME, Perell KL, Kunkel CF. Effects of functional electrical stimulation – induced lower extremity cycling on bone density of spinal cord-injured patients. American Journal of Physical Medicine and Rehabilitation. 75: 29-34, 1996.

Belanger M, Stein RB, Wheeler GD, Gordon T, Leduc B. Electrical stimulation: can it increase muscle strength and reverse osteopenia in spinal cord injured individuals? Archives of Physical Medicine and Rehabilitation. 81: 1090-1098, 2000.

Bendat JS, Piersol AG. Random data: analysis and measurement, 2nd edition. New York: John Wiley and Sons, 1986.

Birks AS and Green RE. Ultrasonic testing: nondestructive testing handbook. 1991; Columbus, OH: American Society for Nondestructive Testing, Inc.

Bland JM, Altman DG. Statistical methods for assessing agreement between two methods of clinical measurement. Lancet. 1: 307-310, 1986.

Buchtal F, Kaiser E. The rheology of the cross striated muscle fiber with particular reference to isotonic conditions. Det Kongelige Danske Videnskabernes Selskab, Copenhagen, Danmark Biology and Medicine. 21: 328, 1951.

Buckwalter JA. Osteoarthritis and articular cartilage use, disuse, and abuse: experimental studies. Journal of Rheumatology. 43(suppl):13-15, 1995.

Burr DB, Frederickson RG, Pavlinch C, Sickles M, Burkart S. Intracast muscle stimulation prevents bone and cartilage deterioration in cast-immobilized rabbits. Clinical Orthopaedics and Related Research. 189: 264-278, 1984.

Burstein D, Bashir A, Gray ML. MRI techniques in early stages of cartilage disease. Investigative Radiology. 35: 622-638, 2000.

Buschmann MD, Grodzinsky AJ. A molecular model of proteoglycan-associated electrostatic forces in cartilage mechanics. Journal of Biomechanical Engineering – Transactions of the ASME. 117: 179-192, 1995.

Bushong SC and Archer BR. Diagnostic ultrasound: physics, biology, and instrumentation. New York: Mosby. 1991.

Catheline S, Thomas JL, Wu F, Fink MA. Diffraction field of a low frequency vibrator in soft tissues using transient elastography. IEEE Transactions on Ultrasonics, Ferroelectrics and Frequency Control. 46: 1013-1019, 1999.

Ce´spedes I, Ophir J. Reduction of image noise in elastography. Ultrasonic Imaging. 15: 89–102, 1993.

Ce´spedes I, Ophir J, Ponnekanti H, Maklad N. Elastography: elasticity imaging using ultrasound with application to muscle and breast in vivo. Ultrasonic Imaging. 15: 73-88, 1993.

Chaffai S, Peyrin F, Nuzzo S, Porcher R, Berger G, Laugier P. Ultrasonic characterization of human cancellous bone using transmission and backscatter measurements: relationship to density and microstructure. Bone. 30: 229-237, 2002.

Cherin E, Saied A, Laugier P, Netter P, Berger G. Evaluation of acoustical parameter sensitivity to age-related and osteoarthritic changes in articular cartilage using 50-MHz ultrasound. Ultrasound in Medicine and Biology. 24: 341-354, 1998.

Chicot D, Hage I, Demarecaux P, Lesage J. Elastic properties determination from indentation tests. Surface & Coatings Technology. 81: 269-274, 1996.

Cohen ZA, Mccarthy DM, Kwak SD, Legrand P, Fogarasi F, Ciaccio EJ, Ateshian GA. Knee cartilage topography, thickness, and contact areas from MRI: in-vitro calibration and in-vivo measurements. Osteoarthritis and Cartilage. 7: 95-109, 1999.

Cohn NA, Emelianov SY, Lubinski MA, O'Donnell M. An elasticity microscope .1. Methods. IEEE Transactions on Ultrasonics, Ferroelectrics and Frequency Control. 44: 1304-1319, 1997a.

Cohn NA, Emelianov SY, Lubinski MA, O'Donnell M. An elasticity microscope .2. Experimental results. IEEE Transactions on Ultrasonics, Ferroelectrics and Frequency Control. 44: 1320-1331, 1997b.

Cohn NA, Kim BS, Erkamp RQ, Mooney DJ, Emelianov SY, Skovoroda AR, O'Donnell M. High-resolution elasticity imaging for tissue engineering. IEEE Transactions on Ultrasonics, Ferroelectrics and Frequency Control. 47: 956-966, 2000.

Donnon FG. The theory of membrane equilibria. Chemistry Review. 1: 73-90, 1924.

Donzelli PS, Spilker RL, Baehmann PL, Niu Q, Shephard MS. Automated adaptive analysis of the biphasic equations for soft-tissue mechanics using a-posteriori error indicators. International Journal of Numerical Methods in Engineering. 34: 1015-1033, 1992.

Doyley MM, Bamber JC, Fuechsel F, Bush NL. A freehand elastographic imaging approach for clinical breast imaging: System development and performance evaluation. Ultrasound in Medicine and Biology. 27: 1347-1357, 2001.

Duck FA. Physical properties of tissue: a comprehensive reference book. London: Academic Press, 1990.

Eckstein F, Sittek H, Milz S, Schulte E, Kiefer B, Reiser M, Putz R. The potential of magnetic resonance imaging (MRI) for quantifying articular cartilage thickness – A methodological study. Clinical Biomechanics. 10: 434-440, 1995.

Fatemi M, Greenleaf JF. Ultrasound-stimulated vibro-acoustic spectrography. Science. 280: 82-85, 1998.

Fatemi M, Greenleaf JF. Vibro-acoustography: An imaging modality based on ultrasound-stimulated acoustic emission. Proceedings of the National Academy of Sciences of USA. 96: 6603-6608, 1999.

Fatemi M, Wold LE, Alizad A, Greenleaf JF. Vibro-acoustic tissue mammography. IEEE Transactions on Medical Imaging. 21: 1-8, 2002.

Ferguson VL, Bushby AJ, Boyde A. Modulus and mineralisation of articular calcified cartilage and subchondral bone in osteoarthritis via nanoindentation and quantitative backscattered electron imaging. Journal of Bone and Mineral Research. 17: 945, 2002.

Fortin M, Buschmann MD, Bertrand MJ, Foster FS, Ophir J. Dynamic measurement of internal solid displacement in articular cartilage using ultrasound backscatter. Journal of Biomechanics. 36: 443–447, 2003.

Foster FS, Pavlin CJ, Harasiewicz KA, Christopher DA, Turnbull DH. Advances in ultrasound biomicroscopy, Ultrasound in Medicine and Biology. 26: 1-27, 2000.

Fung YC. Biomechanics: Mechanical Properties of Living Tissues. Spring-Verlag. 1993.

Galbraith PC, Bryant JT. Effect of grid dimensions on finite element models of an articular surface. Journal of Biomechanics. 22: 385-393, 1989.

Garra BS, Cespedes EI, Ophir J, Spratt SR, Zuurbier RA, Magnant CM, Pennanen MF. Elastography of breast lesions: Initial clinic results. Radiology. 202: 79–86, 1997.

Gluer CC, Blake G, Lu Y, Blunt BA, Jergas M, Genant HK. Accurate assessment of precision errors: how to measure the reproducibility of bone densitometry techniques. Osteoporosis International. 5: 262-270, 1995.

Guilak F, Ratcliffe A, Mow VC. Chondrocyte deformation and local tissue strain in articular cartilage: a confocal microscopy study. Journal of Orthopaedic Research. 13: 410-421, 1995.

Guo LH, Guo X, Leng Y, Cheng JCY, Zhang XD. Nanoindentation study of interfaces between calcium phosphate and bone in an animal spinal fusion model. Journal of Biomedical Materials Research. 54: 554-559, 2001.

Haapala J, Arokoski JP, Pirttimaki J, Lyyra T, Jurvelin J, Tammi M, Helminen HJ, Kiviranta I. Incomplete restoration of immobilization induced softening of young beagle knee articular cartilage after 50-week remobilization. International Journal of Sports Medicine. 21: 76-81, 2000.

Habelitz S, Marshall SJ, Marshall GW, Balooch M. Mechanical properties of human dental enamel on the nanometre scale. Archives of Oral Biology. 46: 173-183, 2001.

Hadjiargyrou M, McLeod K, Ryaby JP, Rubin C. Enhancement of fracture healing by low intensity ultrasound. Clinical Orthopaedics and Related Research. 355: S216-S229, 1998.

Haider MA, Holmes MH. A mathematical approximation for the solution of a static indentation test. Journal of Biomechanics. 30: 747-751, 1997.

Hale JE, Rudert MJ, Brown TD. Indentation assessment of biphasic mechanical property deficits in size-dependent osteochondral defect repair. Journal of Biomechanics. 26: 1319-1325, 1993.

Hall TJ, Bilgen M, Insana MF, Krouskop TA. Phantom materials for elastography. IEEE Transactions on Ultrasonics, Ferroelectrics and Frequency Control. 44: 1355-1365, 1997.

Hamilton JD, Brooks CJ, Vossler GL, O'Donnell M. High frequency ultrasound imaging using an active optical detector. IEEE Transactions on Ultrasonics, Ferroelectrics and Frequency Control. 45: 719-727, 1998.

Han LH, Noble JA, Burcher M. A novel ultrasound indentation system for measuring biomechanical properties of in vivo soft tissue. Ultrasound in Medicine and Biology. 29: 813-823, 2003.

Hattori K, Takakura Y, Ishimura M, Habata T, Uematsu K, Ikeuch K. Quantitative arthroscopic ultrasound evaluation of living human cartilage. Clinical Biomechanics. 19: 213-216, 2004.

Hattori K, Mori K, Yamaoka S, Habata T, Takakura Y, Tomita N, Ikeuch K. Experimental assessment of the mechanical properties of articular cartilage using ultrasonic echoes. Transaction of Orthopaedic Research Soociety. 27: 393, 2002.

Hattori K, Mori K, Habata T, Takakura Y, Ikeuch K. Measurement of the mechanical condition of articular cartilage with an ultrasonic probe: quantitative evaluation using wavelet transformation. Clinical Biomechanics. 18: 553-557, 2003.

Hayes WC, Keer LM, Herrmann G, Mockros LF. A mathematical analysis for indentation tests of articular cartilage. Journal of Biomechanics. 5: 541-551, 1972.

Hoffmann K, Jung J, et Gammal S, Altmeyer P. Malignant melanoma in 20-MHz B scan sonography. Dermatology. 185: 49-55, 1992.

Hollman K, Emelianov SY, Neiss JH, Jotyan G, Spooner GJR, Juhasz T, Kurtz RM, O'Donnell M. Strain imaging of corneal tissue with an ultrasound elasticity microscope. Cornea. 21: 68-73, 2002.

Hori RY, Mockros LF. Indentation tests of human articular-cartilage. Journal of Biomechanics. 9: 259-268, 1976.

Huang YP. Ultrasonic assessment of post-radiotherapy fibrosis. M.Phil. Dissertation, The Hong Kong Polytechnic University, Hong Kong, P.R.C., 2005.

Huang SR, Lerner RM, Parker KJ. Time Domain Doppler estimators of the amplitude of vibrating targets. Journal of Acoustic Society of American. 91: 965-974, 1992.

Huang QH, Lu MH, Zheng YP. Optical and ultrasound elastomicroscopy for imaging tissue elasticity in high resolution. Conference on Biomedical Engineering, BME 2004, 23 -25 September 2004, Hong Kong: 130-134

Huang D, Swanson EA, Lin CP, Schuman JS, Stinson WG, Chang W, Hee MR, Flotte T, Gregory K, Puliafito CA, Fujimoto JG. Optical Coherence Tomography. Science. 254: 1178-1181, 1991

Hung LK, Lee SY, Leung KS, Chan KM, Nicholl LA. Partial patellectomy for patellar fracture: tension band wiring and early mobilization. Journal of Orthopaedic Trauma. 7: 252-260, 1993.

Hunziker EB. Artcular cartilage repair: basic science and clinical progress. A review of the current status and prospects. Osteoarthritis and cartilage. 10: 432-463, 2001.

Javed A, Siddique M, Vaghela M, Hui ACW. Interobserver variation in intra-articular evaluation during arthroscopy of the knee. Journal of Bone and Joint Surgery – British Volume. 84: 48-49, 2002.

Joiner GA, Bogoch ER, Pritzker KP, Buschmann MD, Chevrier A, Foster FS. High frequency acoustic parameters of human and bovine articular cartilage following experimentally-induced matrix degradation. Ultrasonic Imaging. 23: 106-116, 2001.

Jurvelin J, Kiviranta I, Saamanen AM, Tammi M, Helminen HJ. Indentation stiffness of young canine knee articular-cartilage – influence of strenuous joint loading. Journal of Biomechanics. 23: 1239-1246, 1990.

Jurvelin JS, Rasanen T, Kolmonen P, Lyyra T. Comparision of optical, needle probe and ultrasonic techniques for the measurement of articular-cartilage thickness. Journal of Biomechanics. 28: 231-235, 1995.

Kallel F, Ophir J. A least squares estimator for elastography. Ultrasonic Imaging. 19: 195–208, 1997a.

Kallel F, Ophir J. Three dimensional tissue motion and its effects on image noise in elastography. IEEE Transactions on Ultrasonics, Ferroelectrics and Frequency Control. 44: 1286–1296, 1997b.

Kawchuk GN, Fauvel OR, Dmowski J. Ultrasound indentation: a procedure for the noninvasive quantification of force-displacement properties of the lumber spine. Journal of Manipulative and Physiological Therapeutics. 24: 149-156, 2001.

Kempson GE, Freeman MAR, Swanson SAV. Determination of a creep modulus for articular cartilage from indentation tests on human femoral head. Journal of Biomechanics. 4: 239-&, 1971.

Kim HKW, Babyn PS, Harasiewicz KA, Pritzker KPH, Foster FS. High resolution imaging of articular cartilage using ultrasound biomicroscopy. Journal of Orthopaedic Research. 13: 963-970, 1995.

Knapik DA, Starkosky B, Palvin CJ, Foster FS. A realtime 200 MHz ultrasound B-scan imager. IEEE Ultrasound Symposium Proceeding. 1457-1461, 1997.

Konofagou EE, Ophir J. A new elastographic method for estimation and imaging of lateral displacements, lateral strains, corrected axial strains and Poisson's ratios in tissues. Ultrasound in Medicine and Biology. 24: 1183–1199, 1998.

Konofagou EE, Harrigan TP, Ophir J, Krouskop TA. Poroelastography: imaging the poroelastic properties of tissues. Ultrasound in Medicine and Biology. 27: 1387-1397, 2001.

Korhonen RK, Saarakkala S, Toyras J, Laasanen MS, Kiviranta K, Jurvelin JS. Experimental and numerical validation for the novel configuration of an arthroscopic indentation instrument. Physics in Medicine and Biology. 48: 1565-1576, 2003.

Kovach IS. A molecular theory of cartilage viscoelasticiity. Biophysical Chemistry. 59: 61-73, 1996.

Krautkramer J, Krautkramer H. Ultrasonic testing of materials. New York: Springer-Verlag. 1969.

Kreklau B, Sittinger M, Mensing MB, Voigt C, Berger G, Burmester GR, Rahmanzadeh R, Gross U. Tissue engineering of biphasic joint cartilage transplants. Biomaterials. 20:1743-1749, 1999.

Krouskop TA, Dougherty DR, Vinson FS. A pulsed Doppler ultrasonic system for making noninvasive measurement of the mechanical properties of soft tissue. Journal of Rehabilitation Research. 14: 1–8, 1987.

Krouskop TA, Wheeler TM, Kallel F, Garra BS, Hall T. The elastic moduli of breast and prostate tissues under compression. Ultrasonic Imaging. 20: 260-274, 1998.

Laasanen MS, Saarakkala S, Toyras J, Hirvonen J, Rieppo J, Korhonen RK, Jurvelin JS. Ultrasound indentation of bovine knee articular cartilage in situ. Journal of Biomechanics. 36: 1259-1267, 2003a.

Laasanen MS, Saarakkala S, Toyras J, Rieppo J, Jurvelin JS. Site-specific ultrasound reflection properties and superficial collagen content of bovine knee articular cartilage. Physics in Medicine and Biology. 50: 3221-3233, 2005.

Laasanen MS, Toyras J, Vasara AI, Hyttinen MM, Saarakkala S, Hirvonen J, Jurvelin JS, Kiviranta I. Mechano-acoustic diagnosis of cartilage degeneration and repair. Journal of Bone and Joint Surgery – American Volume. 85A: 78-84, 2003b.

Laasanen MS, Toyras J, Hirvonen J, Saarakkala S, Korhonen RK, Nieminen MT, Kiviranta I, Jurvelin JS. Novel mechano-acoustic technique and instrument for diagnosis of cartilage degeneration. Physiological Measurement. 23: 491-503, 2002.

Lai WM, Hou JS, Mow VC. A triphasic theory for the swelling and deformation behaviors of articular cartilage. Journal of Biomechanical Engineering – Transactions of the ASME. 113: 245-258, 1991.

Lane JM, Chisena E, Black J. Experimental knee instability: early mechanical property changes in articular cartilage in a rabbit model. Clinical Orthopaedics and Related Research. 140: 262-272, 1979.

Lassau N, Spatz A, Avril M, Tardivon A, Margulis A, Mamelle G, Vanel D, Leclere J. Value of high frequency ultrasound for preoperative assessment of skin tumors. Radiographics. 17: 1559-1565, 1997.

Lee F, Bronson JP, Lerner RM, Parker KJ, Huang SR, Roach DJ. Sonoelasticity imaging: results in vitro tissue specimens. Radiology. 181: 237-239, 1991.

Lerner RM, Huang SR, Parker KJ. Sonoelasticity images derived from ultrasound signals in mechanically vibrated tissues. Ultrasound in Medicine and Biology. 16: 231-239, 1990.

Leung KS, Qin L, Leung MCT, Fu LLK, Chan CW. Partial patellectomy induces a decrease in the proteoglycan content in the remaining patellar articular cartilage. An

experimental study in rabbits. Clinical and Experimental Rheumatology. 17: 597-600, 1999.

Levinson SF, Shinagawa M, Sato T. Sonoelastic deformation of human skeletal-muscle elasticity. Journal of Biomechanics. 28: 1145-1154, 1995.

Ling HY, Lau KT, Cheng L. Determination of dynamic strain profile of composite structures using embedded multiplexed fibro-optic sensors. Composite Structures. 66: 317-326, 2004.

Ling HY, Lau KT, Cheng L, Chow KW. Embedded fibre Bragg grating sensors for non-uniform strain sensing in composite structures. Measurement Science and Technology. 16: 2415-2424, 2005.

Liu JB, Goldberg BB. Endolunimal vascular and nonvascular sonography: past, present, and future. American Journal of Roentgenogram. 165: 765-774, 1995.

Lu MH, Zheng YP. Indentation test of soft tissues with curved cubstrates: a finite element study. Medical and Biological Engineering and Computing. 42: 535-540, 2004.

Lyyra T, Arokoski JPA, Oksala N, Vihko A, Hyttinen M, Jurvelin JS, Kiviranta I. Experimental validation of arthroscopic cartilage stiffness measurement using enzymatically degraded cartilage samples. Physics in Medicine and Biology. 44: 525-535, 1999a.

Lyyra T, Jurvelin J, Pitkanen P, Vaatainen U, Kiviranta I. Indentation instrument for the measurement of cartilage stiffness under arthroscopic control. Medical Engineering & Physics. 17: 395-399, 1995.

Lyyra T, Kiviranta I, Vaatainen U, Helminen HJ, Jurvelin JS. In vivo characterization of indentation stiffness of articular cartilage in the normal human knee. Journal of Biomedical Materials Research. 48: 482-487, 1999b.

Mak AF, Lai WM, and Mow VC. Biphasic indentation of articular-cartilage .1. theoretical -analysis. Journal of Biomechanics. 20: 703-714, 1987.

Maroudas A, Wachtel E, Grushko G, Katz EP, Weinberg P. The effect of osmotic and mechanical pressures on water partitioning in articular cartilage. Biochemica Et Biophysica Acta, 1073: 285-294, 1991.

Mayr E, Laule A, Suger G, Ruter A, Claes L. Radiographic results of callus distraction aided by pulsed low-intensity ultrasound. Journal of Orthopaedic Trauma. 15: 407-415, 2001.

McDevitt CA, Muir H. Biochemical changes in the cartilage of the knee in experimental and natural osteoarthritis in the dog. Journal of Bone and Joint Surgery – British Volume. 58B: 94-101, 1976.

Mollenhauer J, Aurich ME, Zhong Z, Muehleman C, Cole CC, Hasnah M, Oltulu O, Kuettner KE, Margulis A, Chapman LD. Diffraction-enhanced x-ray imaging of articular cartilage. Osteoarthritis and Cartilage. 10: 163-171, 2002.

Mow VC, Gibbs MC, Lai WM, Zhu WB, Athanasiou KA. Biphasic indentation of articular-cartilage .2. a numberical algorithm and an experimental-study. Journal of Biomechanics. 22: 853-861, 1989.

Mow VC, Hayes WC. Basic Orthopaedic Biomechanics. 2nd edition. Lippincott-Raven. 1997.

Mow VC, Kuei SC, Lai WM, Armstrong CG. Biphasic creep and stress relaxation of articular cartilage in compression: theory and experiment. Journal of Biomechanical Engineering – Transactions of the ASME. 102: 70-84, 1980.

Mow VC, Holmes MH, Lai WM. Fluid transport and mechanical properties of articular cartilage: A review. Journal of Biomechanics. 17: 377-394, 1984.

Muir T, Carstensen E. Prediction of nonlinear acoustic effects at biomedical frequencies and intensities. Ultrasound in Medicine and Biology. 6: 345–357, 1980.

Naito T, Ohdaira E, Masuzawa N, Ide M. Relationship between cavitation threshold and dissolved air in ultrasound in the MHz range. Japanese Journal of Applied Physics Part I. 37: 2990-2991, 1998.

Newton PM, Mow VC, Gardner TR, Buckwalter JA, Albright JP. The effect of lifelong exercise on canine articular cartilage. American Journal of Sports Medicine. 25: 282-287, 1997.

Niederauer MQ, Cristante S, Neierauer GM, et al. A novel instrument for quantitatively measuring the stiffness of articular cartilage. Transactions of the Orthopaedic Research Society. 23: 905, 1998.

Nieminen MT, Toyras J, Laasanen MS, Rieppo J, Silvennoinen J, Helminen HJ, Jurvelin JS. MRI quantitation of proteoglycans predicts cartilage stiffness in bovine humeral head. Transactions of the Orthopaedic Research Society. 26: 127, 2001a.

Nieminen MT, Toyras J, Rieppo J, Hakumaki JM, Silvennoinen J, Helminen HJ, Jurvelin JS. Quantitative MR microscopy of enzymatically degraded articular cartilage. Magnetic Resonance in Medicine. 43: 676-681, 2000.

Nieminen MT, Toyras J, Rieppo J, Silvennoinen J, Hakumaki JM, Hyttinen MM, Helminen HJ, Jurvelin JS. T2 relaxation reveals spatial collagen architecuture in articular cartilage: a comparative quantitative MRI and polarized light microscopic study. Magnetic Resonance in Medicine. 46: 487-493, 2001b.

Nightingale KR, Kornguth PJ, Trahey GE. The use of acoustic streaming in breast lesion diagnosis: A clinical study. Ultrasound in Medicine Biology. 25: 75-87, 1999.

Nightingale KR, Kornguth PJ, Walker WF, Mcdermott BA, Trahey GE. A novel ultrasonic technique for differentiating cystc from solid lesions. Ultrasound in Medicine and Biology. 21: 745-751, 1995.

Nightingale K, Soo MS, Nightingale R, Trahey G. Acoustic radiation force impulse imaging: In vivo demonstration of clinical feasibility. Ultrasound in Medicine and Biology. 28: 227-235, 2002.

Nyborg W. Acoustic streaming, In: Mason W, ed. Physical acoustics, 1965, Vol. IIB, 265-331 (Academic Press Inc., New York).

O'Donnell M, Skovoroda AR, Shapo BM, Emelianov SY. Internal displacement and strain imaging using ultrasonic speckle tracking. IEEE Transactions on Ultrasonics, Ferroelectrics and Frequency Control. 41: 314–325, 1994.

Ophir J, Alam SK, Garra B, Kallel F, Konofagou E, Krouskop T, Varghese T. Elastography: ultrasonic estimation and imaging of the elastic properties of tissues. Proceedings of the Institution of Mechanical Engineers Part H- Journal of Engineering in Medicine. 213 (H3): 203-233, 1999.

Ophir, J, Ce´spedes, EI, Ponnekanti H, Yazdi Y, Li X. Elastography: a quantitative method for imaging the elasticity of biological tissues. Ultrasonic Imaging. 13: 111–134, 1991.

Ophir J, Kallel F, Varghese T, Bertrand M, Ce´spedes I, Ponnekanti H. Elastography: a systems approach. International Journal of Imaging Systems and Technology. 8: 89–103, 1997.

Ophir J, Parker KJ. Contrast agents in diagnostic ultrasound. Ultrasound in Medicine and Biology. 15: 319-333, 1989.

Passmann C, Ermert H. In vivo imaging of skin in the 100 MHz region using the synthetic aperture concept. IEEE Ultrasound Symposium. 2: 1287-1290, 1995.

Parsons JR, Black J. The viscoelastic shear behaviour of normal rabbit articular cartilage. Journal of Biomechanics. 10: 21-29, 1977.

Parsons JR, Black J. Mechanical behaviour of articular cartilage: quantitative changes with alteration of ionic environment. Journal of Biomechanics. 12: 765-773, 1979.

Parvizi J, Wu CC, Lewallen DG, Greenleaf JF, Bolander ME. Low-intensity ultrasound stimulates proteoglycan synthesis in rat condrocytes by increasing aggrecan gene expression. Journal of Orthopaedic Research. 17: 488-494, 1999.

Patil SG, Zheng YP, Shi J. Measurement of Depth-dependence and anisotropy of ultrasound speed of bovine articular cartilage in vitro. Ultrasound in Medicine and Biology. 30: 953-963, 2004.

Pavlin CJ, Christopher DA, Burns PN, Foster FS. High frequency Dopler examination of the anterior segment of the sys. American Journal of Ophthalmology. 126; 597-600, 1998.

Pavlin CJ, Foster FS. Ultrasound biomicroscopy of the eye. New York: Springer-Verlag, 1995.

Pethica JB, Hutchings R, Oliver WC. Hardness measurement at penetration depths as small as 20-nm. Philosophical Magazine A – Physics of Condensed Matter Structure Defects and Mechanical Properties. 48: 593-606, 1983.

Phillips D, Chen XC, Baggs R, Rubens D, Violante M, Parker KJ. Acoustic backscatter properties of the particle/bubble ultrasound contrast agent. Ultrasonics. 36: 883-892, 1998.

Pilla AA, Mont MA, Nasser PR, Khan SA, Figueiredo M, Kaufman JJ, Stiffert RS. Non-invasive low-intensity pulsed ultrasound accelerates bone healing in the rabbit. Journal of Orthopaedic Trauma. 4: 246-253, 1990.

Qin L. Morphological studies on precention of immobilization atrophy of skeletal muscle by electrical stimulation. Dissertation, German Sports University, Cologne, F.R.G., 1992.

Qin L, Appell HJ, Chan KM, Maffulli N. Electrical stimulation prevents immobilization atrophy in skeletal muscle of rabbits. Archives of Physical Medicine and Rehabilitation. 78: 512-517, 1997.

Qin L, Fok PK, Lu HB, Shi SQ, Leng Y, Leung KS. Low intensity pulsed ultrasound increases the matrix hardness of the healing tissues at bone-tendon insertion – a partial patellectomy model in rabbits. Clinical Biomechanics. 21: 387-394, 2006.

Qin L, Leung KS, Chan CW, Fu LK, Rosier R. Enlargement of remaining patella after partial patellectomy in rabbits. Medicine and Science in Sports and Exercise. 31: 502-506, 1999.

Qin L, Zheng YP, Leung CT, Mak AFT, Choy WY, Chan KM. Ultrasound detection of trypsin-treated articular cartilage: its association with cartilagious proteoglycans assessed by histological and biochemical methods. Journal of Bone and Mineral Metabolism. 20: 281-287, 2002.

Radin EL, Paul IL, Tolkoff MJ. Subchondral bone changes in patients with ealy degenerative joint disease. Arthritis and Rheumatism. 13: 400-405, 1970.

Rho JY, Tsui TY, Pharr GM. Elastic properties of human cortical and trabecular lamellar bone measured by nanoindentation. Biomaterials. 18: 1325-1330, 1997.

Righetti R, Ophir J, Ktonas P. Axial resolution in elastography. Ultrasound in Medicine and Biology. 28: 101-113, 2002.

Righetti R, Ophir J, Krouskop TA. A method for generating permeability elastograms and Poisson's ratio time-constant elastograms. Ultrasound in Medicine and Biology. 31: 803-816, 2005.

Righetti R, Ophir J, Srinivasan S, Krouskop TA. The feasibility of using elastography for imaging the Poisson's ratio in porous media. Ultrasound in Medicine and Biology. 30: 215-228, 2004.

Righetti R, Srinivasan S, Ophir J. Lateral resolution in elastography. Ultrasound in Medicine and Biology. 29: 695-704, 2003.

Roelandt J, Gussenhoven E, Bom NI. Intravascular ultrasound. London: Kluwer Press, 1993.

Roux C, Roberjot V, Porcher R, Kolta S, Dougados M, Laugier P. Ultrasonic backscatter and transmission parameters at the os calcis in postmenopausal osteoposis. Journal of Bone and Mineral Research. 16: 1353-1362, 2001.

Rubens DJ, Hadley MA, Alam SK, Gao L, Mayer RD, Parker KJ. Sonoelasticity imaging of prostate cancer: in vitro results. Radiology. 195: 379–383, 1995.

Saarakkala S, Laasanen MS, Jurvelin JS, Torronen K, Lammi MJ, Lappalainen R, Toyras J. Ultrasound indentation of normal and spontaneously degenerated bovine articular cartilage. Osteoarthritis and Cartilage. 11: 697-705, 2003.

Saied A, Cherin E, Gaucher H, Laugier P, Gillet P, Floquet J, Netter P, Berger G. Assessment of articular cartilage and subchondral bone: subtle and progressive changes in experimental osteoarthritis using 50 MHz echography in vitro. Journal of Bone and Mineral Research. 12: 1378-1386, 1997.

Sakamoto M, Li GA, Hara T, Chao EYS. A new method for theoretical analysis of static indentation test. Journal of Biomechanics. 29: 679-685, 1996.

Sandrin L, Tanter M, Gennisson JL, Catheline S, Fink M. Shear elasticity probe for soft tissues with 1-D transient elastography. IEEE Transactions on Ultrasonics, Ferroelectrics and Frequency Control. 49: 436-446, 2002a.

Sandrin L, Tanter M, Catheline S, Fink M. Shear modulus imaging with 2-D transient elastography. IEEE Transactions on Ultrasonics, Ferroelectrics and Frequency Control. 49: 426-435, 2002b.

Sanghvi NT, Snoddy AM, Myers SL, Brandt KD, Reilly CR, Franklin TD. Characterization of normal and osteoarthritic cartilage using 25 MHz ultrasound. IEEE Ultrasound Symposium Proceeding. 3: 1413-1416, 1990.

Sarvazyan AP, Rudenko OV, Swanson SD, Fowlkes JB, Emelianov SY. Shear wave elasticity imaging: A new ultrasonic technology of medical diagnostics. Ultrasound in Medicine and Biology. 24: 1419-1435, 1998.

Sato T, Fukusima A, Ichida N, Ishikawa H, Miwa H, Igarashi Y, Shimura T, Murakami K. Nonlinear parameter tomography system using counter propagating probe and pump waves. Ultrasonic Imaging. 7: 49-59, 1985.

Schenck RC, Athanasious KA, Constantinides G, Gomez E. A biomechanical analysis of articular-cartilage of the human elbow and a potential relationship to osteochondritis-dissecans. Clinical Orthopaedics and Related Research. 299: 305-312, 1994.

Schmitt JM. Optical coherence tomography (OCT): A review. IEEE Journal of Selected Topics in Quantum Electronics. 5: 1205-1215, 1999.

Setton LA, Elliott DM, Mow VC. Altered mechanics of cartilage with osteoarthritis: human osteoarthritis and an experimental model of joint degeneration. Osteoarthritis and cartilage. 7: 2-14, 1999.

Shepherd DET, Seedhom BB. Technique for measuring the compressive modulus of articular cartilage under physiological loading rates with preliminary results. Proceedings of the Institution of Mechanical Engineers Part H – Journal of Engineering in Medicine. 211: 155-165, 1997.

Spilker RL, Suh JK, Mow VC. A finite-element analysis of the indentation stress-relaxation response of linear biphasic articular-cartilage. Journal of Biomechanical Engineering – Transactions of the ASME. 114: 191-201, 1992.

Spriet PM, Girard AC, Foster FS, Harasiewicz K, Holdsworth WD, Laverty S. Validation of a 40 MHz B-scan ultrasound biomicroscope for the evaluation of osteoarthritis lesions in an animal model. Osteoarthritis and Cartilage. 13: 171-179, 2005.

Skovoroda AR, Emelianov SY, O'Donnell M. Tissue elasticity reconstruction based on ultrasonic displacement and strain images. IEEE Transactions on Ultrasonics, Ferroelectrics and Frequency Control. 42: 747–765, 1994.

Srinivasan S, Krouskop T, Ophir J. Comparing elastographic strain images with modulus images obtained using nanoindentation: preliminary results using phantoms and tissue samples, Ultrasound in Medicine and Biology. 30: 329–343, 2004.

Srinivasan S, Righetti R, Ophir J. Trade-offs between the axial resolution and the signal-to-noise ratio in elastography. Ultrasound in Medicine and Biology. 29: 847-866, 2003.

Stafford RJ, Kallel F, Hazle J, Cromeens D, Price R, Ophir J. Elastographic imaging of thermal lesions in soft-tissue: a preliminary study in vitro. Ultrasound in Medicine and Biology. 24: 1449–1458, 1998.

Starritt H, Duck F, Humphrey V. An experimental investigation of streaming in pulsed diagnostic ultrasound beams. Ultrasound in Medicine Biology. 15: 363–373, 1989.

Suh JK, Spilker RL. Indentation analysis of biphasic articular-cartilage – nonlinear phenomena under finite deformation. Journal of Biomechanical Engineering – Transactions of the ASME. 116: 1-9, 1994.

Suh JKF, Youn I, Fu FH. An in situ calibration of an ultrasound transducer: a potential application for an ultrasonic indentation test of articular cartilage. Journal of Biomechanics. 34: 1347-1353, 2001.

Tanter M, Bercoff J, Sandrin L, Fink M. Ultrafast compound imaging for 2-D motion vector estimation: Application to transient elastography. IEEE Transactions on Ultrasonics, Ferroelectrics and Frequency Control. 49: 1363-1374, 2002.

Taylor LS, Porter BC, Rubens DJ, Parker KJ. Three-dimensional sonoelastography: principles and practices. Physics in Medicine and Biology. 45: 1477-1494, 2000.

ter Haar GR. Therapeutic ultrasound. European Journal of Ultrasound. 9: 3-9, 1999.

Toyras J, Laasanen MS, Saarakkala S, Lammi MJ, Rieppo J, Kurkijarvi J, Lappalainen R, Jurvelin JS. Speed of sound in normal and degenerated bovine articular cartilage. Ultrasound in Medicine Biology. 29: 447-454, 2003.

Toyras J, Lyyra-Laitinen T, Niinimaki M, Lindgren R, Nieminen MT, Kiviranta I, Jurvelin JS. Estimation of the Young's modulus of articular cartilage using an arthroscopic indentation instrument and ultrasonic measurement of tissue thickness. Journal of Biomechanics. 34: 251-256, 2001.

Toyras J, Rieppo J, Nieminen MT, Helminen HJ, Jurvelin JS. Characterization of enzymatically induced degradation of articular cartilage using high frequency ultrasound. Physics in Medicine and Biology. 44: 2723- 2733, 1999.

Uchio Y, Ochi M, Adachi N, Kawasaki K, Iwasa J. Arthroscopic assessment of human cartilage stiffness of the femoral condyles and the patella with a new tactile sensor. Medical Engineering & Physics. 24: 431- 435, 2002.

Vannah WM, Drvaric DM, Hastings JA, Stand JA, Harning DM. A method of residual limb stiffness distribution measurement. Journal of Rehabilitation Research and Development. 36: 1-7, 1999.

Varghese T, Ophir J. Enhancement of echo-signal correlation in elastography using temporal stretching. IEEE Transactions on Ultrasonics, Ferroelectrics and Frequency Control. 44: 173–180, 1997.

Varghese T, Zagzebski JA, Frank G, Madsen EL. Elastographic imaging using a handheld compressor. Ultrasonic Imaging. 24: 25-35, 2002.

Viidik A. Biomechanics and functional adaptation of tendons and joint ligaments. Studies on the anatomy and function of bone and joints, Evans, Springer-Verlag, New York. 17-39, 1966.

Walker WF, Fernandez FJ, Negron LA. A method of imaging viscoelastic parameters with acoustic radiation force. Physics in Medicine and Biology. 45: 1437-1447, 2000.

Walker WF, Friemel BH, Laurence NB, Trahey GE. Real-time imaging of tissue vibration using a two-dimensional speckle tracking system. Proceedings 1993 IEEE Ultrasonics Symposium. 873-877, 1993.

Wear KA. Frequency dependence of ultrasonic backscatter from human trabecular bone: theory and experiment. Journal of the Acoustic Society of America. 106: 3659-3664, 1999.

Wear KA, Stuber AP, Reynolds JC. Relationships of ultrasonic backscatter with ultrasound attenuation, sound speed and bone mineral density in human calcaneus. Ultrasound in Medicine and Biology. 26: 1311-1316, 2000.

Wells P. Biomedical ultrasonics, New York; Academic Press Inc. 1977.

Wilson LS, Robinson DE. Ultrasonic measurement of small displacements and deformations of tissue. Ultrasonic Imaging. 4: 71–82, 1982.

Woo S, Manynard J, Butler D. Ligament, tendon, and joint capsule insertions to bone. In: Woo SY, Buckwalter JA, editors. Injury and repair of musculoskeletal soft tissues. Park Ridge, IL: American Academy of orthopaedic Surgeons Symposium. 129-166, 1988.

Wong MWN, Qin L, Lee KM, Tai KO, Chong WS, Leung KS, Chan KM. Healing of bone-tendon junction in a bone though. Clinical Orthopaedics and Related Research. 413: 291-302, 2003.

Wong MWN, Qin L, Tai JKO, Lee SKM, Leung KS, Chan KM. Engineered allogeneic chondrocyte pallet for reconstruction of fibrocatilage zone at bone-tendon junction – a

preliminary histological observation. Journal of Biomedical Material Research Part B: Applied Biometerials. 70B: 362-367, 2004.

Wu J, Du G. Acoustic streaming generated by a focused gaussian beam and finite amplitude tonebursts. Ultrasound in Medicine and Biology. 19: 167–176, 1993.

Wu JZ, Herzog W, Epstein M. Evaluation of the finite element software ABAQUS for biomechanical modeling of biphasic tissues. Journal of Biomechanics. 31: 165-169, 1998.

Xia Y, Moody JB, Burton-Wurster N, Lust G. Quantitative in situ correlation between microscopic MRI and polarized light microscopy studies of articular cartilage. Osteoarthritis and Cartilage. 9: 393-406, 2001.

Yamakoshi Y, Sato J, Sato T. Ultrasonic imaging of internal vibration of soft tissue under forced vibration. IEEE Transactions on Ultrasonics Ferroelectrics and Frequcy Control. 37: 45-53, 1990.

Yang KH, Parvizi J, Wang SJ, Lewallen DG, Kinnick RR, Greenleaf JF, Bolander ME. Exposure to low-intensity ultrasound increases aggrecan gene expression in a rat femur fracture model. Journal of Orthopaedic Research. 14: 802-809, 1996.

Yu WP, Blanchard JP. An elastic-plastic indentation model and its solutions. Journal of Materials Research. 11: 2358-2367, 1996.

Zhang M, Zheng YP, Mak AFT. Estimating the effective Young's modulus of soft tissues from indentation tests - nonlinear finite element analysis of effects of friction and large deformation. Medical Engineering & Physics. 19: 512-517, 1997.

Zhao B, Basir OA, Mittal GS. A self-aligning ultrasound sensor for detecting foreign bodies in glass containers. Ultrasonics. 41: 217-222, 2003.

Zheng YP. Development of an ultrasound indentation system for biomechanical properties assessment of limb tissues in vivo. Ph.D dissertation, The Hong Kong Polytechnic University, Hong Kong, P.R.C., 1996.

Zheng YP, Bridal SL, Shi J, Saied A, Lu MH, Jaffre B, Mak AFT, Laugier P. High resolution ultrasound elastomicroscopy imaging of soft tissues: System development and feasibility. Physics in Medicine and Biology. 49: 3925-3938, 2004.

Zheng YP, Choi YKC, Wong K, Chan S, Mak AFT. Biomechanical assessment of plantar foot tissue in diabetic patients using an ultrasound indentation system. Ultrasound in Medicine Biology. 26: 451-456, 2000.

Zheng YP, Mak AFT. An ultrasound indentation system for biomechanical properties assessment of soft tissues in-vivo. IEEE Transactions on Bio-Medical Engineering. 43: 912-918, 1996.

Zheng YP, Mak AFT, Lau KP, Qin L. An ultrasonic measurement for in vitro depth-dependent equilibrium strains of articular cartilage in compression. Physics in Medicine and Biology. 47: 3165-3180, 2002.

Zheng YP, Shi J, Patil SG, Qin L, Mak AFT. Ultrasonic measurement of articular cartilage swelling: preliminary results. SPIE Medical Imaging: Ultrasonic Imaging and Signal Processing Conference. Feb 15-20, San Diego, CA, USA. 501-512, 2003.